3D Reconstruction of the Proximal Femur and Lumbar Vertebrae from Dual-energy X-ray Absorptiometry for Osteoporotic Fracture Risk Assessment

Tristan Whitmarsh

TESIS DOCTORAL UPF / 2012

Under supervision of
Prof. Alejandro F. Frangi
and
Dr. Ludovic Humbert
Department of Information and Communication Technologies
Universitat Pompeu Fabra

Abstract / Resumen

Abstract. This thesis addresses the growing problem of osteoporosis-related fractures. Osteoporosis is a bone disease characterized by a degradation of the bone structure which can eventually lead to fractures. The disease progresses with age and with our rapidly aging society will become an increasingly important a public health problem. Currently, areal Bone Mineral Density (BMD) measurements from Dual-energy X-ray Absorptiometry (DXA) remains the standard modality for the diagnosis of osteoporosis and assessing the risk of fracture. These measurements, however, are limited descriptors considering the 3D shape and spatial distribution of bone largely determines its strength.

In this thesis a method was developed to reconstruct both the 3D shape and the BMD distribution from standard clinical DXA images. The proposed method incorporates a statistical model built from a large dataset of Quantitative Computed Tomography (QCT) scans which encodes the variations in shape and spatial distribution of the bone. Using a 3D-2D intensity based registration technique an instance of the model is found such that the projection of the model corresponds with the DXA image.

The method was evaluated for its ability to reconstruct the proximal femur from a single DXA image. The resulting parameters of the reconstructions were subsequently evaluated for their hip fracture discrimination ability. The reconstruction method was finally extended to the reconstruction of the lumbar vertebrae from anteroposterior and lateral DXA, thereby incorporating a multi-object and multi-view approach.

The techniques presented in this thesis can potentially improve the fracture risk estimation accuracy over current clinical practice while maintaining DXA as the standard modality.

Resumen. Esta tesis aborda el problema creciente de fracturas asociadas a osteoporosis. La osteoporosis es una enfermedad de los huesos caracterizada por una degradación de la estructura ósea que puede conducir eventualmente a fracturas. La enfermedad progresa con la edad y en nuestra sociedad, que envejece rápidamente, se convierte en un problema de salud pública cada vez más importante. En la actualidad, la medición de la Densidad Mineral Ósea (DMO) por unidad de área hecha con DXA sigue siendo la modalidad estándar para el diagnóstico de la osteoporosis y la evaluación del riesgo de fractura. Estas mediciones, sin embargo, son descriptores limitados teniendo

en cuenta que la forma tridimensional y la distribución espacial de los huesos determinan en gran medida su fuerza.

En esta tesis se desarrolló un método para reconstruir tanto la forma 3D como la distribución de la DMO a partir de imágenes clínicas estándar de DXA. El método propuesto incorpora un modelo estadístico construido a partir de una gran base de datos de imágenes de QCT, el cual codifica plas variaciones en la forma y en la distribución espacial del hueso. Mediante el uso de una técnica de registro 3D-2D basada en intensidades, una instancia del modelo es hallada de manera que la proyección del modelo se corresponde con la imagen de DXA.

El método fue evaluado por su capacidad para reconstruir la parte proximal del fémur a partir de una sola imagen de DXA. Los parámetros resultantes de las reconstrucciones fueron evaluados posteriormente por su capacidad para discriminar una fractura de cadera. El método de reconstrucción se extendió finalmente a la reconstrucción de las vértebras lumbares a partir de DXA anteroposterior y lateral, de ese modo incorporando al método un enfoque multi-objeto y multi-vista.

Las técnicas presentadas en esta tesis pueden potencialmente mejorar la precisión en la estimación del riesgo de fractura respecto a la estimación que ofrece la práctica clínica actual, a la vez que permiten mantener la DXA como la modalidad estándar.

Contents

List of Figures

List of Tables

Acronyms

2RMS	2 Root Mean Square
aBMD	Areal Bone Mineral Density
AAM	Active Appearance Model
AP	Anterior-posterior
AUC	Area Under the Curve
AUROC	Area Under the Receiver Operating Curve
BMC	Bone Mineral Content
BMD	Bone Mineral Density
BMI	Body Mass Index
CI	Confidence Interval
CSA	Cross-sectional Area
CT	Computed Tomography
DRR	Digitally Reconstructed Radiograph
DXA	Dual-energy X-ray Absorptiometry
GPA	Generalized Procrustes Analysis
HA	Hydroxyapatite
HSA	Hip Structural Analysis
ICP	Iterative Closest Point
MI	Mutual Information
MSE	Mean Squared Error
OR	Odds Ratio
PC	Principal Component
PCA	Principal Component Analysis
QCT	Quantitative Computed Tomography
QU	Quantitative Ultrasound
ROC	Receiver Operating Curve
SVD	Singular Value Decomposition
TPS	Thin Plate Spline
vBMD	Volumetric BMD Bone Mineral Density
VFA	Vertebral Fractures Assessment
WHO	World Health Organization

Preface

This thesis signifies the completion of my doctorate degree and with it I would like to thank those who contributed to this achievement.

First and foremost I have to thank my advisor Prof. Alexjandro F. Frangi for his continuous support and dedication to my work and for allowing me to start a new direction on orthopedic research previously unexplored within our group.

I will forever be grateful to Mathieu de Craene for taking me under his wing during my first year as a PhD student and, although not officially recognized in this thesis, he will forever be considered by me as my first co-supervisor. I also have to thank my official co-supervisor Ludovic Humbert who arrived later into my PhD and who from the start showed a keen interest in my work and whose deep involvement went beyond the call of duty.

I am obliged to many of my colleagues who supported me within and outside of the working environment. In particular Daniel Romero, Hrvoje Bogunović and Hernán Morales (and his lovely wife Issis) whose door was always open to me. I would also like to express my thanks to the extensive management team of CISTIB and UPF for their organizational support.

I owe my deepest gratitude to Luis Del Río Barquero who gave the spark of life to this work and without who this thesis would never have seen the light of day. I could always count on his enthusiasm to motivate me. Together with the charm of Silvina Di Gregorio, he managed to convince a vast amount of people to volunteer as subjects in my research and, although they will forever remain anonymous, I owe them a great deal of gratitude. I am also indebted to Jorge Malouf for his support with the data acquisition.

I am grateful to Prof. Rainer Schubert who allowed me to do a 7 month research visit in Austria and Karl D. Fritscher who supported me during this period and beyond. I would also like to thank the University of Sheffield for hosting me during the last phase of my thesis.

I would like to thank all my old friends for sticking with me and all the new friends I made throughout these years. In particular Rida Sadek (and his lovely wife Nardine) who introduced me to Barcelona and remained a close friend throughout my PhD.

I would like to gratefully acknowledge the various sources of funding. The research leading to this thesis was was preliminary funded by a grant from the Instituto de Salud Carlos III (FI09/00757). Additional funding was received from the ERDF Operational Programme of Catalonia 2007-

2013, through the 3D-FemOs project (exp. VALTEC 09-02-0012) and the VERTEX project (exp. RD10-1-0034). In addition, this work was partially funded by the European Union Seventh Framework Programme (FP7/2007-2013) under grant agreement nr 269909, MySPINE project, and the Spanish Ministry Science and Innovation (ref. TIN2009-14536-C02-01), Plan E and ERDF funds.

I am deeply grateful for my family for unconditionally supporting me throughout my life and my career choices. Now that I will take my careful steps back into society I hope that the friends I made during these years will continue to remain by my side wherever fate will lead me.

1

Introduction

This chapter describes the context within which this thesis is presented. The following chapters are based on three distinct publications. The final section presents the conclusions related to this thesis and the possible future directions in extension of this work.

1.1 Osteoporotic Fractures

Osteoporosis is a systemic skeletal disease characterized by low bone mass and micro-architectural deterioration of bone tissue, leading to enhanced bone fragility and a consequent increase in the risk of fracture [111]. Osteoporotic fractures predominantly occur at the proximal femur and the vertebrae. For the year 2000, there were an estimated 9 million new osteoporotic fractures, of which 1.6 million were at the proximal femur and 1.4 million were clinical vertebral fractures [61]. The combined lifetime risk for osteoporotic fractures is around 40%. Although the majority of vertebral fractures remain undiagnosed, they can potentially result in great discomfort and a diminished quality of life. Moreover, Osteoporosis and associated fractures are an important cause of morbidity and mortality. Up to 20% of patients die in the first year following a hip fracture [19][93], while only about one-third of survivors regain their original level of function [23][111].

Osteoporosis and the subsequent fractures are most common among postmenopausal woman. Approximately 1 in 3 women over 50 will suffer a fracture due to osteoporosis whereas for men this is 1 in 5 [84][83]. The incidence of osteoporotic fractures increases with age and with the rapid aging of our society, osteoporosis is becoming one of the most prevalent health problems. Moreover, osteoporotic fractures are associated with a high economic burden. The International Osteoporosis Foundation (IOF) estimates the costs associated with treating osteoporotic fractures in the USA, Canada and Europe at approximately 48 billion USD [34] which is forecast to increase to 131.5 billion USD by 2050 [77]. Osteoporosis also results in huge indirect costs that are rarely calculated and which are probably at least 20% of the direct costs [77].

1.2 Current clinical practice

Osteoporosis is currently diagnosed from Dual-energy X-ray Absorptiometry (DXA). DXA measures the attenuation of X-ray beams with a high and low energy through the body. The attenuation depends on the energy of the X-rays as well as the density of the tissue. By assuming the body is composed out of two types of tissue (bone mineral and soft tissue), the Bone Mineral Content (BMC) can be discriminated from the soft tissue by analyzing the attenuation of the high and low energy X-ray beams. In this way a projection image of the BMC is acquired. The so called areal Bone Mineral Density (aBMD) is subsequently measured at several locations of the proximal femur or spine. To provide a diagnosis, a T-score is computed relating to the number of standard deviations above or below the mean for

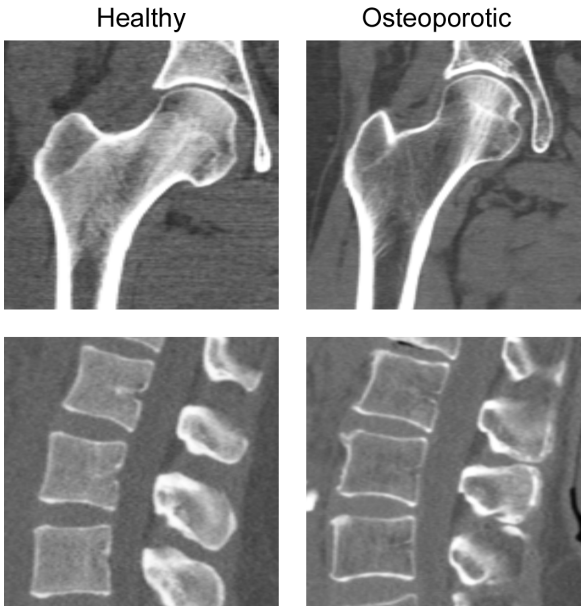

Figure 1.1: CT slices of the proximal femur (top) and lumbar vertebrae (bottom) of a healthy (left) and an osteoporotic patient (right).

a population of healthy young adults (at the age of 35) of the same sex and ethnicity as the patient. The World Health Organization (WHO) classifies patients as healthy when the T-score of the femoral neck is greater than -1, osteopenic when the T-score is between -1 and -2.5, osteoporotic when it is less than -2.5 and severe (established) osteoporosis when the T-score is less than -2.5 and the patient has previously suffered an osteoporotic fractures.

The Bone Mineral Density (BMD) has been shown to be strongly related to fracture incidence. A 10% loss of bone mass in the vertebrae can double the risk of vertebral fractures, and similarly, a 10% loss of bone mass in the hip can result in a 2.5 times greater risk of hip fracture [66]. However, There is growing evidence that structural parameters are critical in determining the bone strength and thus its resistance to fracture [81].

Towards this end Hip Structural Analysis (HSA) has been developed to extract geometric measurements from DXA projections [6] [116]. In addition, Vertebral Fractures Assessment (VFA) examines the lateral DXA images of the spine to screen for previous vertebral fractures which also suggests the presence of osteoporosis. However, these measurements from planar radiographs are still limited descriptors of the complex bone shapes.

A 3D representation of the bone can be acquired by Quantitative Computed Tomography (QCT). Here, a reference density phantom is included within a regular Computed Tomography (CT) acquisition to convert the Hounsfield units to corresponding BMD values. Several parameters derived from QCT, such as trabecular and cortical BMD, the volumetric Bone Min-

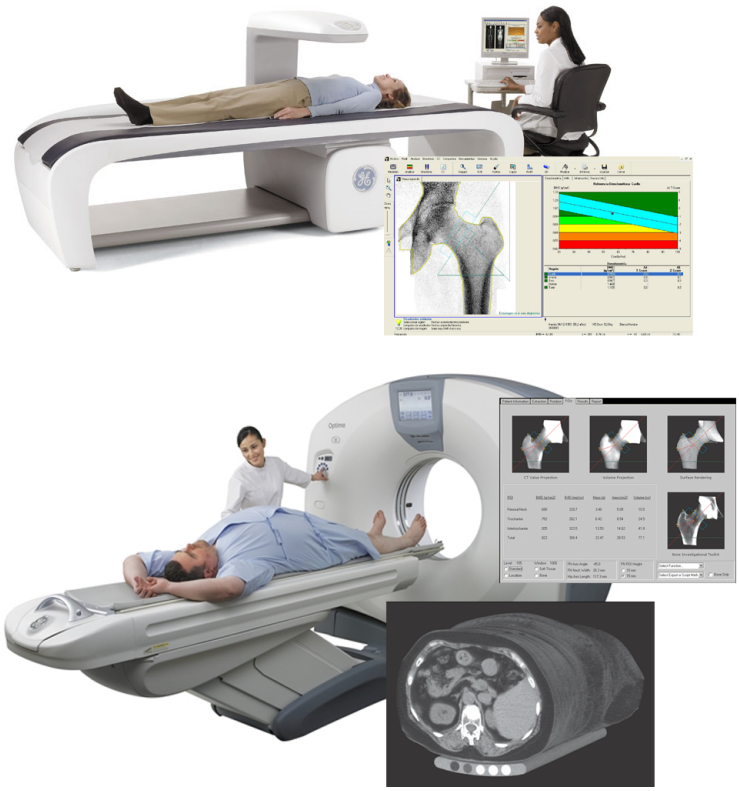

Figure 1.2: A picture of GE Healthcare's Lunar iDXA scanner (GE Healthcare, Madison, WI, USA) (top) with a screenshot of the software platform, enCORE and GE Healthcare's Optima CT660 CT System (bottom) with the Mindways calibration phantom and software to perform a QCT analysis (Mindways Software Inc., Austin, TX, United States).

eral Density (vBMD) at specific regions, the neck axis length and the cortical thickness, have been shown to be strongly correlated with the femoral strength and may improve the fracture risk estimation over DXA derived areal BMD alone [12]. This medical imaging technique, however, is associated with high financial costs, a high radiation dose for the patient and consequently is not used in clinical routine for osteoporosis diagnosis or fracture risk assessment.

Recently Quantitative Ultrasound (QU) [45] has received a great deal of interest as a bone density measurement tool. It has the advantage of being relatively cheap and does not administer the patient to radiation. However, as of yet the precision of this device does not reach what is possible using DXA or QCT.

For the above mentioned reasons DXA remains the current clinical standard in osteoporosis diagnosis and fracture risk assessment.

1.3 Aim and objectives of this thesis

The aim of this thesis is to work towards the development of a fracture risk estimation method for the proximal femur and vertebrae from low radiation dose DXA images currently used in clinical routine, while taking into account the 3D shape and spatial distribution of the bone. Towards this goal three distinct problems have been addressed and investigated:

- *Reconstruction of both the 3D bone shape and 3D BMD distribution of the proximal femur from a single DXA image:* This includes the development of a statistical model of the 3D shape and BMD distribution and a method for its construction from a large dataset of QCT scans. In addition, an intensity based 3D-2D registration method is developed to register the statistical model onto DXA resulting in the 3D reconstruction. The accuracy of the reconstruction method is evaluated on real in vivo DXA images where both the reconstructed shape and the reconstructed BMD distribution is evaluated with respect to the same subject QCT scan.

- *Hip Fracture Discrimination from Dual-energy X-ray Absorptiometry by Statistical Model Registration:* The parameters of the statistical model resulting from the registration onto DXA are evaluated for their ability to discriminate between fracture patients and a control group.

- *3D Reconstruction of the Lumbar Vertebrae from Anteroposterior and Lateral Dual-energy X-ray Absorptiometry:* This requires the extension of the reconstruction method to multi-view and a multi-object approach to deal with the superimposition of the vertebrae on the radiographs.

2

Reconstructing the 3D Shape and Bone Mineral Density Distribution of the Proximal Femur from Dual-energy X-ray Absorptiometry

This chapter presents a method to reconstruct both the 3D bone shape and BMD distribution of the proximal femur from a single DXA image used in clinical routine. A statistical model of the combined shape and BMD distribution is presented, together with a method for its construction from a set of QCT scans. A reconstruction is acquired in an intensity based 3D-2D registration process whereby an instance of the model is found that maximizes the similarity between its projection and the DXA image. Reconstruction experiments were performed on the DXA images of 30 subjects, with a model constructed from a database of QCT scans of 85 subjects. The accuracy was evaluated by comparing the reconstructions with the same subject QCT scans.

The content of this chapter is adapted from the following publication:

T. Whitmarsh, L. Humbert, M. De Craene, L.M. Del Rio Barquero, A.F. Frangi, Reconstructing the 3D Shape and Bone Mineral Density Distribution of the Proximal Femur from Dual-energy X-ray Absorptiometry. *IEEE Transactions on Medical Imaging*, vol. 30(12), pp. 2101-14, 2011.

2.1 Introduction

Femur fractures due to osteoporosis account for significant morbidity, disability, decreased quality of life, mortality and high economic cost for society. Up to 20% of patients die in the first year following hip fracture and in the USA approximately 20% of hip fracture patients require long-term care in a nursing home [111]. The lifetime risk of hip fracture lies between 14% and 20% for caucasian women in Europe and the USA [111]. Osteoporosis predominantly affects post menopause women and thus in most countries the fracture rates among men are substantially lower. Due to the increasing life expectancy, the WHO estimated that the number of osteoporotic femur fractures in the world will have increased from 1.3-1.7 million in 1999 to almost 3 million by 2025 [111]. This indicates the importance of an accurate diagnosis of osteoporosis and fracture risk assessment.

Osteoporosis is currently diagnosed from DXA, which results in an image of the projected BMD (g/cm^2). To provide a diagnose, a T-score is computed relating to the number of standard deviations above or below the mean for a population of healthy adults of the same sex and ethnicity as the patient.

Currently the FRAX®tool [1] is in development by the WHO to evaluate the fracture risk of patients by combining clinical risk factors with the BMD at the femur neck. However, in current clinical practice, DXA derived BMD remains the common measure for diagnosis.

Although DXA gives an accurate planar representation of the BMD, it is limited by its two-dimensionality, and therefore does not represent the 3D shape or spatial distribution of the BMD. To overcome this limitation, a 3D representation of the femur bone with BMD distribution can be acquired by Quantitative Computed Tomography (QCT). For QCT, a calibration phantom is used to relate the Hounsfield unit of the CT scan to a BMD (mg/cm^3). Several parameters derived from QCT, such as trabecular and cortical BMD, the volumetric BMD (vBMD) at specific regions, the neck axis length and the cortical thickness, have been shown to be strongly correlated with the femur strength [21][70] and may better explain failure load variance [11] and improve the fracture risk estimation over DXA derived areal BMD alone [12]. This medical imaging technique, however, is associated with high financial costs, a high radiation dose for the patient and consequently is not used in clinical routine for osteoporosis diagnosis or fracture risk assessment. Therefore, recent work has focused on acquiring a 3D reconstruction from planar images by incorporating a priori information in the form of a statistical model. This could potentially improve upon current standards in osteoporosis diagnosis and fracture risk assessment while keeping DXA as the standard modality.

Already a lot of research has been done in reconstructing the shape of bones from planar x-ray images [72][5]. Few, however, take on the challenge of performing a reconstruction from the rather noisy DXA images. In Kolta *et al.* [67], a generic model is deformed to match the contours of two DXA images. Langton *et al.* [71] proposed a similar method, reconstructing the shape from a single DXA image by deforming an average template model.

Other approaches incorporate a statistical model describing the 3D shape variations of a population in order to get a probabilistic reconstruction. A contour matching method can then be incorporated to reconstruct the femur shape from a sparse set of projections [69][119][33][3][118]. These methods, however, are limited to the reconstruction of the shape, without addressing the reconstruction of the BMD distribution.

Various authors proposed models containing information about the BMD distribution. Yao and Taylor [114] proposed a statistical model described by a tetrahedral mesh with Bernstein polynomial density functions in the tetrahedrals. Both Belenguer-Querol *et al.* [95] and Fritscher *et al.* [37] developed a combined shape and density model where a statistical analysis was performed onto the intensities in the volumes and the displacement fields resulting from non-rigid registrations. The work of Fritscher *et al.* [37] was later adapted by Schuler *et al.* [101] by performing non-rigid registrations on Euclidean distance maps, thereby maintaining the spatial density distribution inside the bone.

In Steininger *et al.* [103], this model was used in a registration process to extract the contour from a single X-ray image. A similar model was used by Hurvitz *et al.* [57] to reconstruct the full shape of the proximal femur. Here, the advantage of using the density distribution is in establishing correspondences on other places than only the contours. But, still no attempt was made to reconstruct the BMD distribution from a DXA image.

Using a statistical model containing information about the spacial distribution of the bone densities, a reconstruction from DXA can be acquired by an intensity based registration process, given the fact that DXA represents a projection of the bone mineral densities. For an overview of intensity based 3D-2D registration techniques we would like to refer the reader to Markelj *et al.* [79].

In Ahmad *et al.* [2], a volumetric image of the bone densities is reconstructed from four DXA images. An average tetrahedral femur model containing shape and density information was constructed from a set of manually segmented QCT scans. Deformation fields were then calculated from this average femur model to each subjects tetrahedral model and principal component analysis was performed on the deformation fields to calculate the principal modes of variation. Following the work of Yao and Taylor [113] and Sadowsky *et al.* [98], in an iterative registration process, the resulting statistical model is registered onto four DXA images. At each iteration, the pose (location and orientation in space), scale, and modes of variation of the statistical model are varied to minimize the difference between the simulated DXA images from projections of the model and the real DXA images. Mutual information was used as the similarity measure and thus the resulting volume is adjusted in a post processing according to the densities of one of the DXA images. The issues concerning the use of in-vivo data, in particular with regards to the overlap of the pelvis with the femur head in the DXA images, remain unaddressed in this paper. More importantly, this work relies on multiple views generated by a C-arm DXA device. These devices are still not widely used in clinical routine as opposed to single view devices.

This work therefore presents and evaluates a method to automatically reconstruct both the 3D shape and BMD distribution of the proximal femur from a single 2D DXA image. In earlier work [109], this method was evaluated on simulated DXA images using an in-vitro QCT dataset. This work extends the method to an in-vivo context using true DXA images. A statistical model of the combined 3D shape and BMD distribution is first constructed from an in-vivo database of QCT scans of the proximal femur. In an intensity based 3D-2D registration process, an instance of the model is found whereby the similarity between its projection and the DXA image is maximized. Finally, the accuracy of the method is evaluated in-vivo by performing reconstruction experiments on a set of DXA images of patients, and comparing the reconstructed shape and BMD distribution with the same subject QCT scans.

2.2 Methods

The reconstruction method proposed here uses a statistical model of the combined shape and density distribution. This model is first constructed from a large dataset of QCT scans (Section 2.2.1). The reconstruction method then incorporates an automatic intensity based 3D-2D registration process whereby an instance of the model is found that maximizes the similarity between the DXA image and the projection of the model instance (Section 2.2.2). The reconstruction accuracy is evaluated by comparing the reconstructions from 30 DXA images with the same subject QCT scans (Section 2.2.3).

2.2.1 Statistical model

The statistical model is based on Active Appearance Models developed by Cootes *et al.* [27] and combines statistical information about the shape and BMD distribution. First, a shape model is built following the work of Frangi *et al.* [35] using non-rigid registrations of the QCT volumes onto a segmented reference subject (Section 2.2.1). The individual QCT volumes are then deformed to the mean shape and a density model is built from the resulting volumes (Section 2.2.1). Finally, to capture the relation between the shape and density distribution, both are combined into a single statistical model (Section 2.2.1). This combined model encodes the variations of shape and BMD distribution of the input population to be used in the reconstruction process.

Data

A database of CT scans of 115 patients (42 male and 73 female with an average age of 55 ± 12 years was collected at CETIR Grup Mèdic (CDP Unit Esplugues, Esplugues de Llobregat, Barcelona, Spain). The patients consisted of volunteers which required densitometry scans for body composition analysis. Subjects were only rejected in case the scans were unusable, for

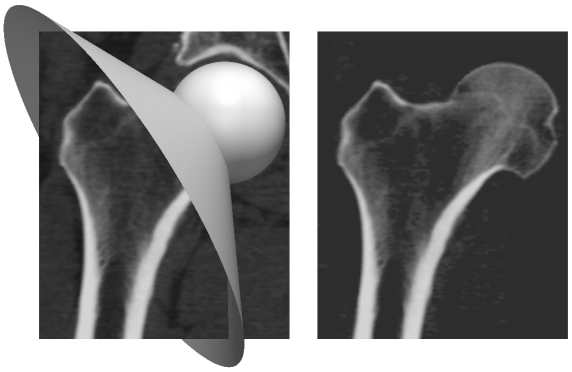

Figure 2.1: Preprocessing of the QCT volumes. A slice of the QCT volume with the manually defined sphere and cone shape defining the region of the pelvis to be removed from the volume (left), and the same slice with the pelvis area removed and a thresholding applied to remove the soft tissue structures (right).

instance due to the presence of an implant, to ensure the largest possible dataset to construct the statistical model.

The CT scans were obtained using the Philips Gemini GXL 16 system (Philips Healthcare, Best, The Netherlands) with a pixel spacing ranging from $0.68 \times 0.68mm$ to $0.96 \times 0.96mm$ and a slice thickness between 0.5 and $1.0mm$. A calibration phantom (Mindways Software Inc., Austin, TX, United States) was placed underneath the patient to relate the Hounsfield units of the CT scan to a BMD. The linear regression between the known phantom densities and the intensities of the phantom in the CT scan gives an average correlation coefficient of 0.9998 indicating an accurate calibration.

Together with the CT scan, a DXA image was acquired of every subject using the GE Healthcare's Lunar iDXA scanner (GE Healthcare, Madison, WI, USA), which generates an image with a pixel spacing of $0.3 \times 0.25mm$. In addition, the femur neck areal BMD was extracted from the DXA image to assess the bone quality. Each subject was subsequently classified as normal, osteopenic or osteoporotic using the T-score of the femur neck areal BMD conform the WHO criteria. This classifies patients as healthy when the T-score is greater than -1, osteopenic when the T-score is between -1 and -2.5 and osteoporotic when it is less than -2.5. Thus, our dataset contains 65 healthy, 43 osteopenic and 7 osteoporotic subjects with and average femur neck areal BMD of $0.9 \pm 0.1g/cm^2$ ranging between 0.7 and $1.4g/cm^2$.

Data preprocessing

The model proposed in this work is constructed by an intensity based registration process using QCT scans of the proximal femur. Performing registrations of the proximal femur is a particularly difficult task because of the close proximity of the femur head with the pelvis [91]. This can result in faulty registrations whereby the femur head registers onto the acetabu-

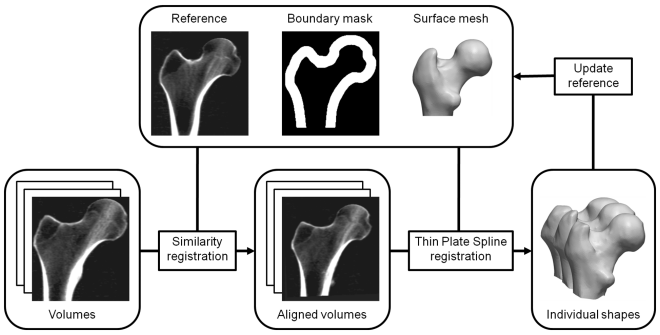

Figure 2.2: Shape model construction pipeline.

lum. To overcome this problem, a preprocessing step is introduced which removes the pelvis from the volume by taking advantage of the spherical characteristic of the femur head (Fig. 2.1).

The point in the center of the femur head and another point on the surface of the femur head lying in the extension of the femur neck are manually determined. These two points define the center and radius of a sphere. In addition, the same points, together with a predefined angle, define the apex and axis of a cone. Using these two regions, the pelvis area can be removed.

To prevent the soft tissue structures from interfering with the registration process, a thresholding set to $60mg/cm^3$ is applied to all volumes resulting in an image containing only the bone.

Shape model construction

The intensity based registration process to construct the shape model is depicted in Fig. 2.2. All registration algorithms used in this work were implemented using the Insight Segmentation and Registration Toolkit (ITK) [115]. The registrations are performed on the preprocessed volumes where the pelvis area and soft tissue structures are removed (Section 2.2.1).

A *reference* volume is chosen manually based on the smoothness of its bone surface, i.e., not having any unusual bumps or dents. The femur bone in this reference volume is subsequently segmented using ITK-SNAP [117], which provides a semi-automatic segmentation using active contour methods.

To reduce the computation load of the registrations, a mask is generated of the bone boundary (*boundary mask*) by dilating the segmentation and subtracting an image mask of the erosion. In addition, a mesh is extracted from the segmentation onto which some additional processing is done to generate a smooth regular *surface mesh* consisting of 7147 vertices.

Every volume in the dataset is first registered onto the reference volume by a *similarity registration* (translation, rotation and uniform scaling). This uses an intensity based registration process where the Mutual Information (MI) similarity measure is optimized using Powell's multi-dimensional optimization method [94].

This is followed by a multi-scale intensity based *Thin Plate Spline (TPS) registration* where the landmarks on the reference volume are defined by the corresponding surface mesh. In an intensity based registration process, the positions of the landmarks on the target volume are found which defines a TPS transformation that, when applied to the target volume, maximized the similarity with the reference. This part of the registration process is similar to Meyer *et al.* [85] where a probabilistic atlas of a brain is constructed by mapping a Magnetic Resonance Imaging scan of each subject to an atlas using TPS registrations.

The TPS registration is incorporated in a multi-scale registration scheme whereby the result of each registration initializes the registration of the higher resolution. The different resolutions are generated by decimating the reference mesh. Here the number of triangles are reduced using the quadric error metric outlined in Hoppe [53]. Three levels of detail of approximately 50, 100 and 200 control points were used. The final registration using the decimation of 200 control points was applied to the original detailed surface mesh. This results in a detailed surface mesh for all similarity-aligned volumes with a point correspondence between them (*individual shapes*), which are used to generate the shape model.

In this work an implementation of the TPS transformation is used, which allows for the computation of the derivative [14] and can thus be used in conjunction with the L-BFGS-B optimizer [122]. For the similarity measure MI is used, which is extended by a regularization term as explained in the following paragraph.

Similarity measure for TPS registration. Without constraining the movement of the TPS control points, they can drift (e.g. along the shaft) and altogether reduce the correspondence accuracy between subjects. To avoid this, Mattes Mutual Information metric [80] was extended by a regularization term. The mesh is modeled as a spring system whereby each edge of the mesh is defined as a spring [78]. The landmark displacements $\mathbf{p}$ will result in a stretching or compression for each edge e of the mesh M, which defines a spring energy E:

$$\mathrm{E}(\mathbf{p}) = \frac{\lambda}{n} \sum_{e \in M} \left(\frac{\|e(\mathbf{p})\| - \|e\|}{\|e\|} \right)^2 . \tag{2.1}$$

Here, n is the number of edges, $\|e\|$ denotes the length (mm) of the edge in the reference mesh and $\|e(\mathbf{p})\|$ the length (mm) of the corresponding edge resulting from the displacements $\mathbf{p}$. In addition, a weight factor λ determines the stiffness of the springs, which is given a value of 5. This energy E is added to the Mutual Information measure MI as a penalty value.

The optimization problem to find the landmark displacements $\mathbf{p}$, which defines the TPS transformation T that maximizes the similarity between the reference image I_{ref} and the target image I_{target}, can now be formulated as:

$$\arg\min_{\mathbf{p}} (-\mathrm{MI}(I_{ref}, I_{target} \circ T(\mathbf{p})) + \mathrm{E}(\mathbf{p})). \tag{2.2}$$

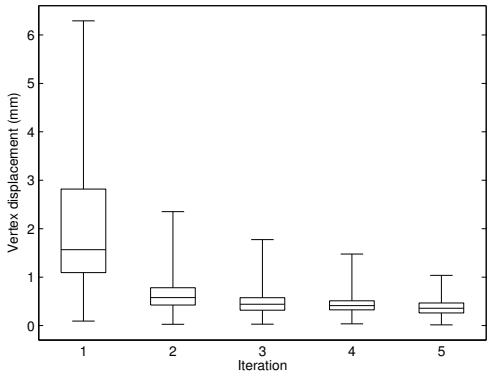

Figure 2.3: Boxplot of the displacements of the reference shape vertices resulting from the iterative updating process in the model construction pipeline for 5 iterations. Each iteration, the average shape was calculated and for each vertex the displacement with respect to the previous reference shape was calculated.

Iterative update. In order to remove some of the bias introduced through the manual reference selection, this registration process is iterated whereby in each iteration the reference volume (together with the mask) is deformed to the mean shape by means of a TPS transformation (Fig. 2.2).

Some previous work on statistical model construction propose an iterative update of the reference by averaging the displacement fields resulting from the individual registrations [35][92]. Non-rigid registrations, however, are subject to foldings, making it necessary to employ strategies incorporating diffeomorphic registrations and averaging displacement fields using logarithms [50].

By only averaging the surface meshes to generate a mean shape, these complex operations are avoided. On the other hand, this averaging can potentially result in self intersections. Even though they have not occurred in our experiments, these can be detected and resolved easily [112].

In Fig. 2.3, the convergence of the reference shape change in the iterative model construction process is shown. The displacement of the reference shape vertices resulting from the iterative updating process is shown for 5 iterations. Each iteration the average shape was calculated and for each vertex the displacement with respect to the previous reference shape was calculated. The boxplot of the displacements for all vertices is given for each respective iteration.

The boxplot shows that this process has converged at the third iteration. This is consistent with the results presented in similar work [22][35]. The model used in the experiments is thus built after 3 iterations. Do note that this refers to the currently used dataset only and does not indicate that the model construction process using a different dataset or different reference converges in the same way.

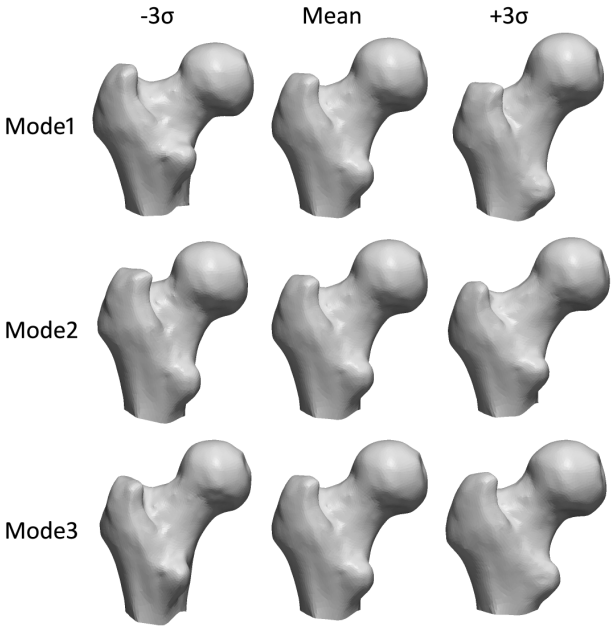

Figure 2.4: The mean and the first three modes of variation of the shape model, varying between -3 and +3 standard deviations (σ).

Statistical analysis. Using the groupwise point correspondence of the individual shapes, the statistical model of the shape is built. The i-th shape can be represented by a shape vector $\mathbf{s}_i = (x_1, y_1, z_1, \ldots, x_n, y_n, z_n)^T \in \mathbb{R}^{3n}$ defined by the n vertices. Principal Component Analysis (PCA) is then applied to the data matrix $D_{shape} = [(\mathbf{s}_1 - \overline{\mathbf{s}})(\mathbf{s}_2 - \overline{\mathbf{s}}) \cdots (\mathbf{s}_k - \overline{\mathbf{s}})]$ where k is the number of shapes and $\overline{\mathbf{s}}$ the average shape. PCA computes an orthonormal basis, aligning the axes with the maximum variation in the data. The axes are given by the eigenvectors (ordered by their importance) of the covariance matrix of D_{shape}, which are also referred to as the modes of variation. Now, a new shape $\mathbf{s}$ can be represented as follows:

$$\mathbf{s} = \overline{\mathbf{s}} + P_s \cdot \mathbf{b}_s \tag{2.3}$$

where P_s denotes the matrix of ordered eigenvectors and $\mathbf{b}_s$ the shape model parameters.

The mean and first three modes of variation of the shape model are shown in Fig. 2.4. From this we can see that the first mode of variation describes the neck-shaft angle, while the second mode of variation extends or compresses the femur neck.

Density model construction

To capture the density variations irrespective of the shape, all unprocessed QCT volumes (without thresholding applied) are deformed to the same av-

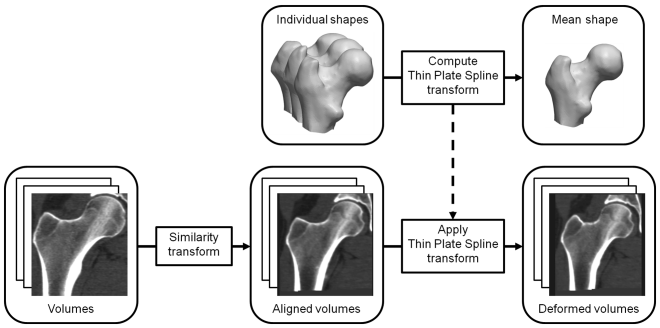

Figure 2.5: Density model construction pipeline.

erage shape. This process is depicted in Fig. 2.5.

The registration process has resulted in the patient-specific shape for each similarity-aligned volume. From these *individual shapes*, the *mean shape* is computed. To deform all the QCT volumes to this mean shape, first the *similarity transform* resulting from the registration process (Section 2.2.1) is applied to the QCT volume of the respective subject. The QCT volumes are now aligned but still need to be deformed to the mean shape. For each similarity-aligned subject we have the individual shape of the bone, which has a vertex correspondence with the average shape. Using this vertex correspondence a *Thin Plate Spline transform* is computed, which deforms the similarity aligned QCT volume to the mean shape.

All volumes were deformed to the same reference volume with a cubic voxel size of $1mm$, which showed to be a good compromise between describing anatomical variations and computational complexity. By using only the points on the bone surfaces for the TPS transformations, the spatial distributions of the BMD inside of the bones is preserved. The deformed QCT volumes now have a voxel correspondence between them and a statistical analysis can be performed over the density values of the voxels to capture the statistical variations of the BMD distribution.

Statistical analysis. The voxel densities in the i-th volume can be represented as a vector $\mathbf{v}_i = (d_1, d_2, \ldots, d_m)^T \in \mathbb{R}^m$ where m is the number of voxels inside the shape and d_m the density of the m-th voxel. PCA is then applied to the data matrix $D_{densities} = [(\mathbf{v}_1 - \overline{\mathbf{v}})(\mathbf{v}_2 - \overline{\mathbf{v}}) \cdots (\mathbf{v}_l - \overline{\mathbf{v}})]$ where l is the number of volumes and $\overline{\mathbf{v}}$ the average volume. A new volume $\mathbf{v}$ can now be represented as follows:

$$\mathbf{v} = \overline{\mathbf{v}} + P_v \cdot \mathbf{b}_v \tag{2.4}$$

where P_v denotes the matrix of ordered eigenvectors and $\mathbf{b}_v$ the density model parameters.

The mean and first three modes of variation of the density model are shown in Fig. 2.6. Since no normalization was applied to the volume densities, the first mode of variation of the density model describes the global

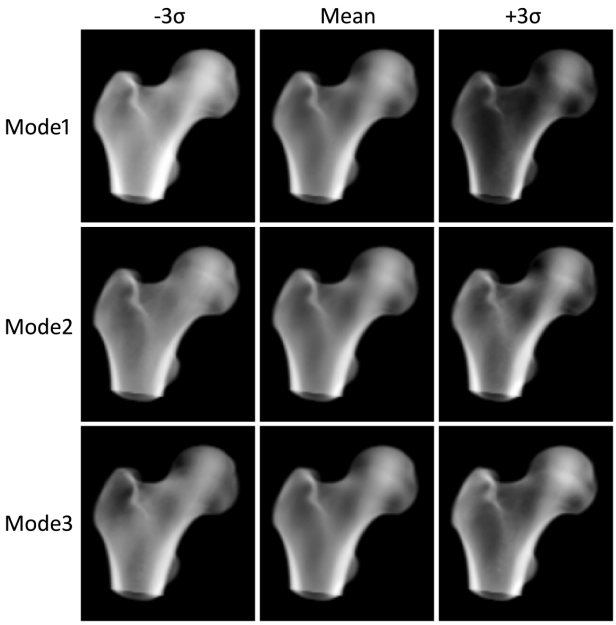

Figure 2.6: Projections of the mean and the first three modes of variation of the density model, varying between -3 and +3 standard deviations (σ).

density change while the rest of the modes describe the distribution of the bone in various ways.

Combined model construction

The relation between the shape and density model is captured, in the same way as Cootes *et al.* [27], by combining them into a single statistical model. Assuming a correlation between the shape and density distribution, this will result in a more compact model. It is reasonable to assume a relationship between the shape and BMD distribution of the proximal femur since a different shape requires a different internal BMD distribution to maintain a certain resistance. Moreover, some combinations of the shape and BMD distribution can be said to be invalid based on the input dataset. By combining the shape and appearance into a single model, the combined model can constrain the shape and BMD distribution to statistically valid combinations.

In our particular application (reconstructing from a single view), we have no information about the thickness of the bone in the direction of the projection. This might cause the density model instance to overestimate the density where after the shape model instance would underestimate the thickness. By combining the shape and density model, more statistical information about the relation between the shape and density distribution is captured, which reduces these faulty combinations. For this same reason, no normalization was applied to the densities in the QCT volumes so as to

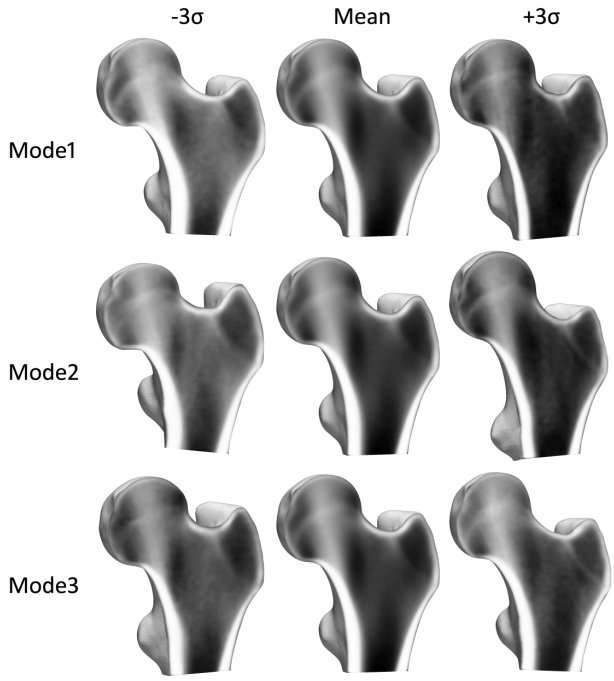

Figure 2.7: The mean and first three modes of variation of the combined model, varying between -3 and +3 standard deviations. The model instances are clipped at the coronal cross-section, showing the BMD distribution variation inside of the shapes.

capture the relation between the shape and the true densities.

Statistical analysis. For each subject in the model, the shape model parameters $\mathbf{b}_s$ and density model parameters $\mathbf{b}_v$ are concatenated into a single vector:

$$\mathbf{b} = \begin{pmatrix} W\mathbf{b}_s \\ \mathbf{b}_v \end{pmatrix} \tag{2.5}$$

where W is a diagonal matrix of weights to match the shape parameter variance to the variance of the density model parameters. PCA is then applied over these vectors, which results in a parameter set $\mathbf{c}$ describing the combined shape and density distribution:

$$\mathbf{b} = Q \cdot \mathbf{c} \tag{2.6}$$

whereby Q is the matrix of ordered eigenvectors.

In Fig. 2.7, the mean and first three modes of variation of the combined model used for the reconstruction experiments is illustrated by clipping the surface mesh of the shape model to show the BMD distribution inside of the surface mesh. Here we can see that the extension of the femur neck (Mode

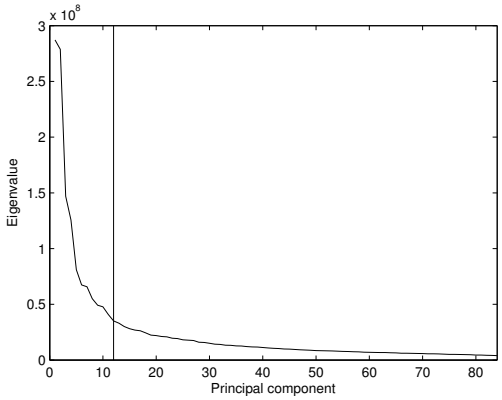

Figure 2.8: The scree plot of eigenvalues associated with the principal components of the combined model. The "elbow" is identified at the $12th$ principal component.

1) and increase of the neck-shaft angle (Mode 2) both results in a BMD increase.

A scree plot is generated where the relative variance is set against their corresponding principal components (Fig. 2.8). At the $12th$ principal component, the decrease of eigenvalues appears to have leveled off to the right of the plot. Following Cattell's scree test [18], the principal components beyond this "elbow" are discarded. Thus, only the first 12 principal components are used in the reconstruction experiments.

By truncating the model parameters beyond the 12th principal component, the original subjects in the model are not fully represented. For each subject in the model, the vertex displacements and density distribution change of the remaining modes of variation determine the residual error resulting from discarding these modes of variation. These vertex displacements are averaged over all subjects and presented as a color map on the mean shape in Fig. 2.9, where also the average residual densities are given for the coronal cross-section, the femur neck and the intertrochanter (Fig. 2.10). The full range of vertex displacements has a mean of $1.1mm$ and 2 Root Mean Square (2RMS) of $2.4mm$ and the residual densities over all subjects gives a mean of 44.4 and 2RMS of $122.5mg/cm^3$.

Model instance

A new instance of the model is described by the combined model parameters $\mathbf{c}$, which gives the parameters of the shape model $\mathbf{b}_s$ and density model $\mathbf{b}_v$ as such:

$$\mathbf{b}_s = W^{-1} \cdot Q_s \cdot \mathbf{c} \tag{2.7}$$

$$\mathbf{b}_v = Q_v \cdot \mathbf{c} \tag{2.8}$$

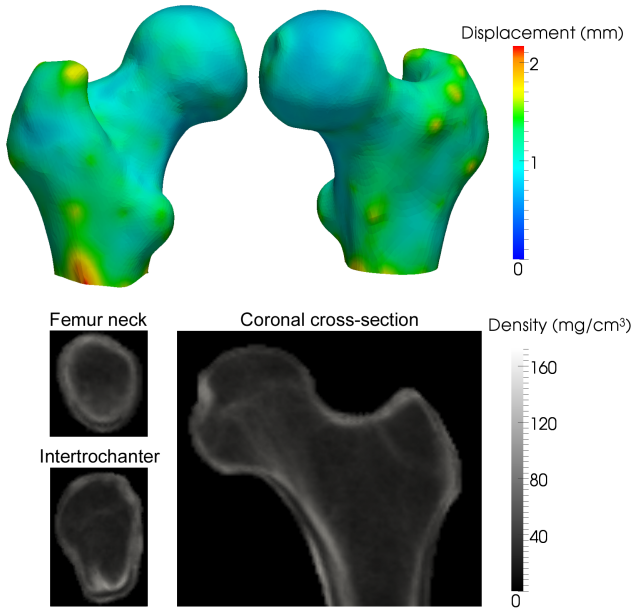

Figure 2.9: The residual vertex displacement (top) and density differences (bottom) resulting from using 12 modes of variation, averaged over all subjects in the model.

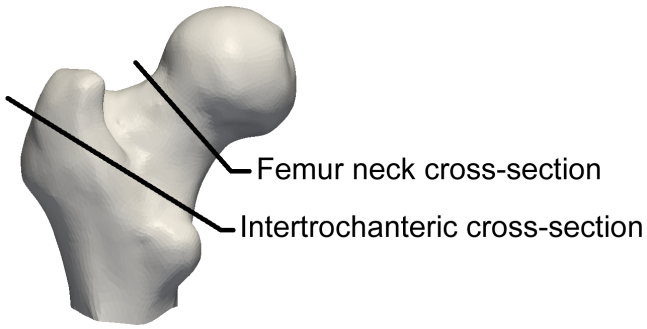

Figure 2.10: The location of the femur neck and intertrochanteric cross-sections.

where

$$Q = \begin{pmatrix} Q_s \\ Q_v \end{pmatrix}. \tag{2.9}$$

Subsequently substituting these shape and density model parameters into (2.3) and (2.4) respectively gives the new shape $\mathbf{s}$ and new density values $\mathbf{v}$.

Similar to Cootes *et al.* [27] the instance of the density model is deformed to the new shape. Here, the deformation is defined by a TPS transformation where the shape model determines the control points. The vertices of the average shape $\overline{\mathbf{s}}$ define the target points and the vertices of the new shape model instance $\mathbf{s}$ define the source points. Since the shape model is built from a dense surface mesh, a subset of the vertices is used. This subset is found by applying the previously mentioned decimation algorithm (Section 2.2.1) on the average shape model resulting in 200 control points and finding the closest points to the vertices of this decimation.

We implicitly reordered the vector of densities $\mathbf{v}$ corresponding to the density model instance to form a volume V according to the dimensions of the reference space all volumes were deformed to:

$$\mathbf{v} \mapsto V. \tag{2.10}$$

The TPS transformation T to deform this volume is defined by the displacements $\mathbf{p}$ resulting from the shape model parameters (2.3):

$$\mathbf{p} = P_s \cdot \mathbf{b}_s. \tag{2.11}$$

Besides the deformation, a pose and a uniform scale factor is applied to the density model instance, which is represented as a similarity transform.

Thus, the new instance of the combined model X is the composition of the density model instance V with the TPS transformation T defined by the shape displacement $\mathbf{p}$ and a similarity transform S as such:

$$X = V \circ T(\mathbf{p}) \circ S. \tag{2.12}$$

2.2.2 Reconstruction

Our 3D reconstruction method is based on the registration of the combined model onto a DXA image. This is achieved by an intensity based 3D-2D registration process whereby an instance of the model, together with a pose and a uniform scale factor is found that maximizes the similarity between the DXA image and the projection of the model. Since only one projection is used, the pose is defined by three rotation values and only two translation values perpendicular to the projection direction.

In Fig. 2.11, the flow chart of the model registration process is depicted. At each iteration, a projection of the model is generated commonly referred to as a Digitally Reconstructed Radiograph (DRR). How this DRR is generated is explained in detail in Section 2.2.2. The similarity is evaluated with respect to the DXA image using the Mean Squared Error (MSE) similarity

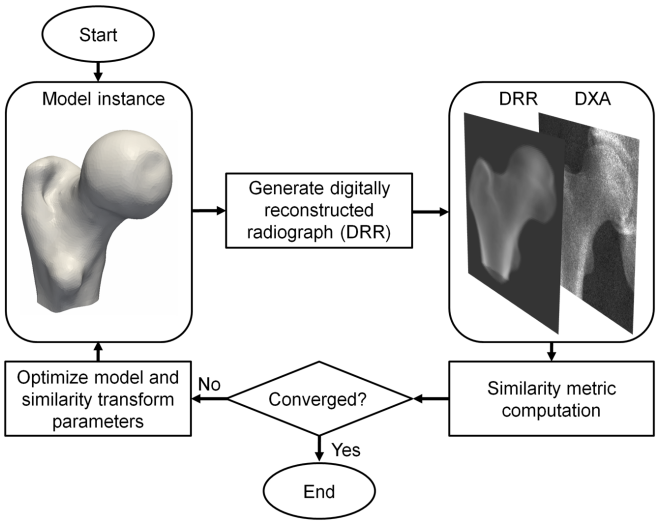

Figure 2.11: Flow chart of the iterative registration process.

measure. If the registration process has not yet converged according to this similarity measure, a new set of model and pose parameters and a new scale factor is estimated using Powell's multi-dimensional optimization method. A new model instance is generated using the new parameter set and the registration process is continued.

Although Mutual Information (MI) is a commonly used similarity measure in medical image registration, it makes no assumptions about the relation between the values. This makes it especially useful for registering different modalities. However, in our application, the values of both the projection and DXA image are of the same unit (g/cm^2). The registration process should therefore result in the same values in the DRR as in the DXA image. Although the final DRR might have a high MI similarity with the DXA image after a MI based registration process, the individual densities might not correspond at all and a reconstruction of the BMD distribution is not guaranteed. Therefore, the MSE is used in the registration process, resulting in more accurate BMD values in the resulting volume.

A mask is defined to take into account only the region of interest in the registration process (Fig. 2.12). A thresholding is applied to the DXA image to generate an initial mask, which is grown to include area around the bone boundary. In the DXA images, the femur head is partially overlapped by the pelvis. In an intensity based registration process, this region will introduce an error to the similarity measure and thus to the final reconstruction accuracy. To overcome this, the part where the pelvis is overlapping with the femur head is manually removed from the mask. In addition, the bottom part of the femur shaft is removed from the mask where the model can not reach.

Since the femur is always in the same general orientation (patient lying

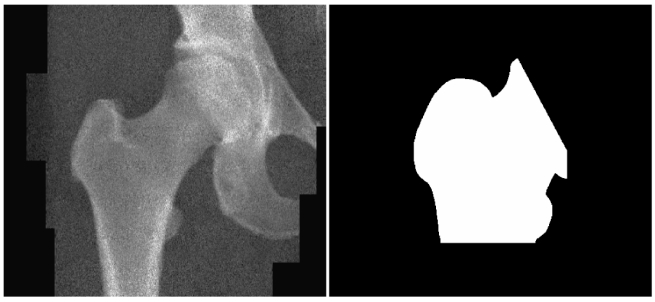

Figure 2.12: The mask (right) generated from the DXA image (left) to be used in the registration process, whereby the area overlapping with the pelvis and the bottom part of the shaft is manually removed.

on a table with straight legs and the foot positioned in a 60 degrees angle), no manual initialization of the rotation is required. Furthermore, the model is initialized by the average instance i.e., all model parameters set to 0. The model is automatically centered onto the mask and a first registration process is performed on the rotation, translation and scale parameters only. This results in an initial alignment of the model onto the DXA image. This is followed by the full registration process, optimizing all model parameters.

Throughout the registration process, the model instance is constrained to three times the standard deviation from the mean to maintain a valid femur throughout the registration process. This means that at each iteration, the model parameters are checked and corrected accordingly.

The resulting final model instance, with the corresponding surface mesh and volume containing the BMD distribution, is then considered the patient-specific reconstruction.

Digitally Reconstructed Radiograph

DXA works by passing two X-ray beams, one of a high energy and the other of a low energy, through a tissue region. The amount of absorption by the bone can be calculated and can be converted to a measure of the BMC. Thus, by performing such scan over a region of interest, an image of the projected BMD is computed.

The narrow-angle fan beam used by GE Healthcare's Lunar iDXA device results in a DXA image that is essentially without magnification. This is accomplished by overlapping the narrow-angle fan-beam sweep line images by which the distance of the object to the plane can be measured (Fig. 2.13). Thus, the DRR can be approximated by an isometric projection, removing the necessity for camera calibration.

The DRR is generated using a ray casting technique [15] resulting in a 2D image representing the areal BMD (g/cm^2). For each position in the DRR, a ray is cast through the volume in the direction of the projection perpendicular to the plane of the DXA image. The projected density value

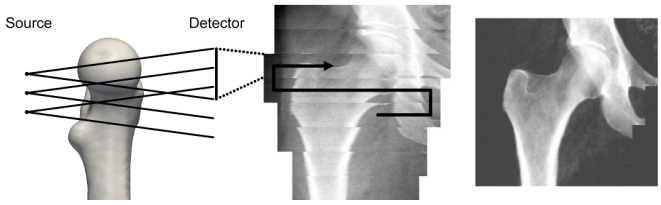

Figure 2.13: DXA image acquisition and processing. From left to right: An illustration of the narrow-angle fan-beam, the overlapping image strips resulting from the sweeps of the fan beam device for one of the two energies and the DXA image after combining the strips and calculating the BMD from the two energies.

is then defined as the integral of the new model instance X (2.12) for every point γ lying on the ray $\Gamma_{\mathbf{q}}$. The areal BMD at position $\mathbf{q}$ of the DRR can thus be formulated as:

$$\mathrm{DRR}(\mathbf{q}) = \int_{\Gamma_{\mathbf{q}}} X(\gamma) d\gamma \approx \sum_{\mathbf{r} \in R_{\mathbf{q}}} X(\mathbf{r}) \cdot d. \tag{2.13}$$

Here, an approximation is made by taking a set of sample points $R_{\mathbf{q}}$ at regular intervals of length d along the ray $\Gamma_{\mathbf{q}}$.

In [65], the QCT derived areal BMD ($\mathrm{BMD_{QCT}}$) was shown to be systematically lower than the areal BMD from DXA ($\mathrm{BMD_{DXA}}$) because of the difference in the techniques and standards. It also showed that it is possible to correct for these absolute differences by a linear conversion equation.

We performed a rigid 3D-2D intensity based registration of a subset of 30 segmented QCT volumes onto the same subject DXA images and the projected values were regressed against the DXA values. The linear regression gave us the following conversion equation:

$$\mathrm{BMD_{DXA}} = (\mathrm{BMD_{QCT}} + 0.100)/0.967 \; g/cm^2. \tag{2.14}$$

This equation was subsequently used to correct the simulated DXA image values.

2.2.3 Evaluation

For the method evaluation experiments, the left proximal femur was chosen. 30 QCT-DXA pairs were selected for the validation of the reconstruction method (mean age of 55 ± 13 years, 15 male and 15 female). They consist of 4 osteoporotic, 13 osteopenic and 13 healthy subjects with an average femur neck BMD of $0.9 \pm 0.2 g/cm^2$ ranging between 0.7 and $1.2 g/cm^2$. Of the remaining 85 QCT volumes, consisting of 27 men and 58 women with a mean age of 55 ± 12 years, the model was constructed. This set includes 3 osteoporotic, 30 osteopenic and 52 healthy subjects with average femur neck BMD of $0.9 \pm 0.2 g/cm^2$ ranging between 0.7 and $1.4 g/cm^2$.

Prior to analyzing the reconstruction accuracy, each QCT volume of the validation dataset was rigidly aligned with the corresponding DXA image

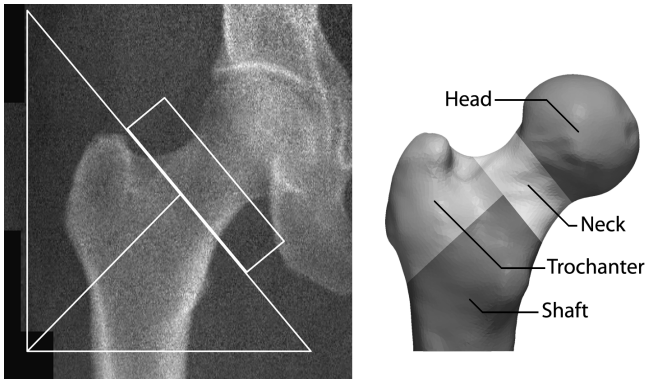

Figure 2.14: The regions on the DXA image as defined by the software of GE Healthcare (left) and the same regions shown on the manually segmented surface mesh of the same subject QCT scan (right), which, in a 3D-2D intensity based registration process, was aligned with the DXA image.

by means of an intensity based 3D-2D registration process using the MSE similarity metric and Powell's multi-dimensional optimization method. This results in the correct patient-specific pose of the ground truth QCT volume to be used in further analysis and allowed us to extract the regions as defined in the GE Lunars software platform, enCORE.

Three regions were defined: the femur neck, trochanter and shaft. The region of the femur head was deduced from these regions. In Fig. 2.14, the DXA image with the regions as defined in the enCore software is shown together with the regions on the segmented surface mesh of the aligned QCT volume. In addition, a global region was defined, which consists of the femur neck, trochanter and shaft together.

The model was constructed of the entire proximal femur, including the whole femur head. Thus, although the part of the femur head overlapping with the pelvis was removed from the mask, the entire femur head was reconstructed and evaluated together with the other regions.

To evaluate the shape reconstruction accuracy, every bone in the QCT volumes (which were previously aligned with the same subject DXA images) of the validation dataset was segmented (again using ITK-SNAP) and for each segmentation the surface mesh was constructed. These were then considered the ground truth for the individual shapes.

Each mesh resulting from the reconstruction process was then registered with the corresponding ground truth surface mesh by an Iterative Closest Point (ICP) algorithm, taking into consideration only the global region. The reconstruction error in terms of shape for each of the regions was then defined by the point-to-surface distances of the vertices in the reconstructed shape mesh to the ground truth surface mesh.

Since only a single view is used in the reconstruction process, there is little information about the actual orientation of the bone. Not estimating the orientation properly might considerably affect the reconstruction accuracy. To

examine the accuracy of the orientations resulting from the reconstructions, also the rotations (coronal, axial and sagittal) following from the previously described ICP registrations are evaluated.

To evaluate the reconstruction accuracy of the BMD distribution, the point correspondences computed to evaluate the shape accuracy were used to deform the reconstructed volume to the ground truth volume by means of a TPS transformation (using a subset of 200 control points). This way, the BMD distribution accuracy can be evaluated without taking into account the error introduced by the reconstructed shape.

Each voxel within the bone of the TPS deformed reconstruction was subsequently compared with the corresponding voxel in the ground truth volume and the voxel-by-voxel differences then determined the BMD distribution reconstruction error. In addition, the error was compared to the entire range of densities in the corresponding region, giving a percentage error of the BMD distribution reconstruction.

Apart from the reconstructed shape and BMD distribution, also the more clinically relevant volumetric BMD (vBMD, the average voxel density in a given region) was evaluated. For each region, the vBMD was compared with the vBMD extracted from the registered ground truth QCT volume. In addition, a regression was computed to analyze the linear statistical relationship.

2.3 Results

The results of the reconstructions of three subjects with varying shape and BMD quality are shown in Fig. 2.15. In Fig. 2.16, for three subjects, the cross-sections of the ground truth QCT volume at the intertrochanter and the femur neck (Fig. 2.10) as well as the coronal section are shown together with the same cross-sections from the reconstructed volumes. These figures illustrate the capacity of the model to successfully reconstruct these large variations in shape and BMD distribution from a single DXA image.

In Table 2.1, the results of the shape reconstruction accuracy for the selected regions is given. The best accuracy can be seen at both the femur neck and the trochanter area with both having an average point to surface distance of $1.0mm$ and 2RMS error of $2.6mm$. The femur head gives the least accurate point to surface distances with a mean error of $2.0mm$ and 2RMS error of $4.9mm$.

In Fig. 2.17, an error map illustrates the point-to-surface distances for every vertex of the shape model averaged over all 30 subjects. From this, we can see that the lesser trochanter imposes a lot of error in the shaft region, which explains the relative large error compared to the other regions.

The ICP registrations aligning the reconstructed shapes with the ground truth surface meshes resulted in a mean rotation error of 3.0° (2RMS of 7.8°) coronal, 2.4° (2RMS of 6.3°) axial and 0.4° (2RMS of 1.1°) sagittal.

Analyzing the reconstruction accuracy of the BMD distribution, we found the average voxel-by-voxel error to be below $85mg/cm^3$ for all regions. The error relative to the whole range of BMD values was around the 5% for all

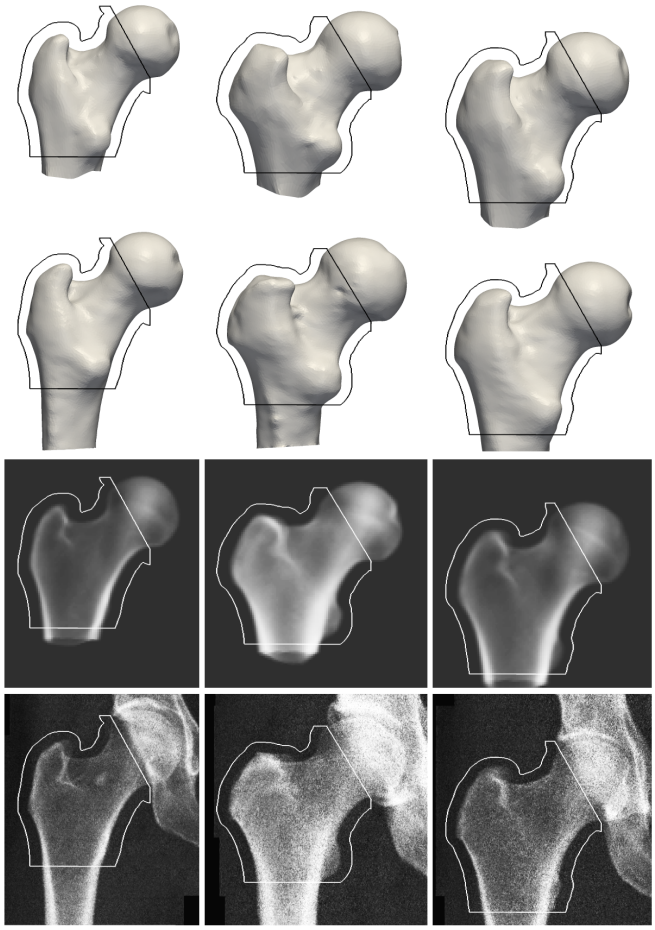

Figure 2.15: Results of three of the reconstructions with the contours of the masks used in the registration process. From top to bottom: the reconstructed shape, the ground truth surface mesh, the DRR generated by projecting the resulting model instance and the DXA image.

Table 2.1: Accuracy of the reconstructions of the shapes, given as the point to surface distances (mm).

Region	Mean	2RMS*	Max
Neck	1.0	2.6	5.6
Trochanter	1.0	2.6	5.9
Shaft	1.2	3.4	9.2
Global	1.1	2.9	9.2
Head	2.0	4.9	8.2

* 95% confidence interval.

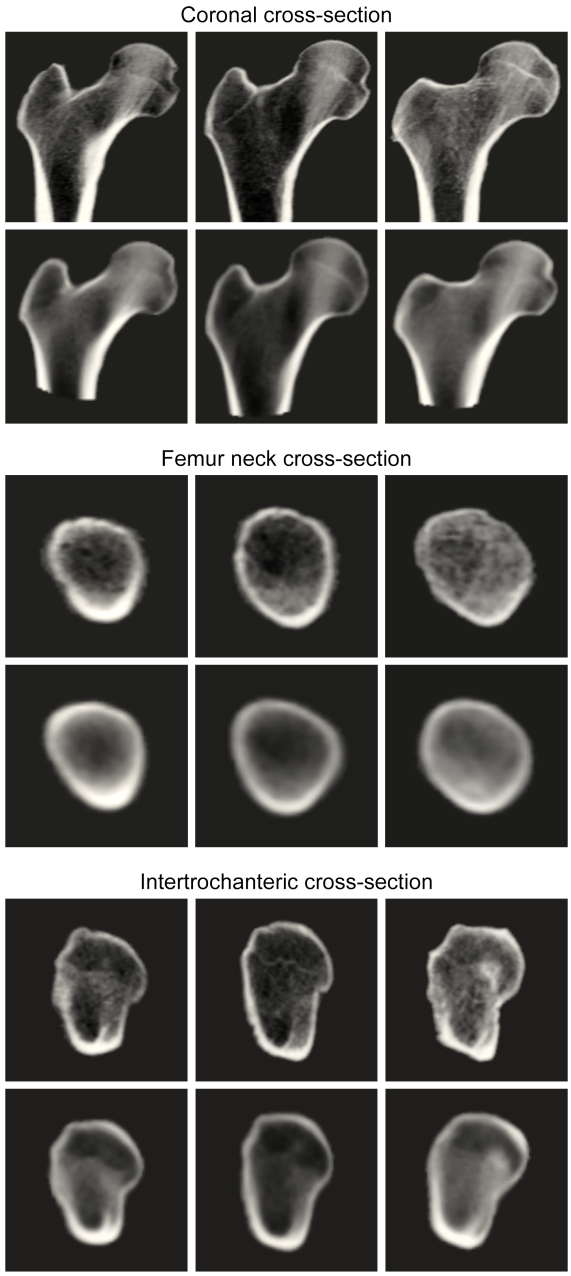

Figure 2.16: The cross-sections at three regions for three subjects (each column represents a single subject) of the segmented ground truth QCT volumes (top) and the corresponding reconstructed volume (bottom). All image have the same window level.

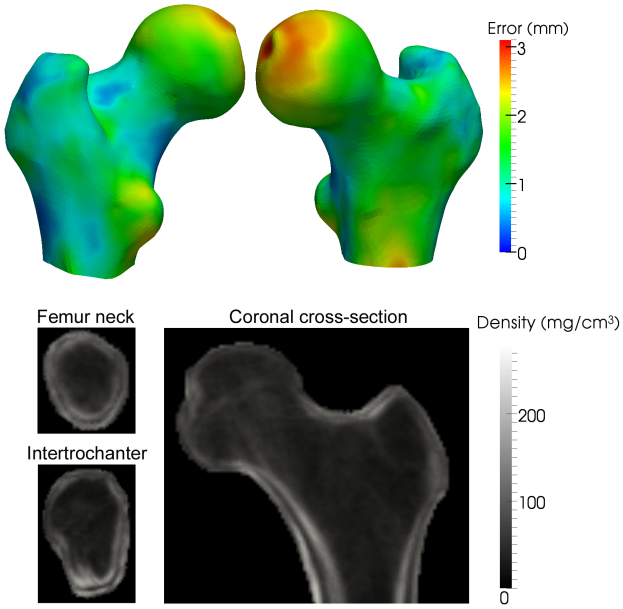

Figure 2.17: The color-coded point to surface distances (mm) between the reconstructed shapes and the QCT-derived surfaces (top) and the BMD reconstruction errors presented with respect to the mean shape (bottom), averaged over the 30 subjects.

regions, with a slight increase at the shaft of 5.7%. In Table 2.2, the error of the BMD distribution is given for each of the regions.

To visualize the distribution of the BMD errors, the volumes representing the BMD errors were aligned to the mean shape and averaged over all 30 subjects. Subsequently, the femur neck, intertrochanter and coronal cross-sections are shown in Fig. 2.17.

In Fig. 2.18 the scatter plots of the vBMD acquired from QCT, set against the vBMD from the reconstructions are shown. In Table 2.3 the correlation coefficient (r), the offset and slope is given. All regions, apart from the femur head, show a strong correlation ($r > 0.9$) and are all statistically significant ($p < 0.001$).

The one-dimensional scatter plots of the mean shape errors, the mean BMD distribution errors and the volumetric BMD errors for all 30 subjects are shown in Fig. 2.19. This gives an indication of the distribution of the errors over the validation set.

Regarding the computation time, one iteration of the model construction process using 85 volumes took approximately 21 hours and one reconstruction takes approximately one hour on an Intel®Core™ i7 CPU 920 @ 2.67GHz processor. At this point, no effort was put into improving the computation time using multi-processor or GPU acceleration.

Table 2.2: BMD distribution reconstruction error (mg/cm^3) for the different regions. The percentages indicate the error with respect to the full range of bone densities in the corresponding region.

Region	Mean	2RMS*	Max
Neck	71.0(5.1%)	205.5(14.8%)	981.0(70.7%)
Trochanter	60.8(4.6%)	182.1(13.7%)	952.5(71.8%)
Shaft	84.1(5.7%)	252.2(17.2%)	1267.0(86.4%)
Global	72.0(4.9%)	217.2(14.8%)	1267.0(86.4%)
Head	53.9(4.6%)	149.0(12.8%)	783.5(67.5%)

* 95% confidence interval.

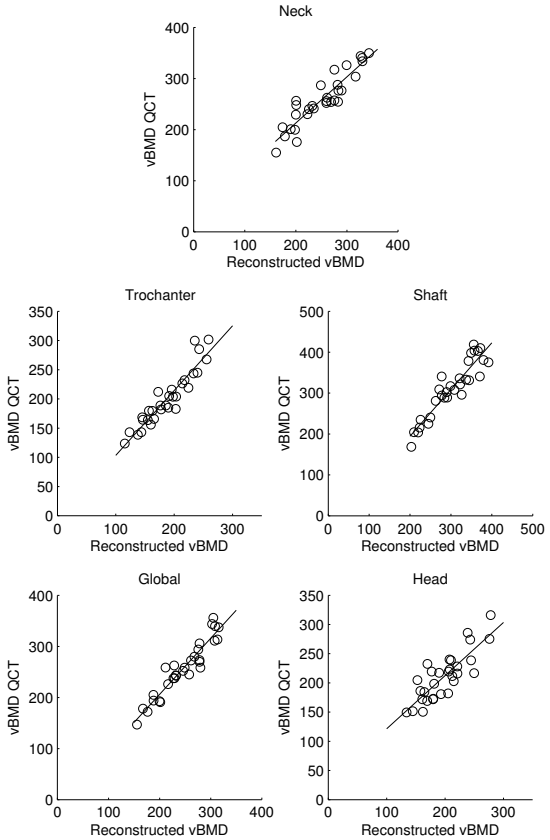

Figure 2.18: Scatter plots and regression lines for all the regions visualizing the correlation between the QCT derived vBMD (vBMD QCT) and the vBMD resulting from the reconstructions (Reconstructed vBMD). The correlation coefficient, offset and slope values are given in Table 2.3.

Table 2.3: The error (mg/cm^3) and correlation values between the QCT derived vBMD and the vBMD resulting from the reconstructions for all regions.

Region	MAE†	2RMS*	Max	r	Offset	Slope
Neck	17.2	44.3	55.8	0.92	32.4	0.90
Trochanter	15.3	42.5	64.8	0.94	−7.5	1.11
Shaft	21.8	56.2	63.2	0.93	−33.6	1.14
Global	15.9	40.8	50.8	0.95	−13.4	1.10
Head	20.5	52.0	62.8	0.83	30.3	0.91

† Mean Absolute Error.
* 95% confidence interval.

2.4 Discussion

For the global shape accuracy, which excludes the femur head, we obtained a average error of $1.1mm$ and a 2RMS error of $2.6mm$, whereas in Zheng *et al.* [119] an average mean reconstruction error of $1.2mm$ was reported using 2 views for each femur. These reconstructions, however, were performed on X-ray images while a reconstruction from DXA is a considerably more challenging task due to the high level of noise present in DXA images. On the other hand, by using a model of the BMD distribution, our method can take advantage of the density information in the DXA images.

In Kolta *et al.* [67], where the proximal femur shape was reconstructed from two DXA images (frontal and sagittal), a mean point to surface distance of $0.8mm$ and a 2RMS error of $2.1mm$ was reported. This method and the method of Zheng *et al.*, however, rely on two projections and are limited to the shape reconstruction only, whereas the reconstruction method presented in this work requires only one DXA image and results in a reconstruction of the shape as well as the BMD distribution.

The comparably large error in the femur head can be explained due to the fact that a large part of this region was not considered in the reconstruction process, and thus was merely estimated. The reconstruction of the BMD distribution on the other hand shows a larger accuracy at the femur head compared to the other regions. This in turn can be explained by the thin layer of cortical bone in this region, which gives a rather small error in comparison to the other regions.

The mean rotation error in the coronal 3.0° (2RMS of 7.8°) and axial 2.4° (2RMS of 6.3°) direction suggests an improvement in the reconstruction accuracy is possible if this part is properly addressed.

Analyzing the BMD distribution reconstruction accuracy in the global region, a mean error of $72.0mg/cm^3$ corresponding to 4.9% of the range of bone densities in this region was measured with a 95% confidence interval of $217.2mg/cm^3$ corresponding to 14.8% of the total range of bone densities. A volume reconstruction accuracy of the whole proximal femur is given in Fritscher *et al.* [38] whereby the error corresponds to 3.6% of the whole intensity range. This however was the result of the registration of a statistical

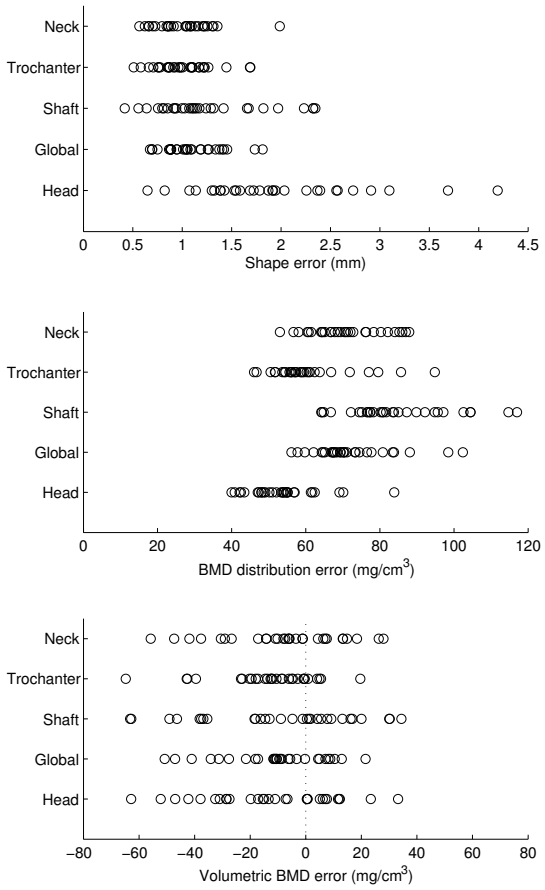

Figure 2.19: One-dimensional scatter plots of the mean shape errors (top), mean BMD distribution errors (center) and volumetric BMD errors (bottom) of the 30 subjects.

model onto a volume, as opposed to our reconstruction method from a single projection.

A comparison of the BMD distribution error can be made with the residual error, which represents the expected error assuming a perfect reconstruction. The closeness of the range of density errors (considering the densities range between -150 and $1300 mg/cm^3$ approximately) is thus an indication of the accuracy in which the BMD distribution is reconstructed.

In Ahmad *et al.* [2], similar results are presented regarding the reconstruction of the vBMD. Here a correlation coefficient of 0.81 is reported for the narrow neck and 0.89 for the intertrochanter. In comparison, our method resulted in a correlation coefficient of 0.92 and 0.94 for the femur neck and the trochanter region, respectively.

Volumetric BMD has been shown to be strongly related to the bone strength [70][11] and has been shown to highly correlate with fracture inci-

dence [9][58]. The accurate vBMD reconstruction therefore shows the clinical relevance of this work and the potential to improve the fracture risk estimation from DXA over current methods.

The statistical model presented in this work is distinct from most proposed models in the way that the variations in the BMD distribution is captured by the density model only, whereas other methods use the shape [114] or deformation field [37] to also describe the internal structure. This will allow us to examine the BMD distribution independent from the shape which can potentially be useful for diagnosing patients, considering osteoporosis affects only the BMD distribution and not the shape of the bone. Furthermore, to determine which type of model performs best with respect to the reconstruction accuracy, the evaluations need to be performed on the same patient population. The fact that no standard dataset was used in our and previous work should be taken into consideration when examining the results in comparison with other research.

Although the model construction method is still not fully automatic due to the manual removal of the pelvis area, this can potentially be automated by incorporating a Hough filter for detecting spherical objects in the volume [123].

Regarding the reconstruction process, the method is automatic and non-supervised, except for the manual removal of the pelvis region from the DXA mask. This too, however, can be automated as is done by the software of GE Healthcare to define the regions of interest.

One limitation in this study is the relative young population and, subsequently, the limited number of osteoporotic patients used for the model construction. Although emphasis is put on the reconstruction accuracy and not pathology detection, bone loss due to osteoporosis might result in a more varied BMD distribution and bone restructuring, which might have an effect on the reconstruction accuracy. The evaluations, however, were performed on healthy subjects as well as osteoporotic and osteopenic patients, and the results therefore represent the possibility to reconstruct also these pathological cases.

Although in this work we have presented a method that can reconstruct the 3D shape and BMD distribution from a single DXA image, the method can as well be applied to a multi-view reconstruction. Although a multi-view reconstruction is expected to increase the reconstruction accuracy, the devices capable of multi-view DXA acquisitions are still expensive and not as widely used in clinics as single-view devices. Some preliminary experiments have been performed on simulated DXA images of specimen to evaluate to what extent using multi-view DXA improves the reconstruction accuracy over a single-view [56]. However, by using specimen data, these experiments do not take into account the pelvis overlap which limits the view angles that can be used when reconstructing the femur from real DXA images.

2.5 Conclusion

This work presents a method to reconstruct both the 3D shape and BMD distribution from a single DXA image by the registration of a statistical model. A statistical model of the combined shape and BMD distribution is introduced, together with a method for its construction. An iterative updating of the reference shape and volume is incorporated to remove any bias in the reference selection and to increase the accuracy of the individual registrations. In an intensity based 3D-2D registration process, an instance of the model is found, which maximizes the similarity between the DXA image and the projection of the model. By using statistics on the combined 3D shape and BMD distribution of a large population, the limitations of a single 2D DXA image can be overcome. Comparisons between the reconstructed femur and ground truth show that this method results in accurate and realistic reconstructions.

This method is fully compliant with clinical routine since clinically deployed DXA scanners are mostly limited to the acquisition of a single view. This opens the way for a better diagnosis of osteoporosis by providing a detailed 3D analysis of the femur from routine, low cost, and low radiation dose 2D DXA imaging devices.

Although this work has put the focus on the proximal femur, vertebral fractures are in fact the most common type of osteoporotic fractures, and although many vertebral fractures remain undiagnosed, they can have a severe impact on the quality of life and are accompanied by increased mortality [51]. The method presented in this work will therefore be extended to allow the reconstruction of the lumbar vertebrae from DXA images.

Our future work aims at improving fracture risk assessment from DXA by using accurate information of the 3D shape and BMD distribution obtained by the presented reconstruction method. Statistical models of the proximal femur have already been used successfully to predict biomechanical parameters [38] and to analyze the trabecular bone of the proximal femur [36]. Although we have shown to be able to successfully and accurately reconstruct the 3D shape and BMD distribution from DXA, additional effort to improve the accuracy is expected to be necessary for this complex analysis.

Including older subjects in the statistical model might improve the reconstruction accuracy of the targeted population. However, older people have a greater incidence of arthritis and other conditions that can affect the shape of the bone. This might negatively affect the statistical model unless a large population is used. Towards this end, a more extensive database will be collected. In addition this will allow the construction of a separate model for male and female subjects and containing more pathological cases. This is expected to improve the reconstruction accuracy for a specific pathology and gender.

Efforts are also being put forth to allow finite element analysis on the reconstructed femurs with the aim of providing a measure of the femur strength.

We aim to eventually demonstrate that the advantages of a 3D analysis

on fracture risk assessment accuracy can be implemented in clinical practice, maintaining DXA as the current standard modality.

3

Hip Fracture Discrimination from Dual-energy X-ray Absorptiometry by Statistical Model Registration

In this chapter the parameter values resulting from the registration of the statistical model onto DXA images are evaluated for their hip fracture discrimination ability with respect to regular DXA derived areal BMD measurements. Compared to the previous chapter the model construction method was improved with a simplified pipeline. However, the shape and density model remain decoupled which allows for the separated evaluation of the parameters with respect to the fracture discrimination. The registration method has remained the same which the exception of optimizing both shape and density model parameters. The statistical model was constructed from a large database of QCT scans of females with an average age of 67.8 ± 17.0 years. This model was subsequently registered onto the DXA images of a fracture and control group. The fracture group consisted of 175 female patients with an average age of 66.4 ± 9.9 years who suffered a fracture on the contra lateral femur. The control group consisted of 175 female subjects with an average age of 65.3 ± 10.0 years and no fracture history. The discrimination ability of the resulting model parameter values, as well as the areal BMD measurements extracted from the DXA images were evaluated using a logistic regression analysis.

The content of this chapter is adapted from the following publications:

T. Whitmarsh, K.D. Fritscher, L. Humbert, L.M. del Ro Barquero, T. Roth, C. Kammerlander, M. Blauth, R. Schubert, A.F. Frangi, Hip Fracture Discrimination from Dual-energy X-ray Absorptiometry by Statistical Model Registration, submitted 2012.

and

T. Whitmarsh, K.D. Fritscher, L. Humbert, L.M. del Ro Barquero, T. Roth, C. Kammerlander, M. Blauth, R. Schubert, A.F. Frangi, A Statistical Model of Shape and Bone Mineral Density Distribution of the Proximal Femur for Fracture Risk Assessment, *Medical Image Computing and Computer-Assisted Intervention*, vol. 6892, pp. 393-400, 2011.

3.1 Introduction

Hip fractures of elderly people can primarily be explained by the presence of osteoporosis. Osteoporosis is a skeletal disease characterized by the development of a low BMD and increased bone fragility, which subsequently increases the risk of fracture. Up to 20% of patients die in the first year following a hip fracture, and only about one-third of survivors regain their original level of function [111]. The loss of bone density progresses with advancing age and the increase in life expectancy will subsequently result in an increased fracture incidence. An estimated 1.3-1.7 million hip fractures occurred worldwide in 1990 and this number is expected to increase to almost 3 million by 2025 [111]. An accurate means to diagnose osteoporosis and to reliably estimate the risk of fracture therefore becomes ever more important.

Fracture risk assessment currently relies on areal BMD measurements from DXA. Although a low areal BMD has been shown to be strongly correlated with fracture incidence, this measure is limited by its two-dimensionality while the spatial distribution and geometry of the bone to a large extent determines the bone strength [81]. A volumetric image of the bone densities can be acquired using QCT. Here, an external bone mineral reference phantom is included with a regular CT scan to convert the CT values to density values. From this density volume, various parameters can be extracted such as the volumetric density of the cortical and trabecular bone as well as geometric and structural parameters such as the cortical thickness, the femoral neck length, the neck shaft angle and the section modulus. These have been shown to be important measurements for determining the femoral strength [11][21][70] and deriving a fracture risk [58][12]. This modality, however, administers the patient with a relatively high dose of radiation compared to DXA. In addition, the high cost and limited access to CT scanners prevents this modality from being used in clinical routine and thus DXA remains the current clinical standard for bone quality measurements and fracture risk assessment.

To overcome the limitations of DXA, several methods have been proposed to acquire a 3D reconstruction from a regular DXA image by incorporating a statistical model in an intensity-based registration process [110][2]. From these reconstructions the same parameters can be extracted as from QCT. However, these parameters are still limited descriptors of the shape and spatial distribution of the bone. Several authors propose the use of Finite Element Analysis (FEA) of bones to determine their mechanical behavior [63][90][89]. Although FEA has been shown to accurately estimate the resistance to specific loading conditions, their direct relation to the risk of fracture has not yet been fully established. In [76] a method was developed for a more detailed analysis of the spatial distribution of the bone using deformable registrations and image similarities. This method was shown to be able to accurately discriminate between fracture patients and controls and was used to identify the regions within the femur which are most strongly associated with hip fracture [74].

Recently, statistical models as pioneered by Cootes *et al.* [25] have re-

ceived a great deal of interest as a means to analyze the complex morphometry of organs for the diagnosis of diseases and detection of symptoms. Statistical models of the shape and motion of the heart are being developed for detecting pathologies such as hypertrophic cardiomyopathy and the distribution of brain gray matter has been analyzed in statistical brain atlases with respect to Alzheimer's disease, schizophrenia and the risk of healthy subjects for developing these disorders.

Both in [4] and [46] the femoral shape was analyzed from planar radiographs using statistical shape modelling, and the association of the modes of variation with the fracture incidence was examined. In [47] this method was extended by including an analysis of the trabecular bone structure, which significantly improved the hip fracture discrimination ability. These methods, however, are still limited by a two-dimensional analysis from radiographic projections. In recent work, Li et al. [75] constructed a statistical model of the volumetric density distribution of the proximal femur and analyzed the model parameters for their hip fracture discrimination power. Here, only the density distribution was analyzed while also the shape determines the femoral strength and shape parameters have been shown to be independent hip fracture discriminators [11]. In [36] a statistical model of shape and appearance was presented and the parameters of this model were, in other work, analyzed for their ability to predict the fracture load of the proximal femur [100]. Although the fracture load gives a measure of the bone strength, it does not directly relate to the risk of fracture.

Previously, we developed a statistical model of both the 3D shape and BMD distribution of the proximal femur for fracture risk assessment [108]. This model is constructed from a large dataset of QCT volumes using an intensity based registration process. The parameters of this model describe the global shape and spatial distribution of the bone and were shown to correctly represent the shape and density variations that determine the fracture risk. In other work this model was shown to be able to accurately reconstruct the 3D shape and BMD distribution of the proximal femur by registering it onto a single DXA image, whereby the proximal femur was reconstructed with a mean shape accuracy of $1.1mm$ and a global BMD distribution error of 4.9% [110]. In this study we aim to evaluate the parameters of the statistical model resulting from the registration onto DXA for their ability to improve the hip fracture discrimination from DXA with respect to regular areal BMD measurements.

3.2 Materials and Methods

3.2.1 CT dataset for statistical model construction

For the construction of the statistical model a dataset of CT scans of the pelvis area of 80 fracture patients was collected at the Department for Trauma Surgery, Medical University Innsbruck (Innsbruck, Austria), using the GE LightSpeed VCT Multi Slice CT device (GE Healthcare, Chalfont St. Giles, UK). The patients were all female with an average age of 80.8 ± 10.1

years and all had suffered a proximal femur fracture. From this set the contralateral un-fractured femurs were taken, which can be justified by research on proximal femur symmetry[32], and this set defined the high fracture risk group. The European forearm phantom [97] was included into every scan acquisition to convert the CT scans to QCT volumes.

This dataset was supplemented by a control group of 80 (all female) patients which was collected at the CETIR Medical Center (Barcelona, Spain) using the Philips Gemini GXL 16 system (Philips Healthcare, Best, The Netherlands). These patients had a lower average age of 55.9 ± 11.6 years, to represent a control group with a low fracture risk and a normal BMD distribution. The CT scans were calibrated using the Mindways calibration phantom (Mindways Software Inc., Austin, TX, United States).

Different studies have shown that the scan device has little influence on the density calibration [39]. However, the European forearm phantom calibrates the volumes to a hydroxyapatite (HA) density, whereas the Mindways phantom is constructed of K_2HPO_4. Previous research shows that one calibration material is highly correlated to another and can be converted using a linear transformation [105]. To get the conversion formula for the phantoms in this work, both phantoms were scanned together using the Siemens scanner and the correlation between the density values was measured 3.1. In this way, the scans with the Mindways calibration phantom were converted to HA density values.

The combined dataset with an average subject age of 67.8 ± 17.0 years was subsequently used for the construction of the statistical model used in this work.

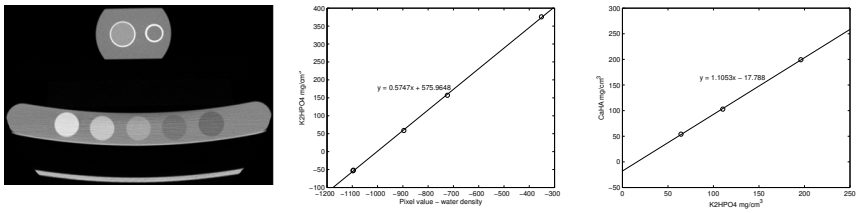

Figure 3.1: From left to right: The CT scan of the combined Mindways and European forearm calibration phantom; the linear regression to calibrate the CT scan to K2HPO4 density values using the Mindways phantom whereby the water density is subtracted from the average pixel value for each of the five rods; the linear regression between the CaHA values of the European forearm phantom and the corresponding K2HPO4 values. For the calibration to K2HPO4 density values an additional correction of the slope and intercept is required to take into consideration the physical properties of the water contained in the calibration rods and the amount of water excluded when adding K2HPO4.

3.2.2 DXA dataset for method evaluation

To evaluate the discrimination method, a database of 175 proximal femur DXA scans was collected at CETIR Grup Medic (CDP Unit Esplugues, Esplugues de Llobregat, Barcelona, Spain), whereby the contra lateral femur

Table 3.1: Baseline characteristics of subjects (mean ± standard deviation).

	Fracture	Controls	p value
Age (years)	66.4 ± 9.9	65.3 ± 10.0	0.281
Weight (kg)	65.0 ± 12.4	65.4 ± 11.0	0.735
Height (cm)	154.2 ± 6.8	154.0 ± 5.8	0.852
BMI (kg/m^2)	27.3 ± 4.8	27.5 ± 4.1	0.690
Femoral neck aBMD (g/cm^2)	0.77 ± 0.13	0.83 ± 0.13	< 0.0001
Trochanteric aBMD (g/cm^2)	0.60 ± 0.13	0.66 ± 0.14	< 0.0001
Shaft aBMD (g/cm^2)	0.91 ± 0.14	1.01 ± 0.16	< 0.0001
Total aBMD (g/cm^2)	0.80 ± 0.15	0.90 ± 0.15	< 0.0001

BMI = body mass index = $weight/height^2$; p values by Student's t test.

was fractured. The scans were performed by the GE Lunar Prodigy Bone Densitometer (GE Healthcare, Chalfont St. Giles, UK). All subjects were female with an average age of 66.4 ± 9.9 years. In addition, an age matched control group (average age of 65.3 ± 10.0 years) of 175 DXA scans of female subjects with no fracture history was collected. Exclusion criteria were hip fractures as a result from high-energy trauma and bone disease. The DXA image pixel values were subsequently converted to standardize BMD [41] which corresponds to the same hydroxyapatite (HA) density values as the QCT scans. For all DXA scans the femoral neck, trochanter, shaft and total areal BMD measurements were acquired using the GE Lunar's software platform, enCORE. The full set of baseline characteristics of the fracture and control subjects are presented in Table 3.1.

Ethical approval was granted for all data acquisitions by the Institutional Review Board and written informed consent was provided by all the subjects included in this study.

3.2.3 Shape and density model construction

The statistical shape and density model is constructed from a large dataset of QCT volumes by an intensity based registration process as depicted in Fig. 3.2. In order to prevent the pelvis area from resulting in misalignments in the registration process, in a preprocessing step the pelvis area is semi automatically removed from the QCT volumes. In addition, a thresholding is applied to remove the soft tissue structures that can negatively affect the registration process.

A reference volume is chosen based on its regular shape and BMD quality. In this volume, the bone is manually segmented and a regular mesh is constructed from this segmentation. All volumes are subsequently registered to this reference volume by an intensity based similarity registration. This is followed by a multi-scale intensity based Thin Plate Spline (TPS) registration using the mesh vertices as the control points on the reference image.

The TPS registrations result in the corresponding landmark locations on the target volumes and thus provides the surface mesh for all similarity

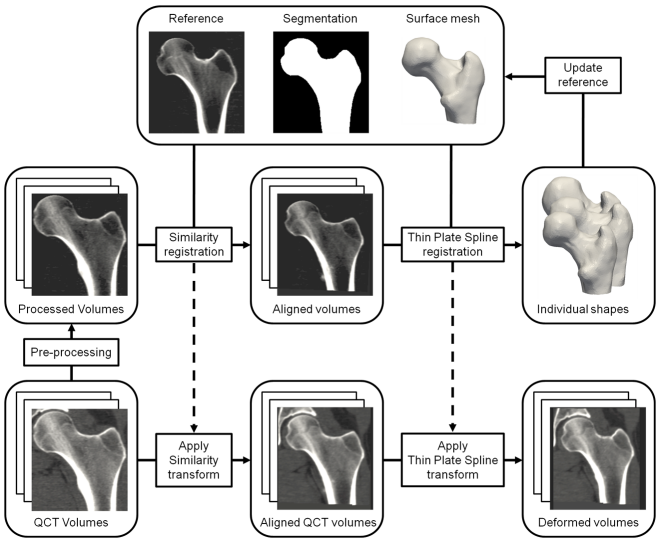

Figure 3.2: Model construction pipeline.

aligned volumes. All similarity aligned meshes are subsequently scaled to their original size using the uniform scale value resulting from the similarity transform.

To remove any bias of the reference selection, the reference volume (and the mask) are deformed to the average shape using a TPS transformation defined by the shape vertices. In a second iteration, the volumes are then registered onto this updated reference while using the average shape for the TPS registrations.

The registrations results in the set of aligned patient specific surface meshes with a vertex correspondence between them. PCA is then applied to the vertices and a new shape $\mathbf{s}$ can be expressed as the average shape $\overline{\mathbf{s}}$ and a linear combination of the first m eigenvectors corresponding to the main modes of variation:

$$\mathbf{s} = \overline{\mathbf{s}} + \sum_{i=1}^{m} \mathbf{p}_i \alpha_i. \tag{3.1}$$

Here $\mathbf{p}_i$ is the i-th eigenvector resulting from the singular value decomposition of the covariance matrix and α_i the corresponding scalar coefficient referred to here as the shape model parameter. In Fig. 3.3, the mean and first three modes of variation of the resulting shape model are presented. The first mode of variation describes the global size while the second describes the neck shaft angle, and the third describes the femoral neck length.

To model the BMD distribution, a final iteration of the registration process is performed to deform all volumes to the same average bone shape, whereafter the resulting similarity and TPS transformation is applied to the unprocessed QCT volume for each subject. This results in shape normal-

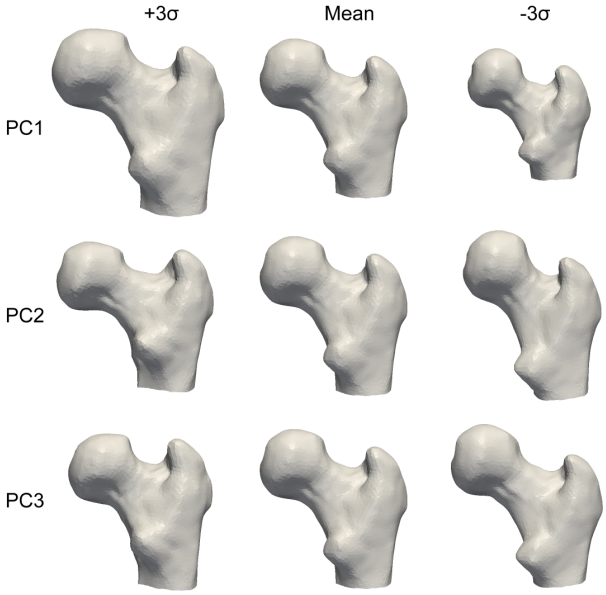

Figure 3.3: The mean shape and the first three modes of variation of the shape model, varying between +3 and -3 standard deviations.

ized volumes with a voxel correspondence between them. Since the TPS transformation is defined by landmarks on the bone surface only, the TPS interpolation preserves the internal BMD distribution. PCA is then applied to the voxel densities inside the bone so that a new volume $\mathbf{v}$ can be expressed as the average volume $\overline{\mathbf{v}}$ and the first n eigenvectors:

$$\mathbf{v} = \overline{\mathbf{v}} + \sum_{i=1}^{n} \mathbf{q}_i \beta_i. \tag{3.2}$$

Here $\mathbf{q}_i$ is the i-th eigenvector and β_i the corresponding density model parameter. Fig. 3.4 shows projections of the mean and first three modes of variation of the density model, whereby the main mode of variation describes the global density.

The model parameters thus describe the number of standards deviations from the mean for each mode of variation of both the shape and density model. For the shape model 14 modes of variation are used and 11 for the density model. These numbers were determined by Cattells scree test [14] whereby the remaining modes of variation are considered noise and are discarded (Fig. 3.5).

3.2.4 Model registration

The statistical model is registered onto a DXA image by an intensity based 3D-2D registration process (Fig. 3.6). A new instance of the model is gener-

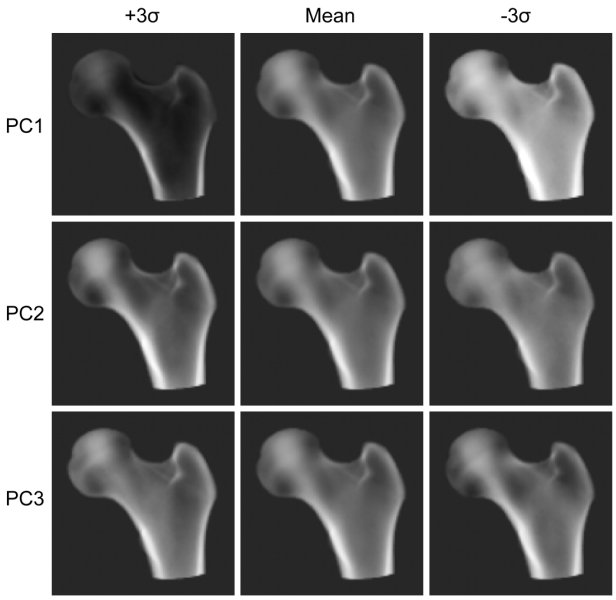

Figure 3.4: Projections of the mean and the first three modes of variation of the density model, varying between +3 and -3 standard deviations.

ated by deforming the density model instance to the shape model instance. In the registration process the model parameters, together with a pose (rotation and translation), that maximize the similarity between the DXA image and the projection of the deformed density model are found. This results in a patient specific reconstruction of the 3D shape and spatial distribution of the bone as described by the model parameters. For a detailed description of the reconstruction process we refer the reader to [110]. The statistical model was subsequently registered onto the DXA images of the fracture patients and control group.

3.2.5 Statistical analysis

The model parameters resulting from the registration onto the DXA image describe the subject specific 3D shape and internal distribution of the bone and are in this work analyzed for their ability to discriminate hip fracture. The statistical analysis was done using the SPSS Statistics package v19 (IBM, Armonk, NY). The shape and density model parameters as well as the areal BMD measurements were first analyzed individually by computing the Odds Ratio (OR) with 95% Confidence Interval (CI), which determines the association of the variable with fracture incidence. To evaluate the discrimination ability of the various measurements, the Receiver Operating Curve (ROC) was analyzed whereby the Area Under the Curve (AUC) with corresponding 95% CI was reported. To analyze the contribution of the shape and

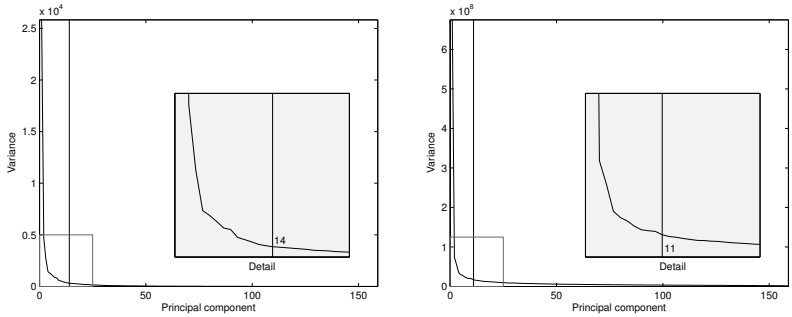

Figure 3.5: Scree plots of the shape (left) and density model (right), whereby the graph appears to have leveled off at respectively the 14th and 11th principal component.

Table 3.2: Results of the logistic regression (adjusted for age, weight, height and BMI) and the ROC analysis using the shape model parameters.

	OR [95% CI]	p value	AUC [95% CI]
Mode 1	0.639 [0.477 - 0.857]	0.003	0.586 [0.526 - 0.645]
Mode 2	1.229 [1.042 - 1.451]	0.014	0.575 [0.515 - 0.635]
Mode 3	1.009 [0.861 - 1.182]	0.913	0.502 [0.441 - 0.562]
Mode 4	0.913 [0.777 - 1.072]	0.267	0.535 [0.474 - 0.595]
Mode 5	1.061 [0.923 - 1.221]	0.404	0.527 [0.466 - 0.588]
Mode 6	1.092 [0.914 - 1.305]	0.331	0.529 [0.468 - 0.589]
Mode 7	1.055 [0.918 - 1.213]	0.451	0.525 [0.465 - 0.586]
Mode 8	0.880 [0.771 - 1.005]	0.059	0.561 [0.501 - 0.621]
Mode 9	0.934 [0.804 - 1.086]	0.374	0.517 [0.457 - 0.578]
Mode 10	0.715 [0.587 - 0.870]	0.001	0.599 [0.540 - 0.659]
Mode 11	0.746 [0.620 - 0.899]	0.002	0.593 [0.533 - 0.652]
Mode 12	0.965 [0.839 - 1.110]	0.615	0.511 [0.451 - 0.572]
Mode 13	0.997 [0.845 - 1.177]	0.970	0.503 [0.442 - 0.563]
Mode 14	0.947 [0.836 - 1.071]	0.385	0.524 [0.464 - 0.585]

density distribution separately, the 14 shape model parameters as well as the 11 density model parameter values were used as independent variables in logistic regression models. Both the shape and density model parameters were subsequently combined in a logistic regression evaluation. As a comparison, the areal BMD values of the same subjects were evaluated and combined in a second logistic regression model to determine to what extent the areal BMD measurements can discriminate between the fracture and non-fracture group. Finally, the 14 shape model parameters, the 11 density model parameters and the areal BMD values were evaluated for their combined discrimination ability.

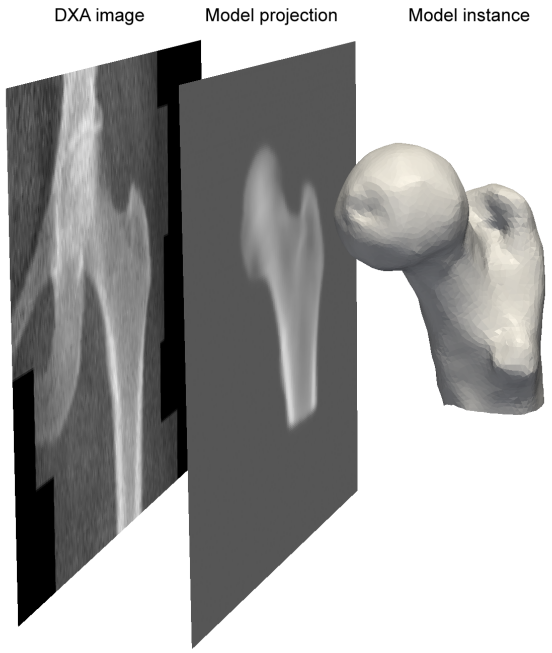

Figure 3.6: The registration of the statistical model onto a DXA image.

Table 3.3: Results of the logistic regression (adjusted for age, weight, height and BMI) and the ROC analysis using the density model parameters.

	OR [95% CI]	p value	AUC [95% CI]
Mode 1	0.361 [0.256 - 0.509]	< 0.001	0.672 [0.616 - 0.728]
Mode 2	1.109 [0.884 - 1.392]	0.370	0.518 [0.457 - 0.578]
Mode 3	0.803 [0.657 - 0.981]	0.032	0.567 [0.507 - 0.627]
Mode 4	1.063 [0.906 - 1.247]	0.453	0.534 [0.473 - 0.595]
Mode 5	1.149 [0.991 - 1.333]	0.066	0.555 [0.495 - 0.616]
Mode 6	0.789 [0.665 - 0.935]	0.006	0.579 [0.520 - 0.639]
Mode 7	0.975 [0.821 - 1.157]	0.768	0.516 [0.455 - 0.576]
Mode 8	0.841 [0.716 - 0.988]	0.035	0.564 [0.504 - 0.624]
Mode 9	0.954 [0.810 - 1.122]	0.568	0.526 [0.466 - 0.587]
Mode 10	1.261 [1.093 - 1.455]	0.001	0.591 [0.532 - 0.650]
Mode 11	1.060 [0.899 - 1.249]	0.490	0.529 [0.469 - 0.590]

Table 3.4: Results of the logistic regression (adjusted for age, weight, height and BMI) and the ROC analysis using the areal BMD measurements.

	OR [95% CI]	p value	AUC [95% CI]
Femoral neck aBMD	2.010 [1.503 - 2.688]	< 0.001	0.638 [0.581 - 0.696]
Trochanteric aBMD	1.866 [1.417 - 2.457]	< 0.001	0.641 [0.583 - 0.699]
Shaft aBMD	2.622 [1.927 - 3.568]	< 0.001	0.680 [0.625 - 0.736]
Total aBMD	2.909 [2.095 - 4.039]	< 0.001	0.686 [0.631 - 0.742]

OR and 95% CI per 1SD decrease of BMD.

Table 3.5: AUC values resulting from logistic regression analysis on the various model parameter and areal BMD measurement combinations.

	AUC [95% CI]	R^{2*}
Shape model parameters	0.683 [0.628 - 0.739]	0.133
Density model parameters	0.719 [0.666 - 0.772]	0.193
All model parameters	0.752 [0.701 - 0.803]	0.242
BMD	0.802 [0.757 - 0.848]	0.293
BMD + All model parameters	0.840 [0.799 - 0.881]	0.395

BMD = areal BMD measurements of the femoral neck, trochanteric, shaft and the total areal BMD.

* Nagelkerke R^2.

3.3 Results

First, the relationships of the individual model parameters with the hip fracture incidence are examined. In Table 3.2 and 3.3 the ORs and AUC values are given for the shape and density model parameters individually. The 1st mode of variation of the shape model corresponding to the scale (Fig. 3.3) has a strong association with the fracture incidence with an OR of 0.639 (95% CI 0.477 - 0.857, p = 0.003). Also for the 2nd shape model parameter, which describes the neck shaft angle, there is a significant association (OR = 1.229, 95% CI 1.042 - 1.451, p = 0.014). The 10th and 11th mode of variation also have a strong and significant association but due to their relative small variance are difficult to interpret. The main mode of variation of the density model, which is related to the global density (Fig. 3), is strongly associated with the fracture incidence with an OR of 0.361 (95% CI 0.256 - 0.509) and is highly significant ($p < 0.001$). The AUC of this mode of variation (0.672, 95% CI 0.616 - 0.728) is comparable to the AUC of the various areal BMD measurements (Table 3.4). Again, the other modes of variation with a significant association (mode 6 and 10) are difficult to interpret due to their relative small variance.

In Fig. 3.7 the ROC curve is given for the parameters acquired by the model registration, the areal BMD values and the full set of model parameters and areal BMD measurements after a logistic regression analysis. The AUC for all evaluated combinations as well as the 95% CI and p values are presented in Table 3.5. The model parameters results in an AUC value of 0.752 (95% CI 0.701 - 0.803) whereas the areal BMD measurements results

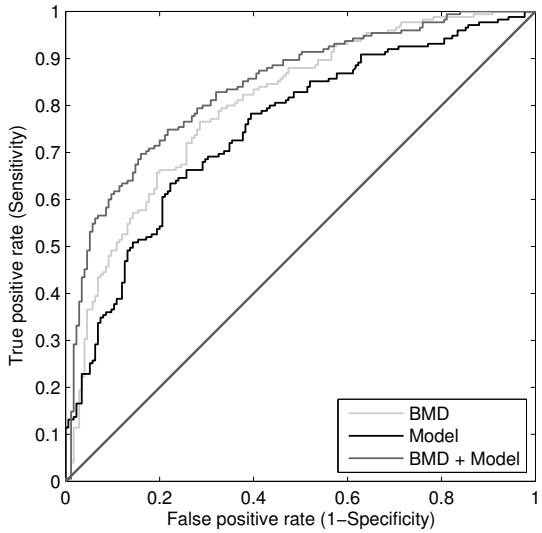

Figure 3.7: The ROC curves resulting from logistic regression analysis on the aBMD measurements (BMD), the shape and density model parameters (Model) and the combined areal BMD measurements and model parameters (BMD + Model).

in an AUC value of 0.802 (95% CI 0.757 - 0.848). By combining all model parameters and BMD measurements an AUC value of 0.840 (95% CI 0.799 - 0.881) is achieved.

Finally, Fig. 3.8 shows the reconstruction results corresponding to the subjects in the fracture and control group with respectively the highest and lowest fracture risk according to the logistic regression on the combined model parameters and areal BMD measurements. The reconstruction results are presented as a projection and the coronal and femoral neck cross-sectional slice of the deformed density model and the resulting mesh of the shape model instance.

3.4 Discussion

In this work a method to construct and register a statistical model of shape and density distribution onto a DXA image was presented and evaluated for its ability to discriminate between a fracture and control group. The model parameters resulting from the reconstructions have been shown to be able to improve the discrimination ability with respect to only DXA derived areal BMD measurements. Fig. 3.8 illustrates the differences in shape and density distribution that determine the fracture risk according to a logistic regression using the model parameters together with the areal BMD measurements. On the coronal slice it can be clearly seen that the high fracture risk has a decreased global volumetric BMD and an overall decreased cortical

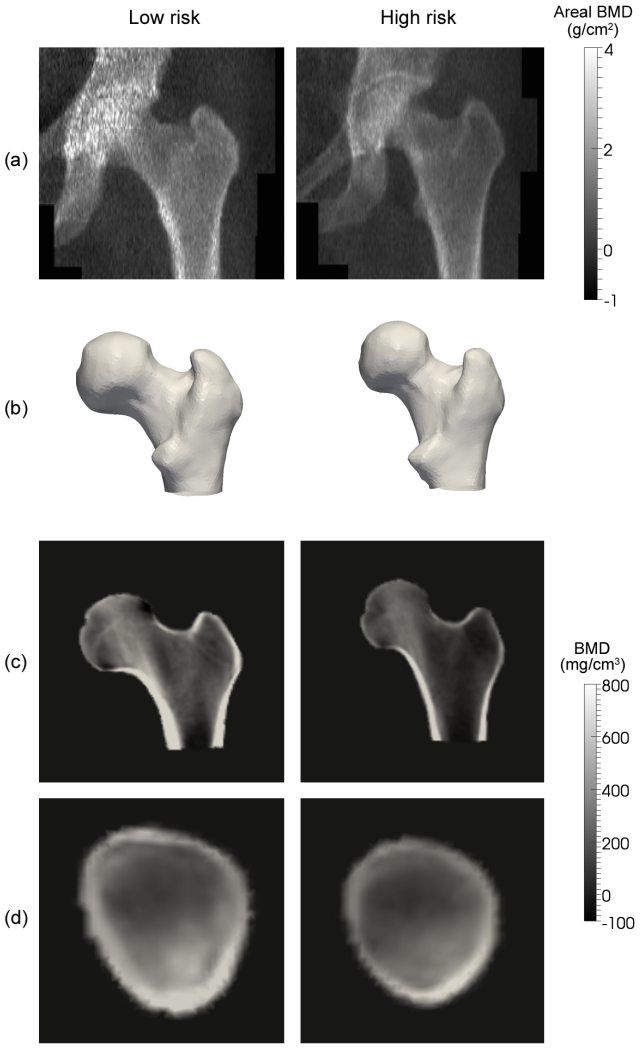

Figure 3.8: Reconstruction results of the subjects in the fracture and control group corresponding respectively to the highest and lowest fracture risk as determined by the logistic regression on the combined model parameters and areal BMD measurements. From top to bottom: the DXA images, the shape model instances, the coronal slices and the cross-sections of the femoral neck of the resulting density volumes.

thickness. This is in accordance with recent analysis on QCT measurements [12][58]. Also a greater cross-sectional area can be seen on the femoral neck cross-section, which again is supported by recent studies [9][58]. Regarding the shape, a greater neck-shaft angle can be seen on the high fracture risk subject, which corresponds to recent studies on hip structural analysis from DXA [62]. In this study the model parameters alone do not result in a better discrimination than areal BMD measurements. In several studies, also QCT measurements have not shown to significantly improve the discrimination ability over areal BMD measurements [20][9]. In [12], three combinations of QCT measurements were compared with areal BMD measurements using logistic regression analyses. Using trabecular BMD and the cortical thickness in the trochanteric region for the hip fracture discrimination resulted in an AUC of 0.843 (95% CI 0.764-0.922) as opposed to an AUC of 0.829 (95% CI 0.743-0.914) for the areal BMD values. However, combining the QCT measurements with the areal BMD measurements resulted in an AUC of 0.864 (95% CI 0.791-0.937). Our method results in a similar improvement with an AUC of 0.840 (95% CI 0.799-0.881) using the model parameters combined with the areal BMD measurements as opposed to an AUC of 0.802 (95% CI 0.757-0.848) using only the areal BMD measurements. Our method, however, only relies on the DXA imaging modality. Consequently, the patient does not have to be exposed to additional radiation. Moreover, the method is fully compatible with current clinical routine where DXA is the standard modality for fracture risk assessment.

The DXA scans used in this study were performed using the GE Lunar Prodigy bone densitometer which provides images with a resolution of $0.6 \times 1.05mm^2$ whereas the more recent line of DXA scanner result in significantly higher resolution images with a resolution of $0.3 \times 0.25mm^2$ for the newer GE Lunar iDXA device. Higher resolution images allow for more accurate reconstructions and thus a more accurate description of the 3D shape and the internal bone structure. Consequently, it is anticipated that the results obtained with the current dataset can be improved upon with the use of the more modern DXA devices. Furthermore, DXA devices equipped with a C-arm are appearing and the increased accuracy resulting from a multi-view reconstruction as presented in [2] is also expected to increase the hip fracture discrimination ability.

One limitation of this study is the retrospective analysis using the femur contralateral from the fractured femur. This can be justified by research on proximal femoral symmetry [32], but ideally an evaluation of the method should be performed on data resulting from a prospective study. In addition, no information about the fracture location was available for the DXA scans used in this work. The different types of fractures have been shown to relate to different parameters [44]. Thus, it is expected that performing site specific fracture risk estimations, e.g. making a distinction between femoral neck and intertrochanteric fractures, improves the fracture risk accuracy for the individual locations. In future work we hope to acquire a dataset that allows for the evaluation of a location specific fracture risk assessment and be able to evaluate the proposed method within a prospective study.

The method proposed in this work can, in a straightforward manner, be applied to other bones such as the vertebrae, which is the most common location for osteoporotic fractures. We therefore also aim to evaluate the proposed method for its ability to improve vertebral fracture risk estimations.

In conclusion, we have presented a method for improving the hip fracture discrimination ability from DXA by including the statistical model parameter values resulting from a 3D reconstruction with the regular areal BMD measurements. A 3D reconstruction method from DXA is combined with a statistical analysis of the 3D shape and BMD distribution to incorporate the advantages of a detailed 3D analysis as can be obtained from QCT, without exposing the patient to the associated high radiation dose. The results indicate that the proposed method can potentially improve the fracture risk estimation accuracy over current clinical practice while maintaining DXA as the standard modality.

4

3D Reconstruction of the Lumbar Vertebrae from Anteroposterior and Lateral Dual-energy X-ray Absorptiometry

Continuing the work presented in chapter 2, here both the 3D shape and volumetric density image of the lumbar vertebrae are reconstructed from DXA. This requires the extension of the reconstruction method to a multi-object approach to deal with the superimposition of the vertebrae on the radiographs. Besides the regular anterior-posterior (AP) view, the lumbar vertebrae allow for a lateral DXA image acquisition. Thus, the method is extended to a multi-view reconstruction. The reconstruction method is evaluated for the L2, L3 and L4 lumbar vertebrae. A statistical model of the shape and bone mineral density distribution is first constructed for each of the three vertebrae from a dataset of 66 QCT scans. All three models are then simultaneously registered onto both AP and lateral DXA image using an intensity based registration process. By using this multi-object approach, overlapping regions between consecutive vertebrae can be accurately reconstructed. Moreover, the addition of a lateral projection, which is not possible for the proximal femur, allows for an improved overall reconstruction accuracy. The reconstructions of 30 subjects are subsequently evaluated with respect to the ground truth QCT scans. For the shape, the point to surface distances are computed as well as the correlations of the mid vertebral body cross-sectional area (CSA) measurements. For the density distribution, the vBMD of the total vertebra, the vertebral body and the trabecular region inside of the vertebral body is compared with the same subject QCT scans.

The content of this chapter is adapted from the following publication:

T. Whitmarsh, L. Humbert, L. M. Del Rio Barquero, S. Di Gregorio, A. F. Frangi, 3D Reconstruction of the Lumbar Vertebrae from Anteroposterior and Lateral Dual-energy X-ray Absorptiometry, submitted, 2012.

4.1 Introduction

Approximately 25 percent of all postmenopausal women in the United States experience a vertebral compression fracture [82], which is the most common type of osteoporotic fracture. The fracture incidence increases with age due to the progression of osteoporosis, which is characterized by the deterioration of the bone tissue resulting in a more fragile bone. Although vertebral fractures can remain undiagnosed, they can potentially result in great discomfort and a diminished quality of life, and women with a vertebral fracture have a 15 percent higher mortality rate compared to those without [24].

Clinical measures for fracture prevention quantify the areal BMD of the vertebrae from DXA to determine the level of bone degradation. DXA provides an estimate of the projected density (g/cm^2) which does not take into account the thickness of the bone. This causes the BMD to be underestimated in individuals with smaller bones. Furthermore, in the AP DXA images, the vertebrae are superimposed by the spinous processes.

The vBMD extracted from QCT has been shown to be able to reliably evaluate levels of osteoporosis [40]. However, because of the high cost and high radiation dose, QCT is not used for such analysis in clinical routine.

Several methods to estimate the volumetric BMD from AP or lateral DXA have been proposed by assuming a cylindrical shape [17, 13, 60, 99]. This so called Bone Mineral Apparent Density (BMAD) has been shown to correlate well with the true volumetric density but does not describe the bone spatial distribution and is not able to discriminate between the trabecular and cortical components.

During aging and in particular when affected by osteoporosis, the trabecular bone structure within the vertebral body undergoes a process of degradation. It is the vBMD within this trabecular region that has been shown to be a strong determinant of the vertebral strength [52, 88, 87] and is a reliable fracture risk predictor [16, 49].

While QCT can measure the trabecular and cortical BMD separately, BMAD can not. Furthermore, also the shape largely determines the vertebral strength and should be taken into account when evaluating the risk of fracture. In particular the size of a vertebra has been shown to be significantly smaller for fracture patients than controls [30] and the vertebral body CSA, has been found to be smaller in woman with fractures than for controls [42]. Again, these measurements can be taken from CT but are not used in standard clinical practice.

There is already some previous work in reconstructing the 3D shape from planar radiographs. Some reconstruct the 3D shape by deforming a generic or parametric model [86, 29, 73, 68, 55] which requires the annotation of several landmarks on the radiographs. Several other approaches use a 3D statistical model to reconstruct the shape from planar X-ray images [7, 120]. These methods use the bone contours on the planar images to register and reconstruct the 3D shape whereby the silhouette of the model is matched with the edges extracted from the radiographs. These methods, however, only reconstruct the 3D shape and do not consider the bone mineral densities

and the bone spatial distribution.

Thus, in this work we propose a method to reconstruct the 3D shape as well as the density volume of the vertebra from DXA images used in clinical routine. A statistical model of the shape and a model of the spatial distribution of the vertebral bones are first constructed from a large database of QCT scans. These models are registered onto an AP and lateral DXA image in an intensity based registration process which, after convergence, results in the 3D reconstructions. The reconstructions are evaluated by a comparison with the same subject QCT volumes, which are considered the ground truth. The reconstruction accuracy of the shape is determined by the point to surface distances as well as comparing the CSA of the reconstruction with the CSA acquired from the ground truth QCT scans. In addition, the total vBMD, the vBMD of the vertebral body and the trabecular vBMD is evaluated with respect to the ground truth QCT.

4.2 Materials and methods

4.2.1 Data

A dataset of 96 spinal CT scans was collected at the CETIR Medical Center (Barcelona, Spain) using the Philips Gemini GXL 16 system (Philips Healthcare, Best, The Netherlands). All subjects were female and scans were rejected in case of the presence of arthritis, abnormal bone growth or the detection of vertebral fractures. The CT scans had a pixel spacing ranging between 0.47 and $1.04mm$ and a slice thickness of $0.5mm$. The volumes were calibrated using the Mindways calibration phantom (Mindways Software Inc., Austin, TX, United States) and were subsequently converted to calcium hydroxyapatite (HA) density values corresponding to the European forearm phantom [97].

In addition to the CT scan, for 30 patients also an AP and lateral DXA image of the lumbar spine was acquired using the GE Healthcare's Lunar iDXA scanner (GE Healthcare, Madison, WI, USA). For the AP direction the patient was in a standard supine position while for the lateral DXA image acquisition the patient was repositioned to a lateral recumbent position. The AP DXA image has a resolution of $0.3 \times 0.25mm^2$ and the Lateral DXA image a resolution of $0.6 \times 0.25mm^2$. These DXA images were subsequently converted to correspond to standardized BMD [41] which is also related to the HA density values of the European forearm phantom.

For these 30 subject, with an average age of 55 ± 11 years, the DXA images were used for the validation of the reconstruction method whereby the reconstructions were compared with the vertebral shapes and the volumetric densities acquired from the same subject CT scans. The remaining 66 CT scans of which the subjects had an average age of 54 ± 11 years were used for the construction of the statistical models used in the reconstruction method.

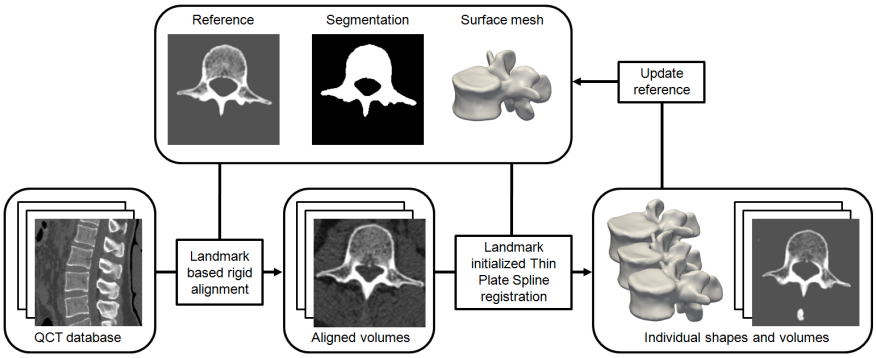

Figure 4.1: Model construction pipeline.

Ethical approval was granted for all data acquisitions by the Institutional Review Board and written informed consent was provided by all the subjects included in this study.

4.2.2 Statistical modelling

Shape model

In previous work a statistical model of shape and BMD distribution was presented for the proximal femur together with the method for its construction [108]. The statistical model of the vertebrae is of the same form. However, the more complicated shape requires a change to be made to the construction method in the form of an initialization using manually defined landmark locations.

The pipeline for the vertebral model construction is depicted in Fig. 4.1. First a reference is selected based on its regular bone shape. This reference is subsequently segmented using ITK-SNAP [117] to acquire a detailed triangular surface mesh. The mesh used in this work consisted of 28,586 vertices. All QCT scans are first registered onto this reference by a rigid transformation defined by 24 landmark locations (Fig. 4.2) which were identified in the volumes by a graphical user interface. The rigid transformation is computed according to [54], which gives the optimal mapping of the landmarks in a least squares sense. This is followed by an intensity based TPS registration using a subset of 300 vertices from the reference mesh as the control points, which were acquired using a mesh decimation method [53]. Here, the 24 manually defined landmarks define a TPS transformation which is used to initialize the TPS registration process. The transformations resulting from the registration process are used to deform the detailed reference mesh to the patient specific vertebral shapes of all QCT volumes.

For the intensity based TPS registrations the L-BFGS-B optimizer [122] was used in conjunction with Mattes Mutual Information similarity metric [80]. The similarity measure was extended by a regularization term based on a spring system as described in [110] to prevent the control points from

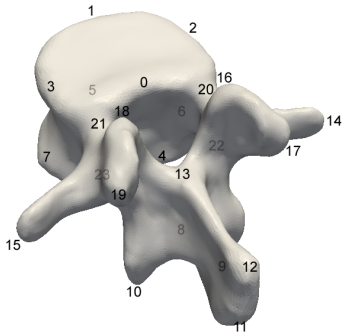

Figure 4.2: The 24 vertebral landmarks used to initialize the intensity based registrations in the model construction process.

drifting and to maintain a smooth regular mesh.

To remove the reference selection bias and to improve the individual registrations, the reference is deformed to the mean shape and the registration process is performed once more. This results in the aligned patient specific surface meshes with a vertex correspondence between them.

To generate the statistical model of the shape, PCA is applied to the vertices of the resulting surface meshes. Each i-th shape can be expressed by the set of vertex coordinates $\mathbf{s}_i = (\mathbf{x}_1^i, ..., \mathbf{x}_a^i)^T \in \mathbb{R}^{3a}$, where a is the number of vertices. The mean $\overline{\mathbf{s}} = (\overline{\mathbf{x}}_1, ..., \overline{\mathbf{x}}_a)^T$ is subsequently computed and the covariance matrix C_s can thus be expressed as:

$$C_s = \frac{1}{k-1} \sum_{i=1}^{k} (\mathbf{s}_i - \overline{\mathbf{s}})(\mathbf{s}_i - \overline{\mathbf{s}})^T \tag{4.1}$$

Here k is the number of subjects included in the analysis. Singular Value Decomposition (SVD) applied to this matrix retrieves the eigenvectors sorted by their associated eigenvalues. A new shape instance $\mathbf{s}$ can now be expressed as the mean shape and a linear combination of the first m eigenvectors corresponding to the main modes of variation:

$$\mathbf{s} = (\mathbf{x}_1, ..., \mathbf{x}_a)^T = \overline{\mathbf{s}} + \sum_{j=1}^{m} \mathbf{p}_j \alpha_j. \tag{4.2}$$

Here $\mathbf{p}_j$ is the j-th eigenvector and α_j the corresponding scalar coefficient, referred to here as the shape model parameter.

Density model

For generating the density model, the registration process is performed one more time which deforms each QCT volume to the mean shape, whereby the reference space is defined by $0.5mm$ cubic voxels. This results in the shape normalized volumes with a voxel correspondence between them, and PCA is

subsequently applied to the density values of the voxels inside of the bone shape. For each i-th volume the density values of the voxels are captured by vector $\mathbf{v}_i = (d_1^i, d_2^i, ..., d_b^i)^T \in \mathbb{R}^b$, where b is the number of voxels, and the average $\overline{\mathbf{v}}$ is computed as well as the covariance matrix C_v:

$$C_v = \frac{1}{k-1} \sum_{i=1}^{k} (\mathbf{v}_i - \overline{\mathbf{v}})(\mathbf{v}_i - \overline{\mathbf{v}})^T \tag{4.3}$$

Again SVD decomposes the covariance matrix into the eigenvectors and corresponding eigenvalues. A new volume $\mathbf{v}$ can now be expressed as the average volume $\overline{\mathbf{v}}$ and the first n eigenvectors which describes the changes in the density distribution:

$$\mathbf{v} = \overline{\mathbf{v}} + \sum_{j=1}^{n} \mathbf{q}_j \beta_j \tag{4.4}$$

Here $\mathbf{q}_j$ is the j-th eigenvector with the corresponding density model parameter β_j. A new instance of the density model thus describes the spatial distribution of the bone within the mean shape.

In this way a statistical model of shape and density distribution is generated for the L2, L3 and L4 vertebrae using the dataset of 66 QCT volumes previously described. Cattell's scree test [18] was used to determined the number of modes of variation that should be used in the statistical models, resulting in $m = 10$ shape model parameters and $n = 5$ density model parameters Figure 4.3.

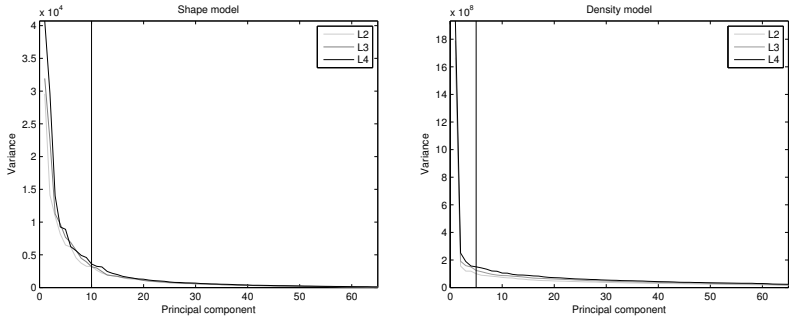

Figure 4.3: Scree plots of the shape models (left) and the density models (right) of the L2, L3 and L4 vertebrae. The "elbow" is determined to be at respectively the $10th$ and $5th$ principal component whereby, according to Cattell's scree test, all further components are dropped.

In Figure 4.4 the first three modes of variation of the shape and density model of the L3 vertebra are depicted. The statistical models of the L2 and L4 vertebrae show similar variations.

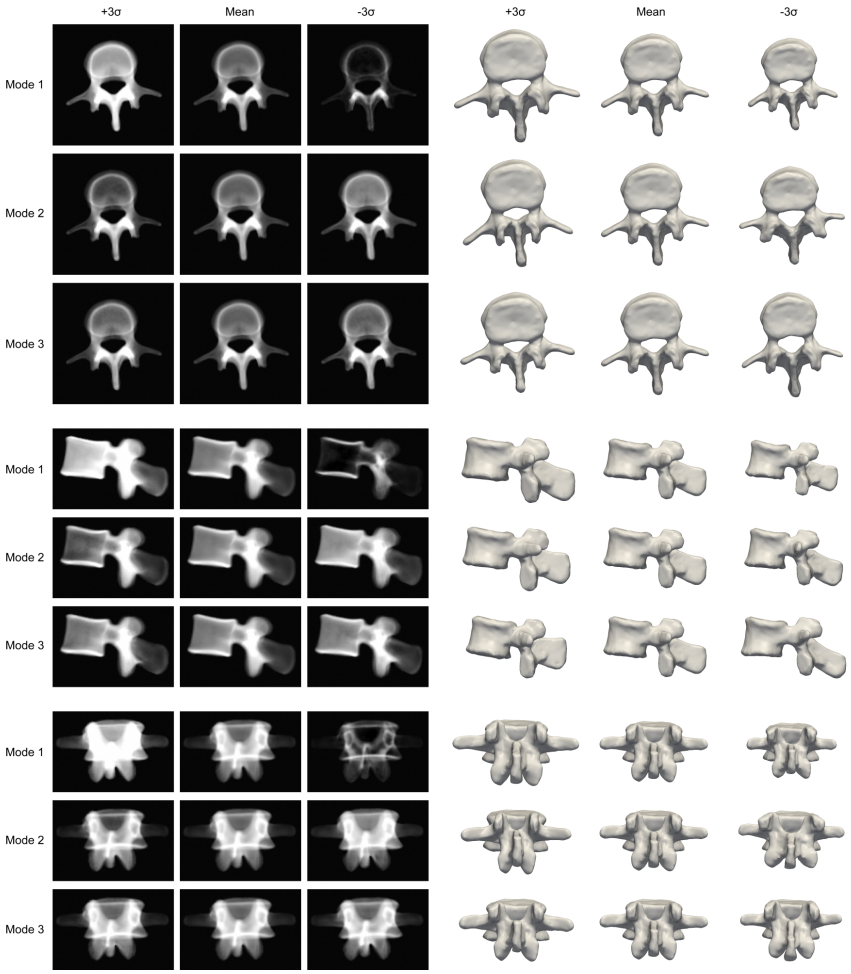

Figure 4.4: The mean and the first three modes of variation (described by +3 and -3 standard deviations (σ) from the mean) of the shape model (right) and projections of the density model (left) in the longitudinal (top), lateral (middle) and AP (bottom) direction.

Model instance

A new instance of the statistical model is defined by the shape and density model parameters. The density model parameters β_j define a new density model instance $\mathbf{v}$ and the shape model parameters α_j define the new shape onto which the volume is deformed. The densities of the density model instance are first implicitly rearranged to form a volume V:

$$\mathbf{v} \mapsto V \tag{4.5}$$

The density volume is defined in the space of the mean shape $\overline{\mathbf{s}}$ and is deformed to the new shape model instance $\mathbf{s}$ using a subset S of the vertex correspondences:

$$S \subset \{(\overline{\mathbf{x}}_1, \mathbf{x}_1), ..., (\overline{\mathbf{x}}_a, \mathbf{x}_a)\} \tag{4.6}$$

In this work a subset of 300 vertex pairs are used. From set S a TPS transformation T is defined which maps the vertices of the new shape (source vertices) to the corresponding vertices of the mean shape (target vertices):

$$\mathbf{x}_{\text{target}} = T(\mathbf{x}_{\text{source}}) \quad \forall\, (\mathbf{x}_{\text{target}}, \mathbf{x}_{\text{source}}) \in S \tag{4.7}$$

The TPS transformation is subsequently applied to the volume of the density model instance V to acquire the shape deformed density model instance V':

$$V' = V \circ T \tag{4.8}$$

4.2.3 Reconstruction

Similar as presented in [110] the vertebrae are reconstructed from DXA in an intensity based 3D-2D registration process. A multi-object approach was used by incorporating the L2, L3 and L4 vertebra simultaneously to deal with the overlap between the consecutive vertebra. In the 3D-2D registration process the model parameters are searched to find the instance of the shape and density models so that the projections of the shape deformed density model instance, referred to here as the Digitally Reconstructed Radiographs (DRRs), matches the anteroposterior and lateral DXA image (Figure 4.5). In addition to the model parameters, also the rigid transformation for both views has to be found, which is defined by a rotation about all three axes and a translation parallel to the image plane. Separate rigid transformations are required for both views since the patient is repositioned for the lateral DXA acquisition, which changes the spinal position and intervertebral orientations.

The registration is initialized by a manual alignment of the mean vertebral shapes in both views. The parameter set is subsequently optimized using an evolutionary algorithm based on [104] in conjunction with the Mean

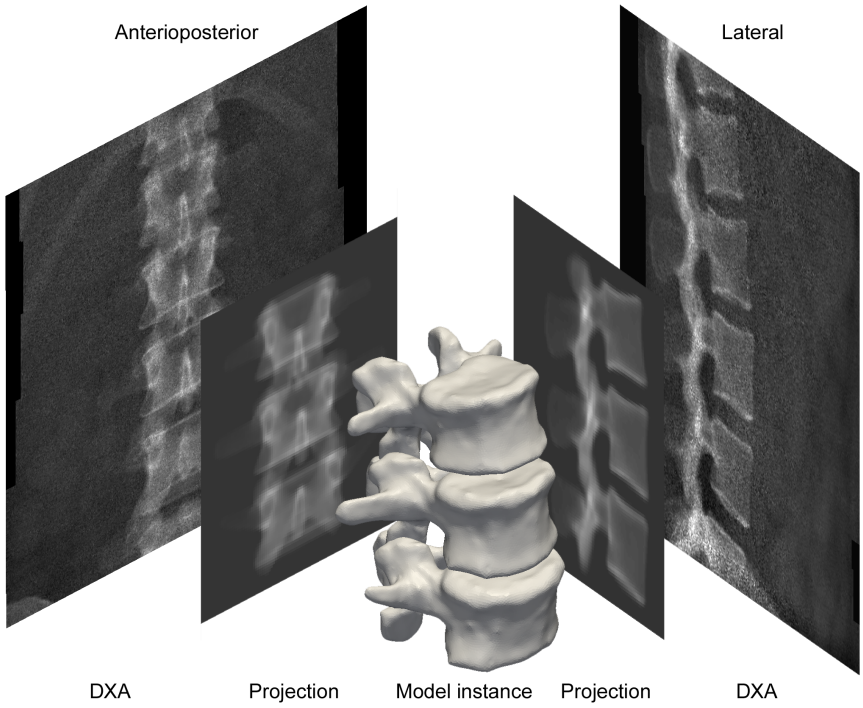

Figure 4.5: Illustration of the reconstruction process whereby the statistical model of the L2, L3 and L4 vertebra are registered onto the AP and lateral DXA images. The instance of the models are found so that their projections match the DXA images.

Squared Error (MSE) similarity measure. The objective function can be described as follows:

$$\min(\mathrm{MSE}(I^{\mathrm{AP}}_{\mathrm{DXA}}, I^{\mathrm{AP}}_{\mathrm{DRR}}) + \mathrm{MSE}(I^{\mathrm{lateral}}_{\mathrm{DXA}}, I^{\mathrm{lateral}}_{\mathrm{DRR}})) \tag{4.9}$$

Here the MSE over the AP DXA image $I^{\mathrm{AP}}_{\mathrm{DXA}}$ and the DRR of the model instance in the AP direction $I^{\mathrm{AP}}_{\mathrm{DRR}}$ is summed with the MSE computed over the lateral DXA image $I^{\mathrm{Lateral}}_{\mathrm{DXA}}$ and the DRR in the lateral direction $I^{\mathrm{Lateral}}_{\mathrm{DRR}}$. The DRR is generated by applying an isometric projection P over the three vertebral model instances (V'_{L2}, V'_{L3} and V'_{L4}) whereby for each vertebra first a rigid transformation is applied for both the AP DRR (R^{AP}) and the lateral DRR (R^{Lateral}):

$$\begin{aligned} I^{\mathrm{AP}}_{\mathrm{DRR}} = P(V'_{\mathrm{L2}} \circ R^{\mathrm{AP}}_{\mathrm{L2}}) \\ + P(V'_{\mathrm{L3}} \circ R^{\mathrm{AP}}_{\mathrm{L3}}) \\ + P(V'_{\mathrm{L4}} \circ R^{\mathrm{AP}}_{\mathrm{L4}}) \end{aligned} \tag{4.10}$$

$$\begin{aligned} I^{\mathrm{lateral}}_{\mathrm{DRR}} = P(V'_{\mathrm{L2}} \circ R^{\mathrm{lateral}}_{\mathrm{L2}}) \\ + P(V'_{\mathrm{L3}} \circ R^{\mathrm{lateral}}_{\mathrm{L3}}) \\ + P(V'_{\mathrm{L4}} \circ R^{\mathrm{lateral}}_{\mathrm{L4}}) \end{aligned} \tag{4.11}$$

A mask is manually defined on both the AP and lateral DXA images to constrain the registration process to the region of interest. In the lateral projection of the lumbar spine, the L4 vertebra is often overlapped by the pelvic bone [59]. To prevent the pelvic area from influencing the reconstructions, this overlapping region is removed from the mask and thus does not contribute to the similarity measure in the reconstruction process (Figure 4.6). By using an approach using a statistical model, however, still a statistically probable vertebral shape and density distribution is estimated in the region outside of the mask.

4.2.4 Evaluation

A statistical model was constructed of the L2, L3 and L4 vertebra using the dataset of 66 QCT scans. For the evaluation of the reconstruction accuracy, the dataset of 30 vertebral QCT scans with corresponding DXA images was used. The L2, L3 and L4 vertebral models were registered onto the AP and lateral DXA images simultaneously, resulting in the reconstructed vertebral shape and the density volume for all three vertebrae. The reconstruction accuracy of the shapes and the volumetric densities were evaluated by a comparison with the same subject QCT scans. For this evaluation, all QCT scans were manually segmented and a detailed surface mesh was constructed from the segmentations.

The reconstruction accuracy of the shape was evaluated by first aligning the reconstructed shape with the ground truth surface mesh using the iterative closest point algorithm. Subsequently, the point-to-surface distances

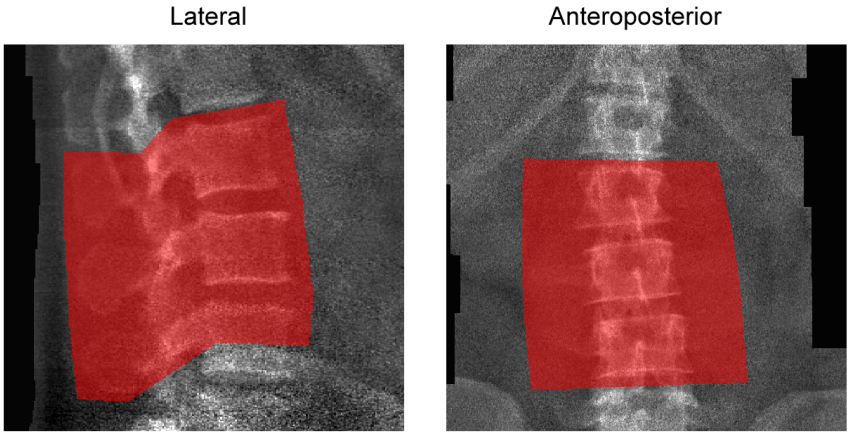

Figure 4.6: The regions of interest on the Lateral and AP DXA image used for constraining the reconstruction process.

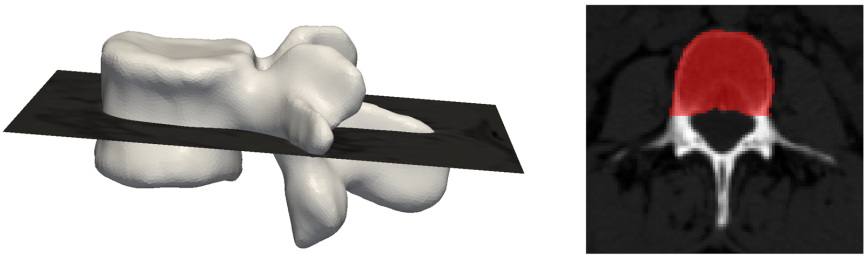

Figure 4.7: The location of the mid vertebral body cross-section (left) and the region for computing the CSA indicated in red (left).

from the vertices in the model to the surface mesh were computed. Since the vertebral body is the region of interest with respect to vertebral fractures, this region was identified on the vertebral shape, and the point-to-surface distances of this region were evaluated separately.

In addition to the point to surface distances, the reconstruction accuracy of the more clinically relevant CSA was evaluated. The total CSA was defined in the mid vertebral body as depicted in Fig. 4.7. The manual segmentation subsequently defines the vertebral bone region and vertebral body is isolated by a line parallel to the transverse processes. This region was extracted in both the reconstructed volumes and the ground truth QCT volumes which were subsequently compared to each other by a linear regression analysis.

The ability of the method to reconstruct the volumetric densities was evaluated by comparing the total vBMD, the vertebral body vBMD and the trabecular vBMD extracted from the reconstructions with respect to the same measurements from the ground truth QCT volumes. The corre-

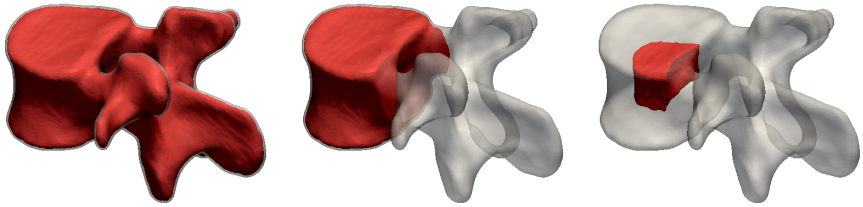

Figure 4.8: From left to right: the total vertebra, the vertebral body and the trabecular region within the vertebra for the vBMD measurements.

Table 4.1: The shape errors expressed as point-to-surface distances (mm).

	Total			Vertebral body		
	Mean	2RMS*	Max	Mean	2RMS*	Max
L2	1.02	2.77	9.68	0.81	2.06	6.45
L3	1.01	2.74	12.57	0.79	2.16	6.67
L4	1.30	3.55	12.13	1.05	2.81	7.15

* 95% confidence interval.

sponding regions are illustrated in Fig. 4.8. The total vBMD is acquired by computing the average density in the whole vertebra. The vertebral body vBMD is determined by considering only the densities in the vertebral body which include the cortical bone. Finally, the region for the trabecular vBMD is determined by dilating the region of the vertebral body by $6mm$ to guarantee the exclusion of the cortical component.

4.3 Results

All reconstructions converged in approximately 10,000 iterations and the full set of 30 reconstructions took approximately 130 hours to complete on an Intel®Core™ i7 CPU 920 @ 2.67GHz processor.

The shape of the L2 vertebra was reconstructed with a mean(2RMS) point-to-surface distance of $1.02(2.77)mm$ for the total vertebral shape and $0.81(2.06)mm$ for the vertebral body. The L3 vertebrae were reconstructed with a similar accuracy of $1.01(2.74)mm$ and $0.79(2.16)mm$ for the total vertebral shape and the vertebral body respectively. The reconstruction accuracy of the shape of the L4 vertebrae was slightly lower with a mean(2RMS) point-to-surface distance of $1.30(3.55)mm$ for the total vertebral shape and $1.05(2.81)mm$ for the vertebral body. The full set of measurements are presented in Table 4.1. In Fig. 4.9 the average point to surface distances are visualized on the mean shapes which show the distribution of the shape errors.

In Fig. 4.10 the boxplots of the vBMD and CSA reconstruction errors are given. The full set of vBMD and CSA reconstruction errors and correlation values are given in Table 4.2. All reported correlations are statistically

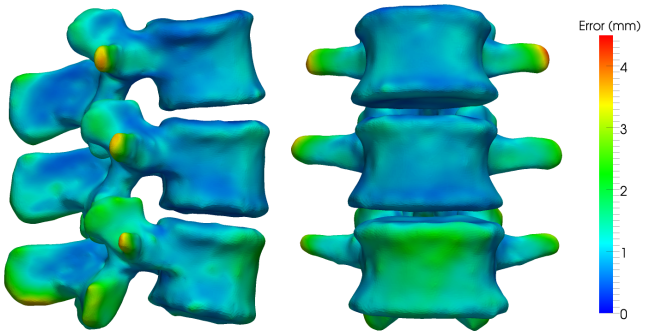

Figure 4.9: The color-coded point to surface distances (mm) between the reconstructed shapes and the QCT-derived surfaces averaged over the 30 subjects.

significant ($p < 0.05$).

For the vBMD measurements of the L2 and L3 vertebrae a strong correlation ($r > 0.85$) was found with the QCT measurements. In particular the trabecular vBMD was reconstructed with a mean(2RMS) error of $22.3(52.9)mg/cm^3$ and $19.1(46.3)mg/cm^3$ and a correlation coefficient of 0.90 and 0.85 for the L2 and L3 vertebrae respectively. Again the L4 vertebra showed a slightly less accurate reconstruction with a correlation coefficient of 0.81 and 0.82 for the vertebral body and trabecular region respectively. In Fig. 4.11 the linear regressions are shown for all vBMD measurements.

Figure 4.12 shows the mid vertebral body slices of the reconstructed L3 vertebra and of the corresponding QCT scans of 3 subjects. The boxplots of the CSA reconstruction accuracies show several outliers which have a significant negative effect on the regression analysis, as can be seen in the offsets and slopes associated with the regressions. Performing the regression analysis with the outliers removed resulted in a correlation coefficient of 0.83, 0.75 and 0.55 for the L2, L3 and L4 vertebrae respectively. The scatter plots and regression lines, both using all 30 subjects and with the outliers removed, are given in Fig. 4.13.

4.4 Discussion

Both the vBMD measurements from QCT and the estimates of volumetric BMD (BMAD) have been shown to be stronger associated with vertebral fractures than standard projected BMD measurements [60]. Thus, taking into account the 3D shape and thereby the volume of the vertebrae can improve the measurement of the bone density and consequently provide a better fracture risk estimation. In [55] the 3D shape of the vertebrae were reconstructed from biplanar X-rays images with a mean(2RMS) point-to-surface distance of $1.0(2.7)mm$. In comparison, our method reconstructed the global region of the L2 and L3 lumbar vertebra with a similar mean(2RMS) point-to-surface distance of $1.02(2.77)mm$ and $1.01(2.74)mm$ respectively.

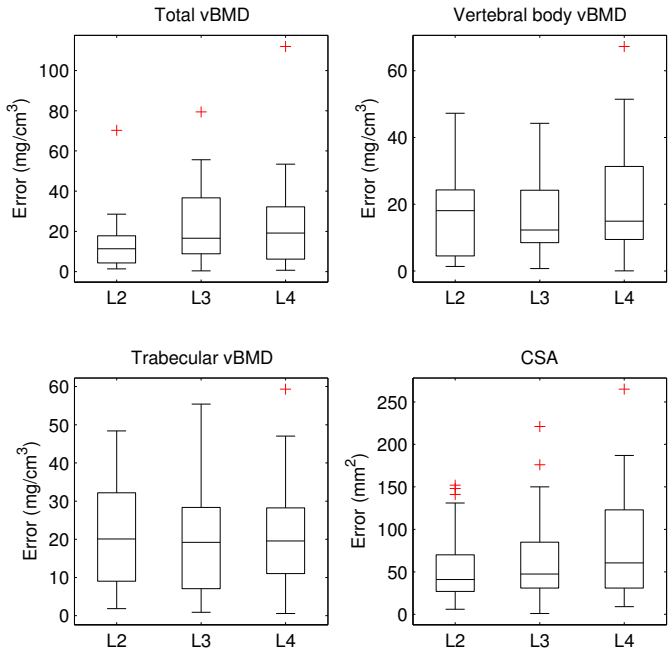

Figure 4.10: The boxplots of the vBMD and CSA reconstruction errors with the outliers indicated by crosses.

Table 4.2: The reconstruction errors and correlation values for the vBMD and CSA measurements (with outliers removed in Italic).

		Mean	2RMS*	Max	r	Offset	Slope
L2	vBMD total (mg/cm^3)	13.9	38.1	70.3	0.92	-1.5	1.03
	vBMD body (mg/cm^3)	16.8	41.5	47.3	0.89	-15.0	1.02
	vBMD trab. (mg/cm^3)	22.3	52.9	48.4	0.90	-12.9	0.94
	CSA (mm^2)	54.3	135.5	152	0.74	226.2	0.80
		44.0	*103.8*	*131*	*0.83*	*98.8*	*0.92*
L3	vBMD total (mg/cm^3)	21.5	56.1	79.4	0.91	-20.7	1.17
	vBMD body (mg/cm^3)	16.5	40.9	44.2	0.87	-26.6	1.17
	vBMD trab. (mg/cm^3)	19.1	46.3	55.4	0.85	-12.2	1.05
	CSA (mm^2)	62.8	160.9	221	0.71	440.8	0.61
		53.1	*127.8*	*150*	*0.75*	*199.0*	*0.83*
L4	vBMD total (mg/cm^3)	22.9	63.9	112.0	0.86	-10.14	1.12
	vBMD body (mg/cm^3)	21.1	54.3	67.2	0.81	-8.46	1.08
	vBMD trab. (mg/cm^3)	21.1	50.2	59.3	0.82	-0.37	0.98
	CSA (mm^2)	79.3	201.1	265	0.45	457.0	0.58
		72.9	*179.2*	*187*	*0.55*	*300.4*	*0.72*

The vBMD and CSA error expressed as absolute differences.
* 95% confidence interval.

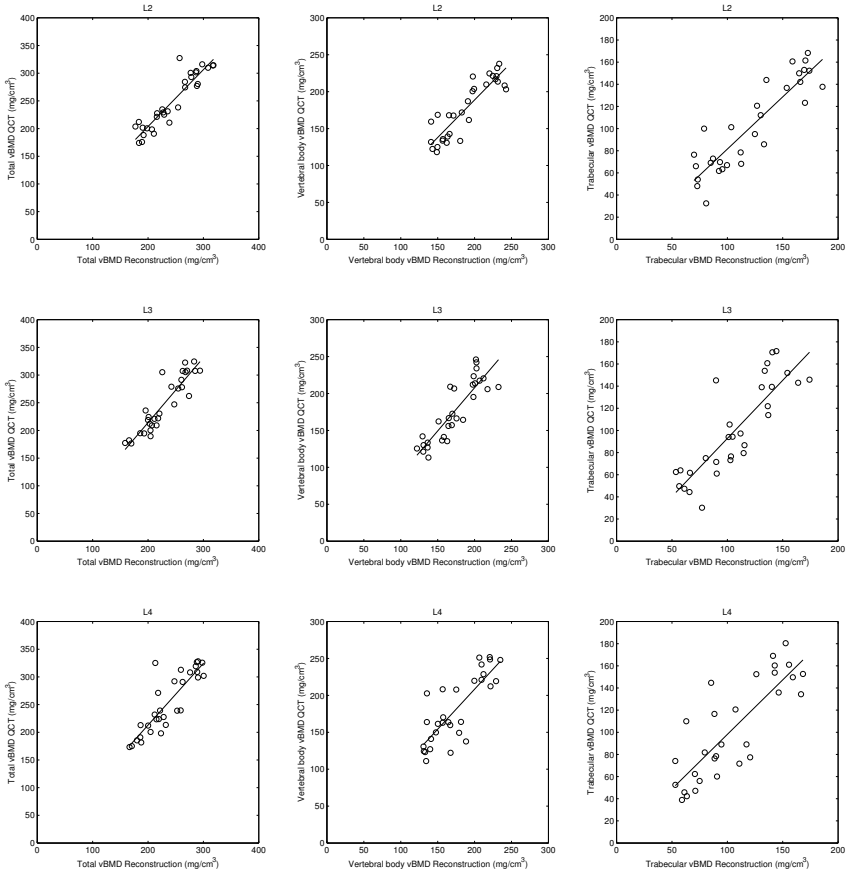

Figure 4.11: Linear regressions between the vBMD measurements extracted from the reconstructions and the ground truth QCT volumes.

In Fig. 4.9 one can see that the point-to-surface distances are disproportionately large at the transverse processes. These segments, of which the low density bone contours are difficult to distinguish from the soft tissue structures on the DXA images, contribute a great deal to the global shape error. This anatomical region, however, is of little importance with respect to the diagnostic of pathologies on the vertebral column.

While accurately reconstructing the 3D shape can potentially improve the estimation of the total volumetric density, our method is able to also reconstruction the volumetric densities inside of the bone, and thus is able to estimate the trabecular vBMD. The trabecular vBMD measurements from QCT have previously been shown to provide a better measure for the risk of fracture than aBMD measurements from DXA. In [49] a comparison between the fracture discrimination ability of QCT derived trabecular vBMD and regular areal BMD measurements from lateral and AP DXA resulted in an Area Under the Receiver Operating Curve (AUROC) of 0.9518 ± 0.0228 for

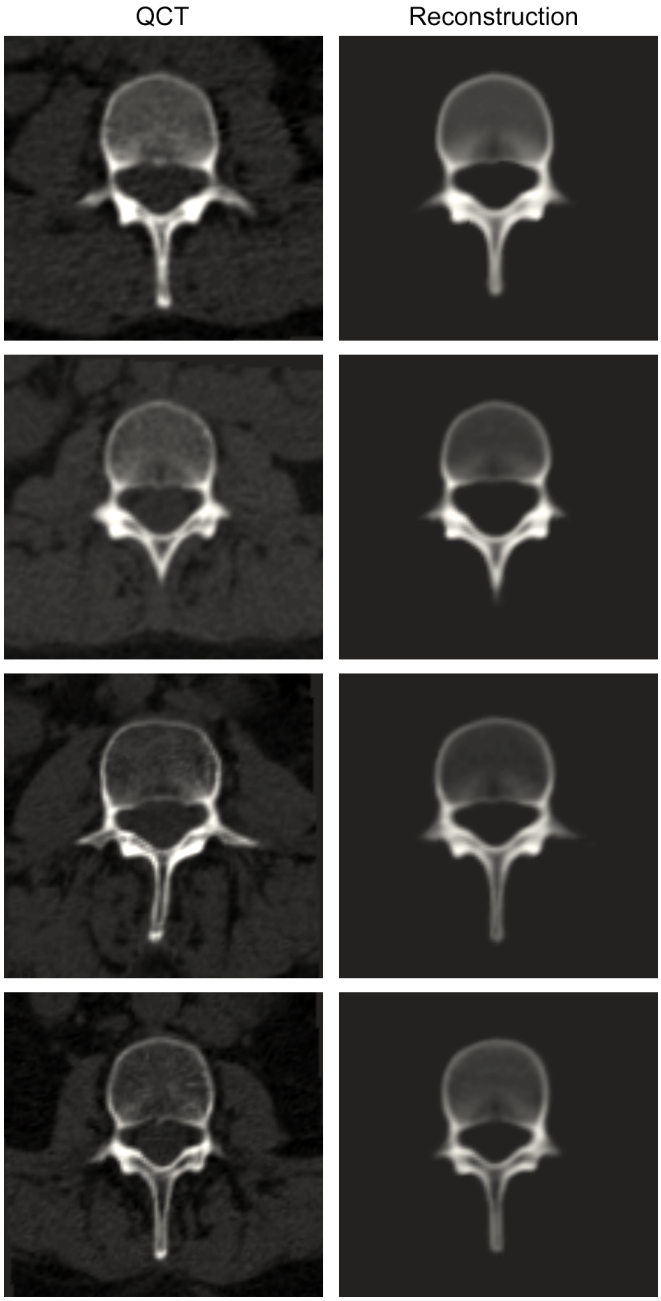

Figure 4.12: The L3 mid vertebral body slices from QCT (left) and the reconstructions from the DXA images of the same subjects (right).

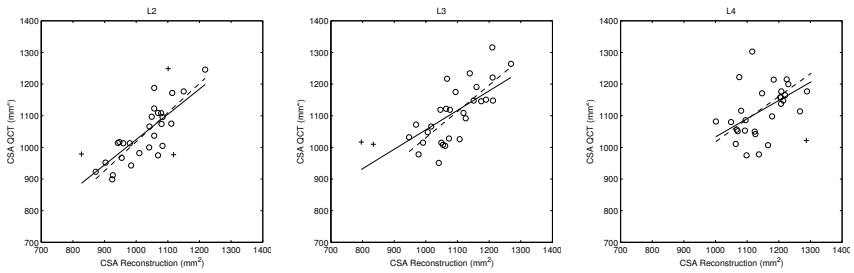

Figure 4.13: Linear regressions between the CSA measurements from the reconstructions and the ground truth QCT volumes. The outliers are indicated by the crosses and the dashed line represents the regression line when the outliers were removed.

QCT, and an AUROC of 0.8741 ± 0.0332 and 0.7931 ± 0.0446 for the lateral and AP DXA respectively.

In this study a strong correlation was found between the reconstructed trabecular vBMD and the trabecular vBMD extracted from QCT with a correlation coefficient of 0.90 and 0.85 for the L2 and L3 vertebra respectively. Considering it is the trabecular region that is predominantly affected by osteoporosis and is recognized as the main cause of compression fractures, this indicates the potential of the method to improve the fracture risk estimation accuracy from DXA. Furthermore, the method is able to accurately reconstruct the shape with respect to the vertebral body CSA ($r > 0.74$ and $r > 0.71$ for the L2 and L3 vertebrae respectively), which is a structural measurement related to the vertebral body compressive strength. The boxplots and regression values, however, indicate several outliers which remain undetected in the vBMD measurements (Fig. 4.10). Thus, additional efforts are required to make the method more robust with respect to the shape reconstruction.

The L4 vertebra is reconstructed with the least amount of accuracy. For the shape a mean(2RMS) point-to-surface distance of $1.30(3.55)mm$ was measured for the total vertebral shape and $1.05(2.81)mm$ for the vertebral body and a correlation coefficient of 0.45 was found for the evaluation of the CSA. This can be explained by the fact that, for many subjects, on the lateral DXA image a large part of the L4 vertebra was not taken into account in the registration process due to the overlap with the pelvic bone. The decrease in accuracy, however, is relatively low, which shows the ability of the statistical model to reconstruct anatomical regions from partial information.

Although there might be some overlapping rib structures for the L2 and L3 vertebrae, these vertebrae can more consistently be reconstructed. Moreover, the reconstruction accuracy of the L2 vertebrae is expected to improve further by including the L1 vertebra in the reconstruction process, thereby also taking into account the overlapping regions with the L1 vertebra. The CT scans used in this work, however, did not include the L1 vertebrae and this structure could therefore not be modeled.

The computation time is currently not practical for the use in clinical

routine. However, many optimizations are possible such as GPU acceleration and distributed parallel computing.

The proposed method does not administer the patient to a high radiation dose as QCT does and, by using standard DXA imaging devices, is fully compliant with clinical practice in osteoporosis diagnosis and fracture risk estimation. Furthermore, the accurate reconstruction of the shape can potentially aid in the detection of vertebral fractures or pathologies such as lumbar spinal stenosis.

4.5 Conclusions

In this work a method was presented to reconstruct the lumbar vertebra from an AP and lateral DXA image. A statistical model of the shape and BMD distribution of the L2, L3 and L4 vertebra was first constructed from a large dataset of QCT scans. The models were simultaneously registered onto the two DXA images by an intensity based 3D-2D registration process. The method is distinct from previous work by incorporating statistical information about the density distribution. Thereby, apart from the shape, also the spatial distribution of the bone is reconstructed. This allows us to extract the vBMD of the trabecular bone which has a better fracture prediction ability than regular areal BMD used in clinical routine. Thus, our method has the potential to improve the fracture risk estimation while maintaining the low cost and low radiation dose DXA images as the standard modality used in clinical routine.

5

Conclusions

5.1 Overview

Within this thesis a new approach to osteoporotic fracture risk assessment from DXA was explored by using a 3D reconstruction method. Working towards the goal of developing a improved fracture risk estimation method resulted in the following contributions:

• The development of a statistical model of the 3D shape and BMD distribution and a method for its construction from a large dataset of QCT scans for both the proximal femur and the lumbar vertebrae.

• An intensity based 3D-2D registration method was developed to register the statistical model onto one or more DXA images resulting in a 3D reconstruction. This method was evaluated for both the proximal femur and the lumbar vertebrae.

• The model parameters resulting from the reconstruction of the proximal femur from DXA were evaluated for their hip fracture discrimination ability with respect to aBMD measurements and thereby for its potential to improve the estimation of the risk of fracture over current clinical practice.

5.2 Conclusions and discussion

Statistical shape and density model. This thesis introduces a novel statistical model of the 3D shape and density distribution of bone structures through the use of TPS transformations. Other authors have proposed similar statistical models of the bone shape and spatial distribution. In [114], Yao and Taylor present a statistical model described by a tetrahedral mesh with Bernstein polynomial density functions in the tetrahedrals. A similar tetraherdal model was proposed in [89] whereby density values were included in the tetraherdal mesh nodes. Fritscher *et al.* [37] developed a combined shape and density model where a statistical analysis was performed onto the intensities in the volumes and the displacement fields resulting from non-rigid registrations. The model presented in this thesis is distinct from these other statistical bone models in that the analysis of the density distribution is disconnected from the shape by using only control points on the bone surface for the deformations. Although both models can be combined into a single statistical model for the reconstruction process, as described in Chapter 2, an analysis can be performed on the density distribution separately. This can be of great importance for the diagnosis of osteoporosis which affects preliminary the internal bone structure or for assessing the pharmaceutical based bone regrowth. Likewise, the shape can be analyzed separately for implant design selection which requires an accurate subject specific shape.

The model construction method presented in this thesis has gone through several stages of development motivated by various design choices. Originally based on the work by Cootes *et al.* [26] and Frangi *et al.* [35] a statistical shape model was constructed by an intensity based registration process onto a segmented reference subject using first an affine registration which is followed by a multi-scale B-spline registration [109]. This shape model was

extended by modeling the density distribution after deforming all volumes to the mean shape using a TPS transformation, which follows the principals of the Active Appearance Model (AAM) originally proposed by Cootes *et al.* [25]. The registration process was later replaced by a similarity registration followed by a TPS registration and was iterated to remove the bias of the reference selection as proposed in [35]. The iterative process using the similarity transform removes the necessity of a Generalized Procrustes Analysis (GPA) for an alignment of the shapes, while the density model construction now only requires an extra iteration of the registration process. These changes make the model construction pipeline more streamlined while having less distinct components reduces cumulative errors.

Another design choice concerns the normalization of the shapes and density values. The true shape representation is often defined as the shape with the location, scale and rotation effects filtered out. The shape model presented in Chapter 2 is therefore constructed by iterative similarity based registrations which results in scale normalized aligned shapes. A subject specific reconstruction thus requires an extra scale parameter in addition to the model parameters. However, certain applications of statistical shape models benefit from adding the scale information into the statistical analysis. In Chapter 3 the subject specific shapes were rescaled to their original size before applying PCA. The resulting principal components as shown in Figure 3.3 are much more descriptive then the ones with the scale normalized. The first mode of variation describes the size, while the second and third clearly describe the neck-shaft angle and hip axis length. These variations are less apparent with the scale normalized as shown in Figure 2.4. A similar case can be made for not normalizing the internal bone mineral density values. Other authors apply PCA to the combined shape and density values [95][37] which requires them to be normalized. This removes the statistical relationship between the densities and shapes which is of particular importance when reconstructing the shape from a single DXA image. In Chapter 2 the shape and density model is combined into a single model by applying PCA over the eigenvector coefficients which maintains the true size and density variations. However, it has not been investigated whether the combined model outperforms the use of a separate shape and density model and consequently in Chapter 3 an approach was chosen to decouple the shape and density model.

3D Reconstruction from DXA. The statistical model was shown to be able to accurately reconstruct both the 3D shape and density volume from DXA by incorporating it in an intensity based registration process. Comparisons between the reconstructed femur and the ground truth QCT scans gave an average error of $1.1mm$ and a 2RMS error of $2.6mm$ for the global shape. Analyzing the BMD distribution reconstruction accuracy in the global region, a mean error of $72.0mg/cm^3$ corresponding to 4.9% of the range of bone densities in this region was measured with a 95% confidence interval of $217.2mg/cm^3$ corresponding to 14.8% of the total range of bone densities.

The reconstruction method was, in Chapter 4, also shown to results in

accurate and realistic reconstructions for the lumbar vertebrae from a AP and lateral DXA image. The vertebrae were reconstructed with a global average point to surface distance of $1.02mm$, $1.01mm$ and $1.30mm$ for the L2, L3 and L4 vertebrae respectively and strong correlations ($r > 0.81$) were found between the vBMD extracted from the reconstructions and the same subject QCT scans.

Although for the reconstruction of the vertebrae the same techniques were used as for the proximal femur, some design choices had to be made regarding the use of multiple models. Some previous work model the relative spacing of the vertebrae [7][10]. This approach, however, constrains the orientation of the individual vertebrae. Considering this thesis is aimed towards fracture risk assessment, the accuracy of the vertebral shape is considered to be more important than their relative orientations. Thus, it was decided to not model the vertebral articulation. In addition, the consecutive vertebral shapes and density distributions are expected to be highly correlated, which can be captured by combining them into a single statistical model. However, this would again constrain the shape and densities of the individual vertebrae which we therefore opted against. As a consequence, the parameter space became quite large, which in turn resulted in a large computation time, making the method currently not viable in clinical routine. Thus, a balance has to be found between the dimensionality on one side and the reconstruction accuracy on the other. This will ultimately be decided by time requirements in clinical practice usage and the reconstruction accuracy required for the fracture risk estimation.

Fracture risk assessment. Reconstructions of the proximal femur from DXA were, in Chapter 3, shown to be able to discriminate well between a fracture and control group. Although measurements can be taken from the reconstructed volumes, a novel technique was proposed by using the model parameters directly, which give a more complete representation of the subject specific shape and internal bone distribution. By using a logistic regression analysis, the model parameters were shown to improve the discrimination ability of aBMD measurements currently used in clinical routine. The AUC of the combined model parameters and areal BMD values was 0.840 (95% CI 0.799 - 0.881), while using only the areal BMD values resulted in an AUC of 0.802 (95% CI 0.757 - 0.848). Thus, the presented method potentially allows for improved hip fracture risk estimation while maintaining DXA as the current standard modality.

Although the evaluation was performed for the proximal femur only, the method can in a straightforward manner be applied to the vertebrae. The vertebral fracture discrimination ability, however, remains to be investigated. Nonetheless, the reconstruction accuracy of the trabecular vBMD ($r > 0.82$) as well as the cross-sectional area ($r > 0.71$ for the L2 and L3 vertebrae), which have been shown to be accurate fracture predictors, suggest that the reconstruction method does indeed allow for an accurate fracture risk estimation for the vertebrae as well.

5.3 Outlook and future work

The work carried out in this thesis constitutes a first step towards an improved fracture risk estimation technique. Although the results are promising, a lot more research and validation is required to produce a method which can be used in clinical practice and be deployed in clinics. In addition, this work can take many different directions and has other applications then only deriving a risk of fracture. Following are some proposed steps toward the main goal of this thesis as well as different lines of research based on this work.

Reconstructing from a C-arm DXA device. The experiments performed within this thesis used DXA images acquired by a narrow-angle fan-beam DXA device. This acquisition method has several advantages over other devices. For instance, there is no magnification effect related to the distance to the X-ray source and therefore no complicated camera calibration is required. On the other hand, these devices are capable of acquiring a single view DXA image only for the proximal femur and in order to acquire the lateral vertebral DXA scan, the patient has to be repositioned from the supine position. Some of the newer DXA systems are equipped with a rotation C-arm. These allow for the acquisition of several projections at various angles. Using projections at multiple angles potentially allows for a greatly increased reconstruction accuracy. The advantages have already been shown by evaluating the reconstruction accuracy from several angles using DXA images simulated from QCT [56]. Further development of the technique will be required for the reconstruction method to be applied to real C-arm DXA devices. Considering these devices are starting to be more widely deployed and provide clear advantages over single view DXA devices, effort are being put forth towards this goal.

Finite Element Modeling. In this thesis an approach to fracture risk estimation was chosen which fully relies on statistics. However, advancements in mechanical simulations on bones have recently received great interest. Finite element modeling allows for the simulation of a mechanical test and thus can assess the resistance of bones to specific forces [64][90]. In this way the effect of the forces associated with a single-limb stance or a fall, commonly the cause of an osteoporotic fracture, can be simulated. Although these simulations can be performed on QCT scans, they can as well be performed on the 3D reconstructions acquired by the method presented in this thesis. Some work towards this goal has already been published [107], but more work is required for this technique to be able to derive a personalized risk assessment. In future work we will attempt to perform the FEM analysis from the 3D reconstructions automatically, whereby a tetrahedral mesh is constructed from the reconstructed shape which is given material properties extracted from the reconstructed density volume. Some evaluations are already underway by comparing strains acquired from a FEM analysis on the reconstructions with measured strains under different loading conditions.

Statistical morphometric analysis. Several shape, density and structural parameters of the proximal femur and vertebrae can be extracted from DXA and QCT, which can be said to describe strength properties of the bone. However, there exist many conflicting reports in the literature in what way these parameters relate to the femoral strength and fracture incidence. For instance, a lesser femoral neck cross-sectional area is believed to be an indicator of a weaker bone and has been shown to be related to a higher fracture incidence [58]. Other work report the opposite [43] and link the enlargement of the CSA with the adaptation to lower BMD in these osteoporotic subjects [20].

This suggest that the complex bone structures and their relation to the bone strength is not yet well understood. The statistical model described in this thesis is particularly useful in examining the global shape changes as well as the BMD distribution variations of a population. Statistical analysis can determine the shape and density changes which determine the risk of fracture. This has, to some extend, already been investigated by us in [108]. In addition, the morphometry and densitometry parameters relate differently to the fracture risk depending on the type of fracture [31]. The proposed analysis is able to assess the morphological changes associated with the fracture risk for specific fracture types, which can lead to a more targeted risk assessment.

Thus, the statistical methods presented in this thesis have a wider application in basic research on bone morphometry which is important for deriving an accurate subject specific and location specific fracture risk assessment.

Vertebral fracture classification. The spine is subject to years of repetitive motion and large compressive forces and the vertebra are therefore at high risk of degenerative changes. Even though these degenerative changes are often asymptomatic, they can result in great pain and discomfort from nerve impingement. The detection of this abnormal bone morphometry, however, is often difficult. In addition, the shape changes associated with normal aging are still under debate. In particular, there is no consensus on whether a mild wedging of the vertebral body is the result of a continuous remodeling with the advancing age or due to micro fractures. To be able to diagnose osteoporotic vertebral fractures and other pathological morphological changes, these should be distinguishable from normality. The detection of vertebral fractures is of particular importance considering the detection of a previous fracture is associated with a four times greater risk of subsequent vertebral fractures [66] as well as an increased risk for hip fractures [8].

The vertebral shape is commonly analyzed by geometric measurements from planar radio graphs. Common measures for vertebral fracture detection are the anterior, middle and posterior heights of the vertebral body and the ratios between them [48]. More complete measurements and dimensions of various anatomical parts of the selected vertebrae can be acquired from CT [121][106] or MRI scans [102] which allow for three dimensional measurements. These measurements, however, are still limited descriptors of

the complex vertebral shape and the high radiation dose associated with CT and the limited access to MRI devices make this technique unsuitable for standard practice diagnostic in clinical routine. Some previous work already applies statistical shape models to the segmentation of the bone contours from x-ray images [96] and the analysis of the shapes with respect to vertebral fractures [28]. The detailed statistical analysis of the complex 3D shape, as presented in this thesis, together with the reconstruction method from DXA or regular X-ray images can potentially lead to an improved vertebral fracture classification and thereby an improved fracture risk assessment.

References

[1] FRAX WHO Fracture Risk Assessment Tool.

[2] O. Ahmad, K. Ramamurthi, K. E. Wilson, K. Engelke, R. L. Prince, and R. H. Taylor. Volumetric DXA (VXA): A new method to extract 3D information from multiple in vivo DXA images. *Journal of Bone and Mineral Research*, 25(12):2744–2751, 2010.

[3] N. Baka, W. Niessen, B. Kaptein, T. van Walsum, L. Ferrarini, J. Reiber, and B. Lelieveldt. Correspondence free 3D statistical shape model fitting to sparse x-ray projections. In *Proceedings of SPIE Medical Imaging 2010: Image Processing*, page 76230D, 2010.

[4] J. C. Baker-LePain, K. R. Luker, J. A. Lynch, N. Parimi, M. C. Nevitt, and N. E. Lane. Active shape modeling of the hip in the prediction of incident hip fracture. *Journal of Bone and Mineral Research*, 26(3):468–474, 2011.

[5] A. Baudoin, W. Skalli, J. de Guise, and D. Mitton. Parametric subject-specific model for in vivo 3D reconstruction using bi-planar X-rays: application to the upper femoral extremity. *Medical and Biological Engineering and Computing*, 46(8):799–805, August 2008.

[6] T. J. Beck, C. B. Ruff, K. E. Warden, W. W. Scott, and G. U. Rao. Predicting femoral neck strength from bone mineral data. A structural approach. *Investigative Radiology*, 25(1):6–18, 1990.

[7] S. Benameur, M. Mignotte, H. Labelle, and J. De Guise. A hierarchical statistical modeling approach for the unsupervised 3-D biplanar reconstruction of the scoliotic spine. *IEEE Transactions on Biomedical Engineering*, 52(12):2041 – 2057, December 2005.

[8] D. M. Black, N. K. Arden, L. Palermo, J. Pearson, and S. R. Cummings. Prevalent Vertebral Deformities Predict Hip Fractures and New Vertebral Deformities but Not Wrist Fractures. *Journal of Bone and Mineral Research*, 14(5):821–828, 1999.

[9] D. M. Black, M. L. Bouxsein, L. M. Marshall, S. R. Cummings, T. F. Lang, J. A. Cauley, K. E. Ensrud, C. M. Nielson, and E. S. Orwoll. Proximal Femoral Structure and the Prediction of Hip Fracture in Men: A Large Prospective Study Using QCT. *Journal of Bone and Mineral Research*, 23(8):1326–1333, 2008.

[10] J. Boisvert, F. Cheriet, X. Pennec, H. Labelle, and N. Ayache. Articulated Spine Models for 3-D Reconstruction From Partial Radiographic Data. *Biomedical Engineering, IEEE Transactions on*, 55(11):2565–2574, November 2008.

[11] V. Bousson, A. Le Le Bras, F. Roqueplan, Y. Kang, D. Mitton, S. Kolta, C. Bergot, W. Skalli, E. Vicaut, W. Kalender, K. Engelke, and J.-D. Laredo. Volumetric quantitative computed tomography of the proximal femur: relationships linking geometric and densitometric variables to bone strength. Role for compact bone. *Osteoporosis International*, 17:855–864, 2006.

[12] V. D. Bousson, J. Adams, K. Engelke, M. Aout, M. Cohen-Solal, C. Bergot, D. Haguenauer, D. Goldberg, K. Champion, R. Aksouh, E. Vicaut, and J.-D.

Laredo. In vivo discrimination of hip fracture with quantitative computed tomography: Results from the prospective European Femur Fracture Study (EFFECT). *Journal of Bone and Mineral Research*, 26(4):881–893, 2011.

[13] P. M. Braillon. Volumetric bone mineral density derived from dual-energy X-ray absorptiometry measurements. *Nuclear Medicine Communications*, 20(1):106, 1999.

[14] A. T. Brooks, R. Improvements to the itk::KernelTransform and Subclasses. *Insight Journal*, January 2007.

[15] A. Burghardt, G. Kazakia, T. Link, and S. Majumdar. Automated simulation of areal bone mineral density assessment in the distal radius from high-resolution peripheral quantitative computed tomography. *Osteoporosis International*, 20(12):2017–2024, December 2009.

[16] K. F. E. B. Cann CE, Genant HK. Quantitative computed tomography for prediction of vertebral fracture risk. *Bone*, 6(1):1–7, 1985.

[17] D. R. Carter, M. L. Bouxsein, and R. Marcus. New approaches for interpreting projected bone densitometry data. *Journal of Bone and Mineral Research*, 7(2):137–145, 1992.

[18] R. B. Cattell. The Scree Test For The Number Of Factors. *Multivariate Behavioral Research*, 1(2):245–276, 1966.

[19] J. R. Center, T. V. Nguyen, D. Schneider, P. N. Sambrook, and J. A. Eisman. Mortality after all major types of osteoporotic fracture in men and women: an observational study. *The Lancet*, 353(9156):878–882, 1999.

[20] X. Cheng, J. Li, Y. Lu, J. Keyak, and T. Lang. Proximal femoral density and geometry measurements by quantitative computed tomography: Association with hip fracture. *Bone*, 40(1):169–174, 2007.

[21] X. Cheng, G. Lowet, S. Boonen, P. Nicholson, P. Brys, J. Nijs, and J. Dequeker. Assessment of the strength of proximal femur in vitro: Relationship to femoral bone mineral density and femoral geometry. *Bone*, 20(3):213–218, March 1997.

[22] G. Chintalapani, L. Ellingsen, O. Sadowsky, J. Prince, and R. Taylor. Statistical Atlases of Bone Anatomy: Construction, Iterative Improvement and Validation. In *Medical Image Computing and Computer-Assisted Intervention*, pages 499–506, 2007.

[23] E. A. Chrischilles, C. D. Butler, C. S. Davis, and R. B. Wallace. A Model of Lifetime Osteoporosis Impact. *Archives of Internal Medicine*, 151(10):2026–2032, 1991.

[24] C. Cooper, E. J. Atkinson, S. J. Jacobsen, W. M. OFallon, and L. J. Melton. Population-Based Study of Survival after Osteoporotic Fractures. *American Journal of Epidemiology*, 137(9):1001–1005, 1993.

[25] T. Cootes, G. Edwards, and C. Taylor. Active appearance models. *IEEE Transactions on Pattern Analysis and Machine Intelligence*, 23(6):681–685, June 2001.

[26] T. Cootes, A. Hill, C. Taylor, and J. Haslam. Use of active shape models for locating structures in medical images. *Image and Vision Computing*, 12(6):355–365, 1994.

[27] T. F. Cootes, G. J. Edwards, and C. J. Taylor. Active Appearance Models. In *European Conference on Computer Vision*, volume 2, pages 484–498, 1998.

[28] M. de Bruijne, M. T. Lund, L. B. Tankó, P. C. Pettersen, and M. Nielsen. Quantitative vertebral morphometry using neighbor-conditional shape models. *Medical Image Analysis*, 11(5):503–512, 2007.

[29] S. Delorme, Y. Petit, J. de Guise, H. Labelle, C.-E. Aubin, and J. Dansereau. Assessment of the 3-D reconstruction and high-resolution geometrical modeling of the human skeletal trunk from 2-D radiographic images. *IEEE Transactions on Biomedical Engineering*, 50(8):989–998, August 2003.

[30] Y. Duan, A. M. Parfitt, and E. Seeman. Vertebral Bone Mass, Size, and Volumetric Density in Women with Spinal Fractures. *Journal of Bone and Mineral Research*, 14(10):1796–1802, 1999.

[31] F. Duboeuf, D. Hans, A. M. Schott, P. O. Kotzki, F. Favier, C. Marcelli, P. J. Meunier, and P. D. Delmas. Different Morphometric and Densitometric Parameters Predict Cervical and Trochanteric Hip Fracture: The EPIDOS Study. *Journal of Bone and Mineral Research*, 12(11):1895–1902, 1997.

[32] K. Faulkner, H. Genant, and M. McClung. Bilateral comparison of femoral bone density and hip axis length from single and fan beam DXA scans. *Calcified Tissue International*, 56:26–31, 1995.

[33] M. Fleute, S. Lavallée, and L. Desbat. Integrated Approach for Matching Statistical Shape Models with Intra-operative 2D and 3D Data. In *Medical Image Computing and Computer-Assisted Intervention*, pages 364–372, 2002.

[34] I. O. Foundation. Osteoporosis in the Workplace: The social, economic and human costs of osteoporosis on employees, employers and governments, 2002.

[35] A. Frangi, D. Rueckert, J. Schnabel, and W. Niessen. Automatic construction of multiple-object three-dimensional statistical shape models: application to cardiac modeling. *IEEE Transactions on Medical Imaging*, 21(9):1151–1166, 2002.

[36] K. Fritscher, A. Grunerbl, M. Hanni, N. Suhm, C. Hengg, and R. Schubert. Trabecular Bone Analysis in CT and X-Ray Images of the Proximal Femur for the Assessment of Local Bone Quality. *IEEE Transactions on Medical Imaging*, 28(10):1560–1575, October 2009.

[37] K. Fritscher, A. Grünerbl, and R. Schubert. 3D image segmentation using combined shape-intensity prior models. *International Journal of Computer Assisted Radiology and Surgery*, 1(6):341–350, April 2007.

[38] K. Fritscher, B. Schuler, T. Link, F. Eckstein, N. Suhm, M. Hänni, C. Hengg, and R. Schubert. Prediction of Biomechanical Parameters of the Proximal Femur Using Statistical Appearance Models and Support Vector Regression. In *Medical Image Computing and Computer-Assisted Intervention*, pages 568–575, 2008.

[39] Y. Fujii, T. Tsunenari, M. Tsutsumi, A. Miyauchi, H. Yamada, M. Fukase, Y. Yoshimoto, Y. Okuno, H. Kusakabe, K. Miyoshi, M. Fukunaga, R. Morita, and T. Fujita. Quantitative computed tomography: Comparison of two calibration phantoms. *Journal of Bone and Mineral Metabolism*, 6:17–20, 1988.

[40] H. K. Genant, J. E. Block, P. Steiger, C.-C. Glueer, and R. Smith. Quantitative computed tomography in assessment of osteoporosis. *Seminars in Nuclear Medicine*, 17(4):316–333, 1987.

[41] H. K. Genant, S. Grampp, C. C. Glaer, K. G. Faulkner, M. Jergas, K. Engelke, S. Hagiwara, and C. van Kuijk. Universal standardization for dual X-ray absorptiometry: Patient and phantom cross-calibration results. *Journal of Bone and Mineral Research*, 9(10):1503–1514, 1994.

[42] V. Gilsanz, M. L. Loro, T. F. Roe, J. Sayre, R. Gilsanz, and E. E. Schulz. Vertebral size in elderly women with osteoporosis. Mechanical implications and relationship to fractures. *The Journal of Clinical Investigation*, 95(5):2332–2337, 5 1995.

[43] S. Gnudi, C. Ripamonti, G. Gualtieri, and N. Malavolta. Geometry of proximal femur in the prediction of hip fracture in osteoporotic women. *British Journal of Radiology*, 72(860):729–733, 1999.

[44] S. Gnudi, C. Ripamonti, L. Lisi, M. Fini, R. Giardino, and G. Giavaresi. Proximal Femur Geometry To Detect and Distinguish Femoral Neck Fractures from Trochanteric Fractures in Postmenopausal Women. *Osteoporosis International*, 13:69–73, 2002.

[45] E. W. Gregg, A. M. Kriska, L. M. Salamone, M. M. Roberts, S. J. Aderson, R. E. Ferrell, L. H. Kuller, and J. A. Cauley. The epidemiology of quantitative ultrasound: A review of the relationships with bone mass, osteoporosis and fracture risk. *Osteoporosis International*, 7:89–99, 1997.

[46] J. Gregory, D. Testi, A. Stewart, P. Undrill, D. Reid, and R. Aspden. A method for assessment of the shape of the proximal femur and its relationship to osteoporotic hip fracture. *Osteoporosis International*, 15:5–11, 2004.

[47] J. S. Gregory, A. Stewart, P. E. Undrill, D. M. Reid, and R. M. Aspden. Bone Shape, Structure, and Density as Determinants of Osteoporotic Hip Fracture: A Pilot Study Investigating the Combination of Risk Factors. *Investigative Radiology*, 40(9):591–597, 2005.

[48] G. Guglielmi, D. Diacinti, C. van Kuijk, F. Aparisi, C. Krestan, J. Adams, and T. Link. Vertebral morphometry: current methods and recent advances. *European Radiology*, 18:1484–1496, 2008.

[49] G. Guglielmi, S. K. Grimston, K. C. Fischer, and R. Pacifici. Osteoporosis: diagnosis with lateral and posteroanterior dual x-ray absorptiometry compared with quantitative CT. *Radiology*, 192(3):845–850, 1994.

[50] A. Guimond, J. Meunier, and J.-P. Thirion. Average brain models: a convergence study. *Computer Vision and Image Understanding*, 77(9):192–210, February 2000.

[51] J. Haczynski and A. Jakimiuk. Vertebral fractures: a hidden problem of osteoporosis. *Medical science monitor*, 7(5):1108–1117, 2001.

[52] W. C. Hayes, S. J. Piazza, and P. K. Zysset. Biomechanics of fracture risk prediction of the hip and spine by quantitative computed tomography. *Radiologic Clinics of North America*, 29(1):1–18, 1991.

[53] H. Hoppe. New quadric metric for simplifying meshes with appearance attributes. In *Proceedings of the 10th IEEE Visualization Conference*, pages 59–510, October 1999.

[54] B. K. P. Horn. Closed-form solution of absolute orientation using unit quaternions. *Journal of the Optical Society of America A*, 4(4):629–642, 1987.

[55] L. Humbert, J. D. Guise, B. Aubert, B. Godbout, and W. Skalli. 3D reconstruction of the spine from biplanar X-rays using parametric models based on transversal and longitudinal inferences. *Medical Engineering & Physics*, 31(6):681–687, 2009.

[56] L. Humbert, T. Whitmarsh, M. De Craene, L. M. del Río Barquero, K. Fritscher, R. Schubert, F. Eckstein, T. Link, and A. F. Frangi. 3D reconstruction of both shape and bone mineral density distribution of the femur from DXA images. In *Proceedings of the 2010 IEEE international conference on Biomedical imaging: from nano to Macro*, pages 456–459, 2010.

[57] A. Hurvitz and L. Joskowicz. Registration of a CT-like atlas to fluoroscopic X-ray images using intensity correspondences. *International Journal of Computer Assisted Radiology and Surgery*, 3(6):493–504, 2008.

[58] M. Ito, N. Wakao, T. Hida, Y. Matsui, Y. Abe, K. Aoyagi, M. Uetani, and A. Harada. Analysis of hip geometry by clinical CT for the assessment of hip fracture risk in elderly Japanese women. *Bone*, 46(2):453–457, 2010.

[59] M. Jergas, M. Breitenseher, C. Gler, D. Black, P. Lang, S. Grampp, K. Engelke, and H. Genant. Which vertebrae should be assessed using lateral dual-energy X-ray absorptiometry of the lumbar spine. *Osteoporosis International*, 5:196–204, 1995.

[60] M. Jergas, M. Breitenseher, C.-C. Gler, W. Yu, and H. K. Genant. Estimates of volumetric bone density from projectional measurements improve the discriminatory capability of dual X-ray absorptiometry. *Journal of Bone and Mineral Research*, 10(7):1101–1110, 1995.

[61] O. Johnell and J. Kanis. An estimate of the worldwide prevalence and disability associated with osteoporotic fractures. *Osteoporosis International*, 17:1726–1733, 2006.

[62] S. Kaptoge, T. J. Beck, J. Reeve, K. L. Stone, T. A. Hillier, J. A. Cauley, and S. R. Cummings. Prediction of Incident Hip Fracture Risk by Femur Geometry Variables Measured by Hip Structural Analysis in the Study of Osteoporotic Fractures. *Journal of Bone and Mineral Research*, 23(12):1892–1904, 2008.

[63] J. Keyak, M. Fourkas, J. Meagher, and H. Skinner. Validation of an automated method of three-dimensional finite element modelling of bone. *Journal of Biomedical Engineering*, 15(6):505–509, 1993.

[64] J. H. Keyak and S. A. Rossi. Prediction of femoral fracture load using finite element models: an examination of stress- and strain-based failure theories. *Journal of Biomechanics*, 33(2):209–214, 2000.

[65] B. Khoo, K. Brown, C. Cann, K. Zhu, S. Henzell, V. Low, S. Gustafsson, R. Price, and R. Prince. Comparison of QCT-derived and DXA-derived areal bone mineral density and T scores. *Osteoporosis International*, 20(9):1539–1545, September 2009.

[66] C. M. Klotzbuecher, P. D. Ross, P. B. Landsman, T. A. Abbott, and M. Berger. Patients with Prior Fractures Have an Increased Risk of Future Fractures: A Summary of the Literature and Statistical Synthesis. *Journal of Bone and Mineral Research*, 15(4):721–739, 2000.

[67] S. Kolta, A. Le Bras, D. Mitton, V. Bousson, J. A. De Guise, J. Fechtenbaum, J. D. Laredo, C. Roux, and W. Skalli. Three-dimensional X-ray absorptiometry (3D-XA): A method for reconstruction of human bones using a dual X-ray absorptiometry device. *Osteoporosis International*, 16(8):969–976, 2005.

[68] S. Kolta, S. Quiligotti, A. Ruyssen-Witrand, A. Amido, D. Mitton, A. Bras, W. Skalli, and C. Roux. In vivo 3D reconstruction of human vertebrae with the three-dimensional X-ray absorptiometry (3D-XA) method. *Osteoporosis International*, 19:185–192, 2008.

[69] R. Kurazume, K. Nakamura, T. Okada, Y. Sato, N. Sugano, T. Koyama, Y. Iwashita, and T. Hasegawa. 3D reconstruction of a femoral shape using a parametric model and two 2D fluoroscopic images. *Computer Vision and Image Understanding*, 113(2):202–211, 2009.

[70] T. F. Lang, J. H. Keyak, M. W. Heitz, P. Augat, Y. Lu, A. Mathur, and H. K. Genant. Volumetric quantitative computed tomography of the proximal femur: Precision and relation to bone strength. *Bone*, 21(1):101–108, 1997.

[71] C. M. Langton, S. Pisharody, and J. H. Keyak. Generation of a 3D proximal femur shape from a single projection 2D radiographic image. *Osteoporosis International*, 20(3):455–461, March 2009.

[72] A. Le Bras, S. Laporte, V. Bousson, D. Mitton, J. A. De Guise, J. D. Laredo, and W. Skalli. Personalised 3D reconstruction of proximal femur from low-dose digital biplanar radiographs. *International Congress Series*, 1256:214–219, June 2003.

[73] A. Le Bras, S. Laporte, D. Mitton, J. A. de Guise, and W. Skalli. Three-dimensional (3D) detailed reconstruction of human vertebrae from low-dose digital stereoradiography. *European Journal of Orthopaedic Surgery & Traumatology*, 13:57–62, 2003.

[74] W. Li, J. Kornak, T. Harris, J. Keyak, C. Li, Y. Lu, X. Cheng, and T. Lang. Identify fracture-critical regions inside the proximal femur using statistical parametric mapping. *Bone*, 44(4):596–602, 2009.

[75] W. Li, J. Kornak, T. Harris, Y. Lu, X. Cheng, and T. Lang. Hip fracture risk estimation based on principal component analysis of QCT atlas: a preliminary study. In *Medical Imaging 2009: Biomedical Applications in Molecular, Structural, and Functional Imaging*, volume 7262, page 72621M, 2009.

[76] W. Li, J. Kornak, T. B. Harris, J. Keyak, C. Li, Y. Lu, X. Cheng, and T. Lang. Bone fracture risk estimation based on image similarity. *Bone*, 45(3):560–567, 2009.

[77] R. Lindsay, S. L. Silverman, C. Cooper, D. A. Hanley, I. Barton, S. B. Broy, A. Licata, L. Benhamou, P. Geusens, K. Flowers, H. Stracke, and E. Seeman. Risk of New Vertebral Fracture in the Year Following a Fracture. *JAMA: The Journal of the American Medical Association*, 285(3):320–323, 2001.

[78] C. Lorenz and N. Krahnstöver. Generation of point-based 3D statistical shape models for anatomical objects. *Computer Vision and Image Understanding*, 77(9):175–191, 2000.

[79] P. Markelj, D. Tomaževič, B. Likar, and F. Pernuš. A review of 3D/2D registration methods for image-guided interventions. *Medical Image Analysis*, 16(3):642–661, 2012.

[80] D. Mattes, D. Haynor, H. Vesselle, T. Lewellen, and W. Eubank. PET-CT image registration in the chest using free-form deformations. *IEEE Transactions on Medical Imaging*, 22(1):120–128, January 2003.

[81] P. Mayhew, S. Kaptoge, N. Loveridge, J. Power, H. Kroger, M. Parker, and J. Reeve. Discrimination between cases of hip fracture and controls is improved by hip structural analysis compared to areal bone mineral density. an ex vivo study of the femoral neck. *Bone*, 34(2):352–361, 2004.

[82] L. J. Melton. Epidemiology of Spinal Osteoporosis. *Spine*, 22(24S):2S–11S, 1997.

[83] L. J. Melton, E. J. Atkinson, M. K. O'Connor, W. M. O'Fallon, and B. L. Riggs. Bone Density and Fracture Risk in Men. *Journal of Bone and Mineral Research*, 13(12):1915–1923, 1998.

[84] L. J. Melton, E. A. Chrischilles, C. Cooper, A. W. Lane, and B. L. Riggs. Perspective how many women have osteoporosis? *Journal of Bone and Mineral Research*, 7(9):1005–1010, 1992.

[85] C. Meyer, J. Boes, B. Kim, and P. Bland. Probabilistic Brain Atlas Construction: Thin-Plate Spline Warping via Maximization of Mutual Information. In *Medical Image Computing and Computer-Assisted Intervention*, volume 1679, pages 631–637, 1999.

[86] D. Mitton, C. Landry, S. Vron, W. Skalli, F. Lavaste, and J. De Guise. 3D reconstruction method from biplanar radiography using non-stereocorresponding points and elastic deformable meshes. *Medical and Biological Engineering and Computing*, 38:133–139, 2000.

[87] L. Mosekilde, S. Bentzen, G. rtoft, and J. Jrgensen. The predictive value of quantitative computed tomography for vertebral body compressive strength and ash density. *Bone*, 10(6):465–470, 1989.

[88] E. R. Myers and S. E. Wilson. Biomechanics of Osteoporosis and Vertebral Fracture. *Spine*, 22(24S):25S–31S, 1997.

[89] D. P. Nicolella and T. L. Bredbenner. Development of a parametric finite element model of the proximal femur using statistical shape and density modelling. *Computer Methods in Biomechanics and Biomedical Engineering*, 15(2):101–110, 2012.

[90] E. S. Orwoll, L. M. Marshall, C. M. Nielson, S. R. Cummings, J. Lapidus, J. A. Cauley, K. Ensrud, N. Lane, P. R. Hoffmann, D. L. Kopperdahl, and T. M. Keaveny. Finite Element Analysis of the Proximal Femur and Hip Fracture Risk in Older Men. *Journal of Bone and Mineral Research*, 24(3):475–483, 2009.

[91] J. Pettersson, M. Borga, and H. Knutsson. Some Issues on the Segmentation of the Femur in CT Data. In *Proceedings of the SSBA Symposium on Image Analysis*, pages 158–161, March 2004.

[92] J.-M. Peyrat, M. Sermesant, X. Pennec, H. Delingette, C. Xu, E. R. McVeigh, and N. Ayache. Statistical Comparison of Cardiac Fibre Architectures. In *Proceedings of Functional Imaging and Modeling of the Heart*, pages 413–423, 2007.

[93] G. Poór, S. J. Jacobsen, and L. J. Melton III. *Mortality following hip fracture: Facts and research in gerontology*. Serdi, 1994.

[94] W. Press, B. Flannery, S. Teukolsky, and W. Vetterling. *Numerical Recipes in C: The Art of Scientific Computing*. Cambridge University Press, October 1992.

[95] L. B. Querol, P. Büchler, D. Rueckert, L. P. Nolte, and M. A. Ballester. Statistical finite element model for bone shape and biomechanical properties. In *Medical Image Computing and Computer-Assisted Intervention*, pages 405–411, October 2006.

[96] M. Roberts, T. Oh, E. Pacheco, R. Mohankumar, T. Cootes, and J. Adams. Semi-automatic determination of detailed vertebral shape from lumbar radiographs using active appearance models. *Osteoporosis International*, 23:655–664, 2012.

[97] P. Ruegsegger and W. A. Kalender. A phantom for standardization and quality control in peripheral bone measurements by PQCT and DXA. *Physics in Medicine and Biology*, 38(12):1963–1970, 1993.

[98] O. Sadowsky, J. Lee, E. Sutter, S. Wall, J. Prince, and R. Taylor. Hybrid Cone-Beam Tomographic Reconstruction: Incorporation of Prior Anatomical Models to Compensate for Missing Data. *IEEE Transactions on Medical Imaging*, 30(1):69–83, 2011.

[99] M. F. Schreuder, A. P. van Driel, A. van Lingen, J. C. Roos, C. M. de Ridder, R. A. Manoliu, E. F. David, and J. C. Netelenbos. Volumetric measurements of bone mineral density of the lumbar spine: comparison of three geometrical approximations using dual-energy X-ray absorptiometry (DXA). *Nuclear Medicine Communications*, 19(8):727–733, 1998.

[100] B. Schuler, K. D. Fritscher, V. Kuhn, F. Eckstein, T. M. Link, and R. Schubert. Assessment of the individual fracture risk of the proximal femur by using statistical appearance models. *Medical Physics*, 37(6):2560–2571, 2010.

[101] B. Schuler, K. D. Fritscher, V. Kuhn, F. Eckstein, and R. Schubert. Using a statistical appearance model to predict the fracture load of the proximal femur. In *Proceedings of SPIE Medical Imaging 2009: Visualization, Image-Guided Procedures, and Modeling*, number 1, page 72610W, 2009.

[102] O. Sevinc, C. Barut, M. Is, N. Eryoruk, and A. A. Safak. Influence of age and sex on lumbar vertebral morphometry determined using sagittal magnetic resonance imaging. *Annals of Anatomy - Anatomischer Anzeiger*, 190(3):277–283, 2008.

[103] P. Steininger, K. D. Fritscher, G. Kofler, B. Schuler, M. Häni, K. Schwieger, and R. Schubert. Comparison of Different Metrics for Appearance-Model-Based 2D/3D-registration with X-ray Images. In *Bildverarbeitung für die Medizin 2008*, pages 122–126, 2008.

[104] M. Styner, C. Brechbühler, G. Székely, and G. Gerig. Parametric Estimate of Intensity Inhomogeneities Applied to MRI. *IEEE Transactions on Medical Imaging*, 19(3):153–165, 2000.

[105] S. Suzuki, T. Yamamuro, H. Okumura, and I. Yamamoto. Quantitative computed tomography: comparative study using different scanners with two calibration phantoms. *British Journal of Radiology*, 64(767):1001–1006, 1991.

[106] E. Urrutia Vega, R. E. Elizondo Omaña, O. De la Garza Castro, and S. Guzmán López. Morphometry of Pedicle and Vertebral Body in a Mexican Population by CT and Fluroscopy. *International Journal of Morphology*, 27:1299–1303, 12 2009.

[107] S. Väänänen, J. Jurvelin, and H. Isaksson. Estimation of 3D shape, internal density and mechanics of proximal femur by combining bone mineral density images with shape and density templates. *Biomechanics and Modeling in Mechanobiology*, 2011.

[108] T. Whitmarsh, K. D. Fritscher, L. Humbert, L. M. Del Rio Barquero, T. Roth, C. Kammerlander, M. Blauth, R. Schubert, and A. F. Frangi. A statistical model of shape and bone mineral density distribution of the proximal femur for fracture risk assessment. *Medical Image Computing and Computer-Assisted Intervention*, 14(Pt 2):393–400, January 2011.

[109] T. Whitmarsh, L. Humbert, M. D. Craene, L. M. del Río Barquero, K. Fritscher, R. Schubert, F. Eckstein, T. M. Link, and A. F. Frangi. 3D bone mineral density distribution and shape reconstruction of the proximal femur from a single simulated DXA image: an in vitro study. In *Proceedings of SPIE Medical Imaging 2010: Image Processing*, number 1, page 76234U, 2010.

[110] T. Whitmarsh, L. Humbert, M. De Craene, L. M. Del Rio Barquero, and A. F. Frangi. Reconstructing the 3D Shape and Bone Mineral Density Distribution of the Proximal Femur from Dual-energy X-ray Absorptiometry. *IEEE Transactions on Medical Imaging*, 30(12):2101–2114, December 2011.

[111] WHO. *Prevention and management of osteoporosis.* World Health Organization Technical Report Series 921, 2003.

[112] S. Yamakawa and K. Shimada. Removing Self Intersections of a Triangular Mesh by Edge Swapping, Edge Hammering, and Face Lifting. In *Medical Image Computing and Computer-Assisted Intervention*, pages 1205–1212, 1998.

[113] J. Yao and R. Taylor. Deformable registration between a statistical bone density atlas and X-ray images. In *Proceedings of the CAOS International*, pages 168–169, 2002.

[114] J. Yao and R. H. Taylor. Non-Rigid Registration And Correspondence Finding In Medical Image Analysis Using Multiple-Layer Flexible Mesh Template Matching. *International Journal of Pattern Recognition and Artificial Intelligence*, 17(7):1145–1165, 2003.

[115] T. Yoo, M. J. Ackerman, W. E. Lorensen, W. Schroeder, V. Chalana, S. Aylward, D. Metaxes, and W. R. Engineering and Algorithm Design for an Image Processing API: A Technical Report on ITK - The Insight Toolkit. In *Proceedings of Medicine Meets Virtual Reality*, pages 586–592, 2002.

[116] T. Yoshikawa, C. Turner, M. Peacock, C. Slemenda, C. Weaver, D. Teegarden, P. Markwardt, and D. Burr. Geometric structure of the femoral neck measured using dual-energy X-ray absorptiometry. *Journal of Bone and Mineral Research*, 9(7):1053–1064, 1994.

[117] P. A. Yushkevich, J. Piven, H. C. Hazlett, R. G. Smith, S. Ho, J. C. Gee, and G. Gerig. User-guided 3D active contour segmentation of anatomical structures: Significantly improved efficiency and reliability. *NeuroImage*, 31(3):1116–1128, 2006.

[118] G. Zheng. Statistical Deformable Model-Based Reconstruction of a Patient-Specific Surface Model from Single Standard X-ray Radiograph. In *Proceedings of the 13th International Conference on Computer Analysis of Images and Patterns*, pages 672–679, 2009.

[119] G. Zheng, S. Gollmer, S. Schumann, X. Dong, T. Feilkas, and M. A. G. Ballester. A 2D/3D correspondence building method for reconstruction of a patient-specific 3D bone surface model using point distribution models and calibrated X-ray images. *Medical Image Analysis*, 13(6):883–899, 2009.

[120] G. Zheng, L.-P. Nolte, and S. Ferguson. 2D/3D reconstruction of a scaled lumbar vertebral model from a single fluoroscopic image. In *Engineering in Medicine and Biology Society (EMBC), 2010 Annual International Conference of the IEEE*, pages 4395–4398, September 2010.

[121] S. H. Zhou, I. D. McCarthy, A. H. McGregor, R. R. H. Coombs, and S. P. F. Hughes. Geometrical dimensions of the lower lumbar vertebrae - analysis of data from digitised CT images. *European Spine Journal*, 9:242–248, 2000.

[122] C. Zhu, R. H. Byrd, P. Lu, and J. Nocedal. Algorithm 778: L-BFGS-B: Fortran subroutines for large-scale bound-constrained optimization. *ACM Transactions on Mathematical Software*, 23(4):550–560, 1997.

[123] R. Zoroofi, Y. Sato, T. Sasama, T. Nishii, N. Sugano, K. Yonenobu, H. Yoshikawa, T. Ochi, and S. Tamura. Automated segmentation of acetabulum and femoral head from 3-D CT images. *IEEE Transactions on Information Technology in Biomedicine*, 7(4):329–343, December 2003.

Publications

Journals

1. **T. Whitmarsh**, L. Humbert, L.M. Del Río Barquero, S. Di Gregorio, A.F. Frangi, 3D Reconstruction of the Lumbar Vertebrae from Anteroposterior and Lateral Dual-energy X-ray Absorptiometry, submitted, 2012.
2. **T. Whitmarsh**, K.D. Fritscher, L. Humbert, L.M. del Río Barquero, T. Roth, C. Kammerlander, M. Blauth, R. Schubert, A.F. Frangi, Hip Fracture Discrimination from Dual-energy X-ray Absorptiometry by Statistical Model Registration, submitted 2012.
3. C. Hoogendoorn, N. Duchateau, D. Sanchez-Quintana, **T. Whitmarsh**, F. Sukno, M. De Craene, K. Lekadir, A.F. Frangi, A High-Resolution Atlas and Statistical Model of the Human Heart from Multislice CT, submitted, 2012.
4. L. Humbert, **T. Whitmarsh**, M. De Craene, L.M. Del Río Barquero, A.F. Frangi, Technical Note: Comparison between Single and Multi-view DXA Configurations for Reconstructing the 3D Shape and Bone Mineral Density Distribution of the Proximal Femur, Medical physics, submitted, 2012.
5. **T. Whitmarsh**, L. Humbert, M. De Craene, L.M. Del Río Barquero, A.F. Frangi, Reconstructing the 3D Shape and Bone Mineral Density Distribution of the Proximal Femur from Dual-energy X-ray Absorptiometry, *IEEE Transactions on Medical Imaging*, vol. 30(12), pp. 2101-14, 2011.

Conferences

1. I.C. Mateos, L. Humbert, **T. Whitmarsh**, A. Lazary, L.M. Del Río Barquero, A.F. Frangi, 3D Reconstruction of Intervertebral Discs from T1-weighted Magnetic Resonance Images, *IEEE International Symposium on Biomedical Imaging 2011.*
2. L. Humbert, **T. Whitmarsh**, L.M. del Río Barquero, K. Fritscher, R. Schubert, F. Eckstein, T.M. Link, R. Schubert and A.F. Frangi, Femoral Strength Prediction using a 3D Reconstruction Method from Dual-energy X-ray Absorptiometry, *IEEE International Symposium on Biomedical Imaging 2011.*
3. **T. Whitmarsh**, K.D. Fritscher, L. Humbert, L.M. del Río Barquero, T. Roth, C. Kammerlander, M. Blauth, R. Schubert, A.F. Frangi, A Statistical Model of Shape and Bone Mineral Density Distribution of the Proximal Femur for Fracture Risk Assessment, *Medical Image Computing and Computer-Assisted Intervention*, vol. 6892, pp. 393-400, 2011.
4. **T. Whitmarsh**, K.D. Fritscher, L. Humbert, L.M. del Río Barquero, R. Schubert, A.F. Frangi, Hip Fracture Discrimination using 3D Reconstructions from Dual-energy X-ray Absorptiometry, *IEEE International Symposium on Biomedical Imaging 2011*, pp. 1189-1192, 2011.

5. L. Humbert, **T. Whitmarsh**, M. De Craene, L.M. del Río Barquero, K. Fritscher, R. Schubert, F. Eckstein, T.M. Link, and A.F. Frangi, 3D Reconstruction of Both the Shape and Bone Mineral Density Distribution of the Femur from DXA Images, *IEEE International Symposium on Biomedical Imaging 2010*, pp. 456-459, 2010.
6. C. Hoogendoorn, **T. Whitmarsh**, N. Duchateau, F. M. Sukno, D. de Craene, A. F. Frangi, B. M. Dawant, D. R. Haynor, A groupwise mutual information metric for cost efficient selection of a suitable reference in cardiac computational atlas construction, *In Proceedings of SPIE Medical Imaging 2010: Image Processing*, page 76231R, 2010.
7. **T. Whitmarsh**, L. Humbert, M. De Craene, L.M. Del Río Barquero, K. Fritscher, R. Schubert, F. Eckstein, T. Link and A.F. Frangi, 3D bone mineral density distribution and shape reconstruction of the proximal femur from a single simulated DXA image: an in vitro study, *In Proceedings of SPIE Medical Imaging 2010: Image Processing*, page 76234U, 2010.

Abstracts

1. M. Spinelli, F. Taddei, L. Humbert, **T. Whitmarsh**, L. Cristofolini, E. Schileo, M. Viceconti, A.F. Frangi, FE Prediction of Strains For Patient-Specific Proximal Femurs Generated from a Single DXA, *18th Congress of the European Society of Biomechanics*, Lisbon, Portugal, July 2012.
2. L. Humbert, **T. Whitmarsh**, L.M. del Río Barquero, A.F. Frangi, Computing Structural Parameters from Dual-energy X-ray Absorptiometry using a 3D Reconstruction Method, *European Congress on Osteoporosis & Osteoarthritis IOF-ECCEO12*, Bordeaux, France, 2012.
3. **T. Whitmarsh**, L. Humbert, L.M. del Río Barquero, A.F. Frangi, Volumetric Bone Mineral Density Estimation using a 3D Reconstruciton Method from dual-energy X-ray Absorptiometry, *Annual Meeting ASBMR*, San Diego, 2011.
4. M. Spinelli, L. Humbert, **T. Whitmarsh**, L. M. Del Río Barquero, M. Viceconti and A. F. Frangi, FE-ready Patient-specific Mesh Generation of the Proximal Femur Reconstructed from a Single DXA, *Computer Simulations in Bioengineering*, 2011.
5. **T. Whitmarsh**, L. Humbert, M. De Craene, L. Del Río Barquero, A. F. Frangi, Reconstrucción de la forma del fémur y distribución de densidad mineral ósea en 3D para el diagnóstico de osteoporosis, a partir de técnica DXA, *XIV Congreso SEIOMM*, Santander, Spain, October 2009.

Patents

1. **Whitmarsh T.**, Humbert L., del Río L., de Craene M., Frangi A.F. 2011. Method for obtaining a three-dimensional reconstruction from one or more projective views and use thereof. PCT patent PCT/IB2011000235, filed: 10/02/2011.

Curriculum Vitae

Tristan Whitmarsh obtained a Batchelor degree in Computer Science and a Master degree in Game and Media Technology from the Utrecht University in The Netherlands whereby his thesis work was done at IMATI-CNR in Genoa, Italy. He spent nine months as a Research Assistant at MIRALab at the University of Geneva in Switserland. Tristan joined the Center for Computational Imaging & Simulation Technologies in Biomedicine of the Universitat Pompeu Fabra in Barcelona, Spain in June 2008 and has since been working on statistical modelling and reconstructing bone structures for deriving an osteoporotic fracture risk estimation. He did a six month research visit at the Private Universität für Gesundheitswissenschaften, Medizinische Informatik und Technik (UMIT) Institut für Biomedizinische Bildanalyse, Hall in Tirol, Austria and a four month visit at the Department of Mechanical Engineering of the University of Sheffield, Sheffield, UK.